Spring 5-15-2019

Extraordinary Magnetoresistance in Encapsulated Graphene Devices

Bowen Zhou
Washington University in St. Louis

WASHINGTON UNIVERSITY IN ST. LOUIS

Department of Physics

Dissertation Examination Committee:
Erik Henriksen, Chair
Ken Kelton
Kater Murch
Chuan Wang
Li Yang

Extraordinary Magnetoresistance in Encapsulated Graphene Devices

by
Bowen Zhou

A dissertation presented to
The Graduate School
of Washington University in
partial fulfillment of the
requirements for the degree
of Doctor of Philosophy

May 2019
St. Louis, Missouri

Table of Contents

List of Figures

List of Tables

Acknowledgments

I owe a debt of gratitude to many people for all their support and help that has been given to me during my graduate school and dissertation writing. I know just the acknowledgements are far far less than enough to express ample gratitude to all those who have encouraged me throughout my academic career and life in US.

First and foremost, I must thank the support of my family. I also need to apologize to them since I have been in US for six years, and only got one chance to travel back to China to see them. It was four years ago, and I only stayed there for a little more than one month. I know how my family especially my parents missed me, and I frequently felt bad about leaving home for so long.

I would specially apologize to my grandparents. I heard both of them kept talking about me in their last days and I still could not go back because I was too busy and desperate in my experiments during the time. I missed the last chance to see them before they went to heaven, and I even missed their funerals. My only hope now is to wish them peace in Paradise.

I need to thank my advisor, Erik Henriksen for his guidance through my graduate study. His deep understanding of physics experiments, especially instrument physics, techniques, experiment and circuit design etc. helped me in all my measurements and study. Because he constantly pushed me to perform all kinds of theoretical calculations, I was able to understand deeper physics phenomena. Also because of his encouragement, I eventually figured a way to learn simulation by myself and use it to verify my experimental data.

I would like to thank the members of my faculty mentoring committee, Ken Kelton and Li Yang. Their feedback and insight to my research and career over the last several years has proved invaluable. Also, many thanks to Kater Murch and Chuan Wang for being members of my

dissertation committee. Kater also nicely invited people of physics department to his home and made many very delicious pizzas and other food to treat us.

I would like to thank the Physics Department and Graduate School to provide financial support for my graduate study.

I want to thank Jamie Elias, Jessie Balgley and Jordan Russell and all other lab mates for their help in my research. Thank Shiyuan Gao and Li Chen in Physics Department for theoretical discussion. Also thank Rahul Gupta for his continued support in cleanroom. Best wishes to his startup.

I also like to thank my collaborator, Johannes Pollanen and his students from Michigan State University. The project of gate-tunable acoustoelectric effect in graphene gave me a chance to learn surface acoustic wave and Heidelberg laser writer. I used the laser writer to prepare all the devices for the project and we were rewarded with one publication.

I would specially thank Esha Christie, now the Czar of International Friends. Esha and her husband Stan are very friendly, and they very actively helped me on job search, especially in connecting me with people in industries.

I would like to thank Kelsey Meinerz, Patrick Harrington, Matt Reisman, Mike Abercrombie for talking with me about problems of graduate school. Thank Hossein Mahzoon for his discussion on my future career. Also thank Sarah Akin, Julia Hamilton and Todd Hardt for their continued support in the department.

Last, but not least, I offer thanks to Jennifer Whitman, Mort Whitman, John Weir, Ed Moncada, Heather Murray and all my friends in International Friends, Tuesday Lunch and Washington University.

I could not have done this without the support from all those mentioned and so many more. Thank you all.

Bowen Zhou

Washington University in St. Louis

May 2019

Dedicated to my dreams.

ABSTRACT OF THE DISSERTATION

Extraordinary Magnetoresistance in Encapsulated Graphene Devices

by

Bowen Zhou

Doctor of Philosophy in Physics

Washington University in St. Louis, 2019

Professor Erik Henriksen, Chair

We report a study on the phenomenon of extraordinary magnetoresistance (EMR) in boron nitride encapsulated monolayer graphene devices. Extremely large EMR values–calculated as the change in magnetoresistance, $(\mathrm{R(B)} - R_0)/R_0$–can be found in these devices due to the vanishingly small resistance values at zero field. In many devices the zero-field resistance can become negative, which enables R_0 to be chosen arbitrarily close to zero depending only on measurement precision, resulting in very large EMR. We critically discuss the dependence of EMR on measurement precision and device asymmetry. On the other hand, we also find the largest reported values of the sensitivity to magnetic fields, given by the derivative dR/dB. Moreover, the sensitivity measured in a two-probe configuration is over an order of magnitude larger than in the standard four-probe configuration. Additionally, the gate-voltage-dependent resistance at zero field shows a strong electron-hole asymmetry, which we trace to the nature of the metal-graphene edge contact: as in the well-studied case of metals deposited on graphene, the graphene at one-dimensional edge contacts also appears

to be heavily electron-doped leading to the appearance of a resistive pn junction in the neighborhood of the central metallic shunt, when the bulk of graphene is gated to be p-type. We also report the effects of the sizes of the devices and the ratios of metallic disk to graphene on the EMR.

Chapter 1:

Introduction of Graphene

1.1 Brief History of Graphene

As early as 1947, P. R. Wallace published a paper on “The Band Theory of Graphite” providing the first theoretical explanation of electronic band structure of graphite. Although interest in this material was light at first, in recent decades a remarkable amount of effort has been devoted to its exploration.

A single atom layer of graphite, called graphene, was first exfoliated from a parent graphite crystal by Andre Geim and Konstantin Novoselov at the University of Manchester in 2004 [2]. The tool they used for exfoliation is extremely simple: using scotch tape to split graphite into graphene. They began a very productive series of experiments on graphene, and discovered many interesting phenomena including the first observation of the unusual “half-integer” quantum Hall effect in graphene.

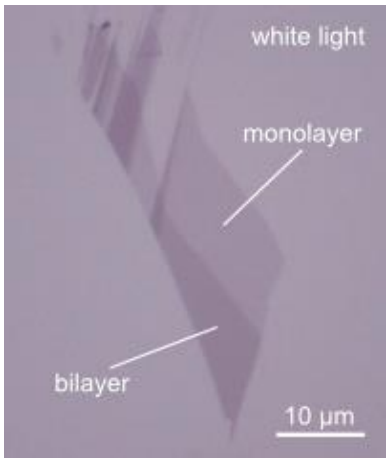

Figure 1.1 Example of scotch-tape exfoliated graphene [2].

This pioneering research on graphene was recognized with the Nobel Prize in Physics in 2010 "for groundbreaking experiments regarding the two-dimensional material graphene", which ultimately opened the door to research on a great variety of two-dimensional materials, such as borophene, germanene, phosphorene, and boron nitride, etc.

Besides scientific research, graphene has been widely studied in industry for novel applications and commercialization. As an alternative energy storage to traditional batteries based on electrochemistry, graphene supercapacitors have such advantages as large energy storage capacity, fast charging rates, long life span and environmentally friendly production. By 2017, for instance, Skeleton Technologies made commercial graphene supercapacitor units with maximal power output of 1500 kW available for industrial power applications [4].

1.2 Lattice structure of Graphene

Graphene is a single-atom-thick two-dimensional (2D) layer of carbon atoms with a honeycomb lattice structure. The structure can be treated as a triangular lattice with a basis of two atoms (A and B) in each unit cell and two lattice vectors: $\boldsymbol{a}_1 = (a/2)(3, \sqrt{3})$, and $\boldsymbol{a}_2 = (a/2)(3, -\sqrt{3})$ [3].

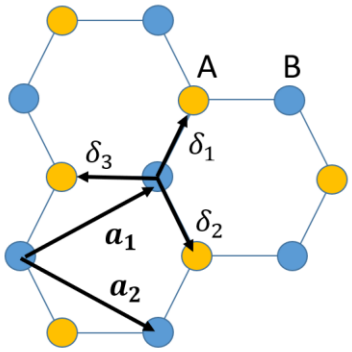

Figure 1.2 Schematic of honeycomb lattice structure of graphene.

Every carbon atom has 6 electrons: 2 in the inner 1s shell and 4 in the outer 2s and 2p shells. The electron configuration is: $(1s)^2(2s)^2(2p)^2$. The 4 outer shell electrons in each carbon atom are available for chemical bonding. In graphene, each carbon is connected with its three nearest neighbors, each at a distance of $a = 1.42$ Å away, through three σ bonds (pairs of electrons), which are the result of the sp^2 orbital hybridization – the combination of orbitals s, p_x and p_y orbitals. The three σ bonds have an angle of 120 degrees with each other and generate a very strong in-plane binding. The fourth bond is formed from the leftover p_z orbital, which is perpendicular to the graphene surface, and hybridizes with neighboring atoms to create π and π^* (bonding and anti-bonding) bands. In multilayer graphene or graphite, between each layer the weakly-interacting π bonds give rise to Van-der-Waals-forces, which enables the layers to be readily pried apart, and

enables the construction of multi-layer "van der Waals heterostructures" comprised of graphene and other thin layer materials.

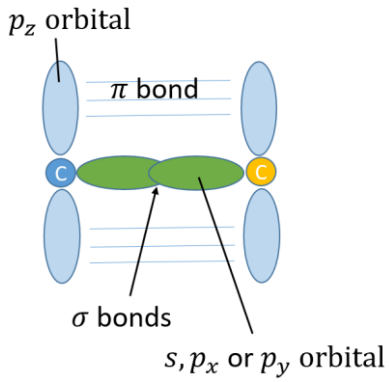

Figure 1.3 Schematic of σ bond and π bond in graphene.

1.3 Band structure of Graphene

Good metallic conductors have partially filled conduction or valence bands, in contrast to semimetals which typically have overlapped valence and conduction bands. Meanwhile, insulators and undoped semiconductors have a band gap, therefore, at low temperatures charge carriers cannot get into the conduction band and these materials conduct poorly. Extrinsically-doped semiconductors populate the conduction or valence band with impurity- or field-effect-sources carriers.

Graphene is conventionally treated as a semimetal with zero bandgap: the valence and the conduction bands meet at charge neutrality, when the valence band is completely full and the conduction band completely empty. Electrons or holes can be made to populate the conduction or

valence band depending on the Fermi level, which may be controlled by the electric-field-effect, using a nearby gate voltage for electrostatic charge doping.

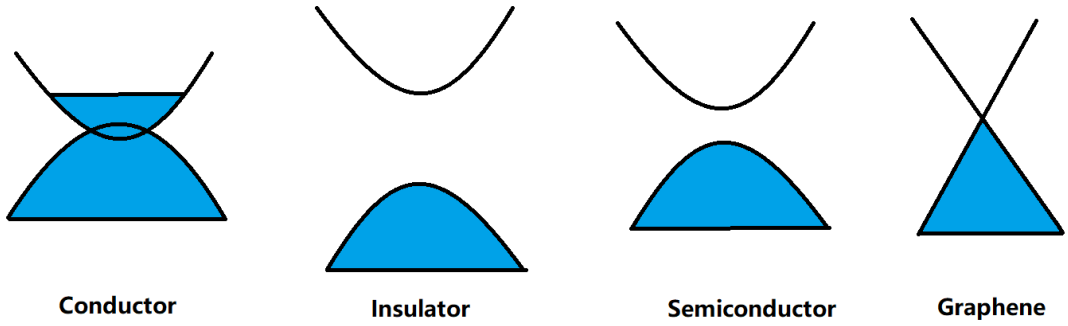

Figure 1.4 Schematic band structures of conductor, insulator, semiconductor and graphene.

Returning to the tight-binding description of graphene by Wallace in 1947, we find the bonding and antibonding π- and π^*- orbitals form the valence band and the conduction band, which touch at the neutral point, called Dirac point of graphene. In momentum space, there are two sets of three equivalent so-called "Dirac points" at the K and K' valleys. Each set is inequivalent with the other. The widely-referenced linear band dispersion of graphene is located within around 1eV of the Dirac point energy:

$$E_{\pm}(q) = \pm\hbar v_F q \tag{1.1}$$

where q is the 2D wavevector relative to the Dirac point in the momentum space and $v_F = 10^6 m/s$ is the Fermi velocity, which is 1/300th of the speed of light. This suggests the motion of real electrons in graphene is comfortably non-relativistic, despite the linear quasi-relativistic dispersion for quasiparticles.

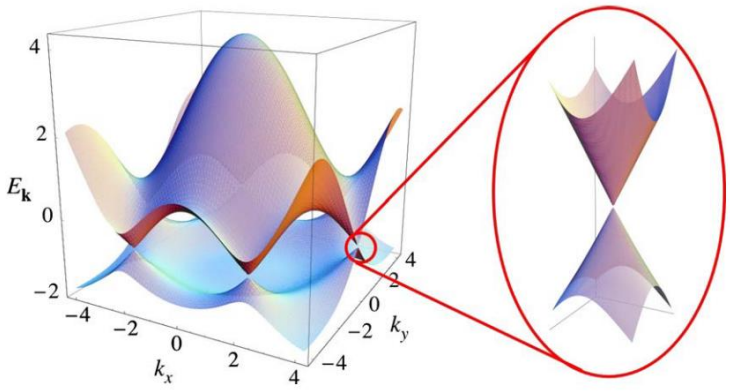

Figure 1.5 Electronic dispersion in the honeycomb lattice of graphene [3]. Two inequivalent corners of the Brillouin zone at the K and K' valleys are known as the Dirac points.

The low energy effective 2D continuum Schrodinger equation for spinless graphene carriers near the Dirac point and the corresponding effective low energy Dirac Hamiltonian are:

$$-\hbar v_F \sigma \cdot \nabla \Psi(\mathrm{r}) = E\Psi(\mathrm{r}) \tag{1.2}$$

$$\mathcal{H} = \hbar v_F \begin{pmatrix} 0 & q_x - iq_y \\ q_x + iq_y & 0 \end{pmatrix} = \hbar v_F \sigma \cdot q \tag{1.3}$$

where $\sigma = (\sigma_x,\ \sigma_y)$ is the vector of 2D Pauli matrices, and $\Psi(\mathrm{r})$ is a 2D spinor wave function.

The momentum space pseudospinor eigenfunctions of this Hamiltonian are:

$$\Psi(q, K) = \frac{1}{\sqrt{2}} \begin{pmatrix} e^{-i\theta_q/2} \\ \pm e^{i\theta_q/2} \end{pmatrix} \tag{1.4}$$

$$\Psi(q, K') = \frac{1}{\sqrt{2}} \begin{pmatrix} e^{i\theta_q/2} \\ \pm e^{-i\theta_q/2} \end{pmatrix} \tag{1.5}$$

where $\pm$ signs represent the conduction (valence) bands with dispersion $E_{\pm}(q) = \pm\hbar v_F q$.

Each graphene sublattice can be treated as being responsible for one branch of the dispersion. These two dispersion branches interact very weakly with one another. This chiral effect indicates the existence of a pseudospin quantum number for the charge carriers in graphene, which is analogous to the "real" spin. We can use the pseudospin to differentiate between contributions from each of the sublattices. This independence is called chirality because of the inability to transform one type of dispersion into another.

1.4 Basic Physical Properties of Graphene

With zero band gap, the charge carrier density can be smoothly tuned between the conduction band and the valence band of graphene. The ease with which the Fermi level can be tuned makes graphene an extraordinary material to study 2D physics phenomena that depend on the carrier density.

1.4.1 Charge Density and Fermi Level

The charge density (n) of electrons or holes can be tuned by applying the gate voltage (V_g) between the silicon substrate and graphene. Applying the gate voltage creates the electric field between the gate and graphene, which induces a charge density: $n = \epsilon_0 \epsilon V_g / de$ where $\epsilon_0 \epsilon$ and d are the dielectric constant and thickness of SiO_2 layer respectively, and e is the electron charge. Positive gate voltage attracts electrons while negative gate voltage induces holes in graphene. Fermi level

(E_f) is used to characterize the highest filled energy levels to in the band structure of graphene, which can be controllably shifted through the band structure as the charge density changes.

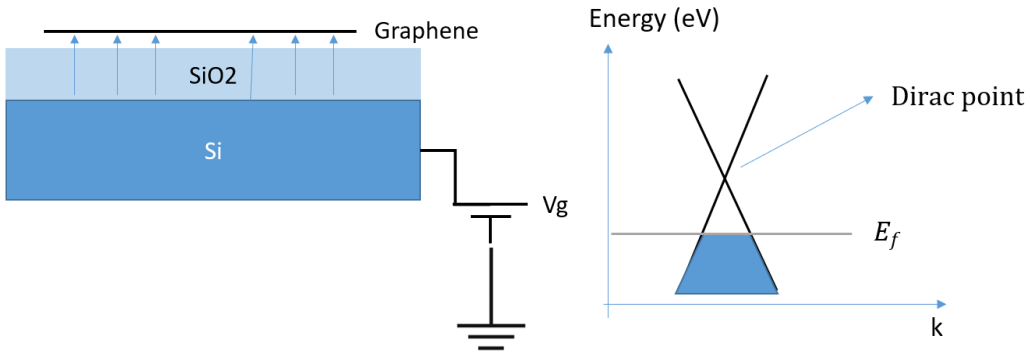

Figure 1.6 Schematic of a graphene flake sitting on an oxidized silicon substrate (left) and the Fermi level in the band structure (right).

When the Fermi level is at the Dirac point of the band structure, the charge density is zero since the valence band is filled so that no charges can move while the conduction band is left completely empty. As the Fermi level increases from the Dirac point, the charge density of electrons increases, so that the resistance of graphene is lowered; as the Fermi level decreases from the Dirac point, the charge density of holes increases, and the resistance is also decreased, resulting in a convenient bipolar conductivity.

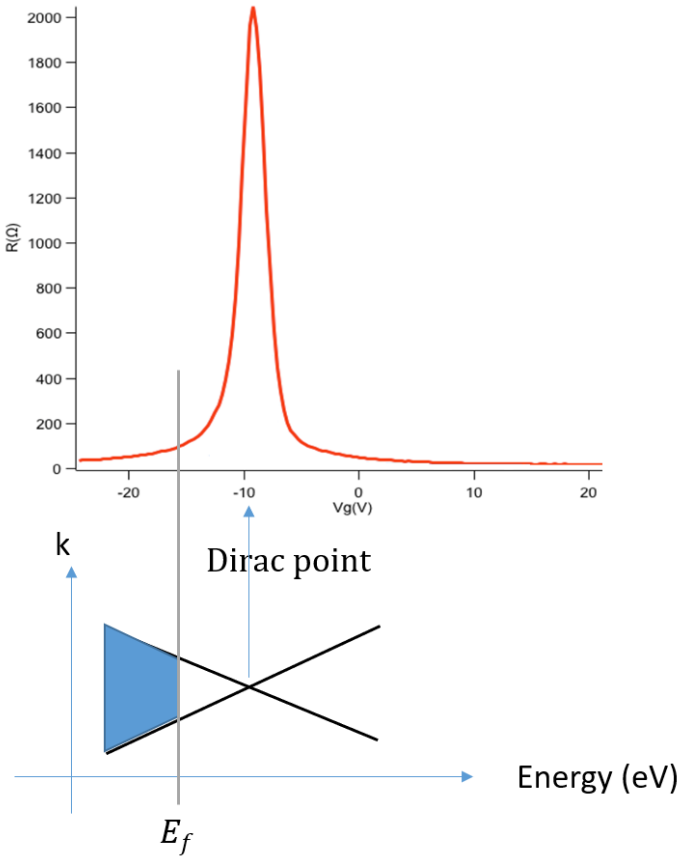

Figure 1.7 (Top) A plot of the resistance of a bilayer graphene device versus gate voltage; (bottom) the corresponding schematic illustration of Fermi energy level in the band structure of graphene. The Dirac point corresponds to the largest resistance of graphene. The Fermi level represented by the grey line is set in the valence band corresponding to the negative gate voltage range suggesting the graphene has charge carriers of holes. Likewise, it is in the positive gate voltage range if the Fermi level is in the conduction band.

1.4.2 Resistance

The most typical method for characterizing electric transport in graphene is the four-wire measurement of the Hall resistance. At this point, we only consider the longitudinal measurement: Current is passed through the graphene device, while the voltage drop between the two probes in the longitudinal direction is measured. By using the four-wire measurement, the contact resistance

(the resistance of the interface between electrical contact and graphene) and the resistance of any hookup wire can be avoided as almost no current flows to the measuring instrument due to its huge input impedance, so that the voltage drop in the measuring wires and graphene contacts is negligible. Therefore, the device resistance in four-wire measurement is more accurate than that in the two-wire measurement.

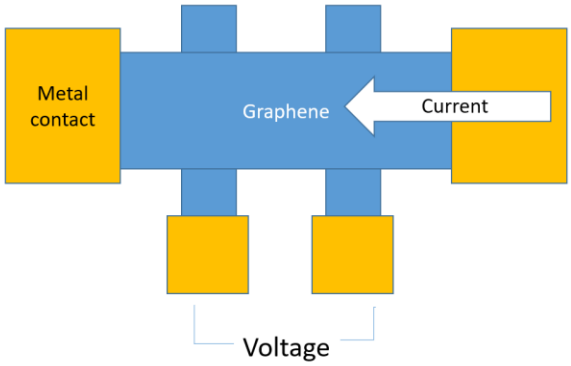

Figure 1.8 Schematic of four-wire measurement on graphene.

Ohm's law then gives the longitudinal resistance $R_{xx} = V_{xx}/I$, where I is the applied current through the device and V_{xx} is the measured longitudinal voltage. More details of the Hall resistivity and conductivity will be discussed in Section 2.1.2 of Chapter 2.

1.4.3 Carrier Mobility

In the equilibrium state of a conducting system, the charges diffuse around randomly without producing any net current in any direction. When an electric field is applied to the system, the charges acquire a net drift velocity v_d in response to the E-field. In any non-perfect conducting system, the moving charges can undergo scattering from impurities and lattice vibrations

(phonons), changing the momentum and energy of the charges. At steady state, since there is no net acceleration, the scattering effect on the momentum must be in balance with the effect of electric field. Then the rate of the charges gaining momentum (p) due to the electric field should be equal to the rate of losing momentum due to scattering:

$$[\frac{dp}{dt}]_{scattering} = [\frac{dp}{dt}]_{field}$$

$$\frac{mv_d}{\tau} = qE$$

where τ is the scattering time, which characterizes the time during which carriers are ballistically accelerated by the electric field before changing their direction and/or energy due to scattering.

In an electric field, the relative ease with which charges can move through a material is described by the carrier mobility, which is defined as the ratio of drift velocity to the electric field:

$$\mu = \frac{v_d}{E} = \frac{q}{m}\tau \tag{1.6}$$

The conductivity of the carriers also depends on the scattering time:

$$\sigma = nq^2\frac{\tau}{m} \tag{1.7}$$

And therefore, the conductivity can be expressed by the mobility:

$$\sigma = nq\mu \tag{1.8}$$

The carrier mobility is a useful parameterization of how clean the system is, as a higher mobility implies a reduction in impurity scattering events. Typical values of the carrier mobility in graphene are 10^3-10^4 cm^2/Vs for graphene-on-oxide devices, or 10^4-10^6 cm^2/Vs for higher quality graphene

encapsulated in flakes of hexagonal boron nitride. Graphene itself has a high intrinsic mobility on a par with pure bulk Si, even at room temperature.

1.4.4 Mean Free Path, Diffusive and Ballistic Transport

The mean free path is associated with the scattering time. It describes the average distance travelled by a moving particle between successive scattering events. The conductivity can be expressed using the mean free path:

$$\sigma = 2\frac{q^2}{\mathrm{h}}\mathrm{k}l_m$$

where $\mathrm{k} = \sqrt{\pi \mathrm{n}}$. Comparing this equation with (1.8), we find

$$l_m = \frac{\hbar}{\mathrm{q}}\mu\sqrt{n\pi} \tag{1.9}$$

When the mean free path of the charges is smaller than the size of the system, multiple scattering events occur before hitting the walls of the system, so that diffusive transport is observed.

In contrast, when the mean free path of the charges is larger than the size of the system, the charges are scattered primarily at the system edges, which is referred to as ballistic transport.

Since the mean free path depends on the carrier mobility, the cleaner the system is, the longer the mean free path can be. Therefore, the charge carriers could get from the diffusive transport into the ballistic transport if the same system gets cleaner as shown in equation (1.9).

Diffusive and ballistic transport will be discussed in detail in Chapter 4.

Bibliography

1. K. S. Novoselov, A. K. Geim, S. V. Morozov et al., *Electric field in atomically thin carbon films*, Science, **306**, 666 (2004).

2. Reproduced from website: http://grapheneindustries.com/?Products.

3. A. H. Castro Neto, F. Guinea, N. M. R. Peres, K. S. Novoselov, and A. K. Geim, *The electronic properties of graphene*, Rev. Mod. Phys. **81**, 109 (2009).

4. https://www.graphene-info.com/skeleton-uses-curved-graphene-its-new-supercapacitor-based-energy-storage-system

Chapter 2:

Fundamentals of Extraordinary Magnetoresistance

2.1 Theory of Extraordinary Magnetoresistance

Magnetoresistance (MR) is a physical property of a material, showing the tendency to change the value of electrical resistance with an externally-applied magnetic field. It was first discovered by William Thomson (Lord Kelvin) in 1856.

The extraordinary magnetoresistance (EMR) is a specific geometrical magnetoresistance effect. In the literature there are two major structures of EMR devices: circular and rectangular. For this dissertation, we focus on the circular structure. Since the circular EMR device typically has a thickness that is significantly smaller than its diameter, we treat the system as a two-dimensional system. The EMR device is typically constructed with a circular semiconductor having an embedded circular metal shunt in the center.

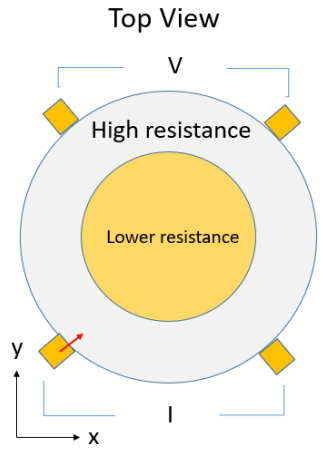

Figure 2.1 Schematic of EMR device.

Four contacts are evenly spaced around the device: two are used as current source and drain (I), and the other two are used for voltage measurement (V). The nonlocal resistance is defined as $R = V/I$, and the magnetoresistance is normalized so that $MR = [R(B) - R_0]/R_0$, where $R(B)$ is the resistance in a magnetic field perpendicular to the device, and R_0 is the minimal resistance at zero magnetic field.

2.1.1 Lorentz Force

The conductivity of the metallic shunt, σ_m, is much larger than that of the semiconductor, σ_s. At zero magnetic field, the current prefers to run through the low-resistance central metal shunt in our device and therefore bypasses much of the graphene (or other semiconductor material); as the magnetic field is increased, the Lorentz force

$$F = q(E + v \times B) \tag{2.1}$$

-where E is the applied electric field, v the drift velocity of the charge carriers, and B the magnetic field - gradually redirects current into the high-resistance graphene area, bypassing the metal shunt.

Hence, we see the MR increases with the magnetic field, and that the conductivity ratio of the metal to the semiconductor σ_m/σ_s plays a key role in the magnitude of MR. This will be discussed more in Section 2.4.

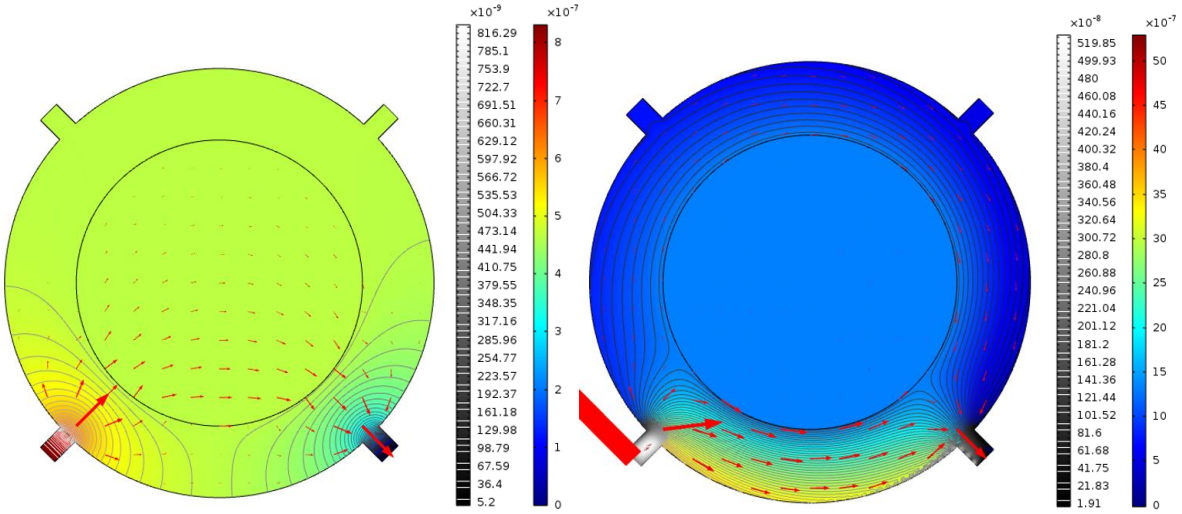

Figure 2.2 Simulation of electrical current in EMR device with zero field (left) and with high magnetic field (right) by COMSOL Multiphysics. Colors represent the electric potential, red means high and blue means low. Red arrows represent the current density, the larger the arrows the higher density. Black contours represent the equipotential lines.

Looking further into the physics details: at zero magnetic field, the direction of the current is parallel to that of the applied electric field which is normal to the equipotential surface of the metal (the metal itself is effectively an equipotential due to its high conductivity), therefore, the current runs into and passes through the metal shunt since its direction is normal to the interface. However, in a magnetic field, the current is deflected around the shunt by the Lorentz force and its direction is no longer parallel with that of the electric field. At sufficiently high magnetic field, the direction

of current becomes parallel with the metal-semiconductor interface, therefore, the current bypasses the metal shunt in the center. Thus, the current is forced to travel through the more resistive material around the shunt, leading to a magnetoresistance enhanced over the zero field resistance by orders of magnitude.

2.1.2 Mathematical illustrations

In 1927, the Drude–Sommerfeld model for free electrons was developed principally by Arnold Sommerfeld. This model describes the behavior of charge carriers in a metallic solid.

There are four assumptions:

(1) Free electron approximation: The electrons do not interact with the ions which are treated as charge neutral in the metal, except in boundary conditions.

(2) Independent electron approximation: The interactions between electrons are ignored.

(3) Relaxation-time approximation: The electron probability of collision is inversely proportional to the average time between collisions--the relaxation time τ.

(4) Pauli exclusion principle: An electron can only occupy one quantum state of the system.

This Drude–Sommerfeld model can be applied in semiconductor and graphene as well, and it is the basis of the following derivations.

The applied magnetic field B is in the z direction so $B = (0, 0, B)$, and the current I is driven through the sample from the lower-left contact in the x direction. And the electric field E is in the x-y plane: $E = (E_x, E_y, 0)$.

In the relaxation time approximation, the drift velocity $\boldsymbol{v}$ of charge carrier can be expressed in equation:

$$m\left(\frac{dv}{dt}+\frac{v}{\tau}\right)=qE+qv\times B \tag{2.2}$$

where q is the charge of the carrier; m is its effective mass; and $1/\tau$ is its relaxation (scattering) rate; the right hand side of the equation is the expression of the Lorentz force.

We only consider the steady state of system, so there is no velocity change with time.

So $\frac{dv}{dt}=\frac{dv_x}{dt}=\frac{dv_y}{dt}=0$. And then the rest of the velocity components can be expressed by electric field and the magnetic field as

$$v_x=q\frac{\tau}{m}(E_x+v_yB) \tag{2.3}$$

$$v_y=q\frac{\tau}{m}\left(E_y-v_xB\right) \tag{2.4}$$

With these two equations, we can only use E_x and E_y to express v_x and v_y:

$$(1+\frac{q^2B^2\tau^2}{m^2})v_x=q\frac{\tau}{m}E_x+\frac{q^2B^2\tau^2}{m^2}E_y \tag{2.5}$$

$$(1+\frac{q^2B^2\tau^2}{m^2})v_y=-\frac{q^2B^2\tau^2}{m^2}E_x+q\frac{\tau}{m}E_y \tag{2.6}$$

Combine these two equations, and get their matrix form:

$$(1+\frac{q^2B^2\tau^2}{m^2})\begin{pmatrix}v_x\\v_y\end{pmatrix}=\begin{pmatrix}q\frac{\tau}{m} & \frac{q^2B^2\tau^2}{m^2}\\ -\frac{q^2B^2\tau^2}{m^2} & q\frac{\tau}{m}\end{pmatrix}\begin{pmatrix}E_x\\E_y\end{pmatrix} \quad (2.7)$$

Since the current density is $J=(J_x,J_y,0)$, and $J=nqv=\sigma E$; then the matrix form of the current density is

$$\begin{pmatrix}J_x\\J_y\\0\end{pmatrix}=\begin{pmatrix}\sigma_{xx} & \sigma_{xy} & \sigma_{xz}\\ \sigma_{yx} & \sigma_{yy} & \sigma_{yz}\\ \sigma_{zx} & \sigma_{zy} & \sigma_{zz}\end{pmatrix}\begin{pmatrix}E_x\\E_y\\0\end{pmatrix}$$

Since we only consider charges moving in 2D system here, we can simplify it as:

$$\begin{pmatrix}J_x\\J_y\end{pmatrix}=\begin{pmatrix}\sigma_{xx} & \sigma_{xy}\\ \sigma_{yx} & \sigma_{yy}\end{pmatrix}\begin{pmatrix}E_x\\0\end{pmatrix}$$

The current matrix can be expressed by the velocity matrix:

$$\begin{pmatrix}J_x\\J_y\end{pmatrix}=nq\begin{pmatrix}\boldsymbol{v}_x\\\boldsymbol{v}_y\end{pmatrix}=\frac{\frac{nq^2\tau}{m}}{1+\frac{q^2B^2\tau^2}{m^2}}\begin{pmatrix}1 & q\frac{\tau B}{m}\\ -q\frac{\tau B}{m} & 1\end{pmatrix}\begin{pmatrix}E_x\\E_y\end{pmatrix}$$

$$\sigma=\frac{\frac{nq^2\tau}{m}}{1+\frac{q^2B^2\tau^2}{m^2}}\begin{pmatrix}1 & q\frac{\tau B}{m}\\ -q\frac{\tau B}{m} & 1\end{pmatrix}$$

Let $\sigma_0=nq^2\tau/m$ (conductivity at zero magnetic field).

In an electric field, mobility of a charge is proportional to the relaxation time:

$$\mu = \frac{q}{m}\tau \tag{2.8}$$

Then

$$\sigma_{xx} = \frac{\sigma_0}{1 + \mu^2 \mathrm{B}^2} \tag{2.9}$$

$$\sigma_{yx} = \frac{\sigma_0 \mu B}{1 + \mu^2 B^2} \tag{2.10}$$

$$\sigma_{yy} = \sigma_{xx} = \frac{\sigma_0}{1 + \mu^2 B^2} \tag{2.11}$$

$$\sigma_{xy} = -\sigma_{yx} = -\frac{\sigma_0 \mu B}{1 + \mu^2 B^2} \tag{2.12}$$

The conductivity components are expressed by the mobility and the magnetic field.

Thus, we can plug these components back to the conductivity tensor and get the final equation:

$$\begin{aligned} \sigma &= \begin{pmatrix} \sigma_{xx} & \sigma_{xy} \\ -\sigma_{xy} & \sigma_{xx} \end{pmatrix} \\ &= \frac{\sigma_0}{1 + \mu^2 B^2} \begin{pmatrix} 1 & -\mu B \\ \mu B & 1 \end{pmatrix} \\ &= \begin{pmatrix} \frac{\sigma_0}{1+\mu^2 B^2} & -\frac{\sigma_0 \mu B}{1+\mu^2 B^2} \\ \frac{\sigma_0 \mu B}{1+\mu^2 B^2} & \frac{\sigma_0}{1+\mu^2 B^2} \end{pmatrix} \end{aligned} \tag{2.13}$$

From this equation, we can see at B=0, σ is diagonal so J // E. At small B, the off-diagonal terms of σ appears and make J non-parallel with E. At sufficiently high B, J is perpendicular to E since the off-diagonal terms dominate.

The resistivity is the inverse of the conductivity: $\rho = 1/\sigma$. So the resistivity tensor is also relevant to the mobility of the device and the magnetic field as

$$\rho = \begin{pmatrix} \rho_{xx} & \rho_{xy} \\ \rho_{xy} & \rho_{xx} \end{pmatrix} = \frac{1}{\sigma_0} \begin{pmatrix} 1 & \mu B \\ -\mu B & 1 \end{pmatrix} \tag{2.14}$$

where $\rho_{xx} = 1/\sigma_0 = m/nq^2\tau$ and $\rho_{xy} = \mu B/\sigma_0 = B/nq$. Therefore, we get the conductivity tensor and resistivity tensor of the Hall effect.

2.2 First Discovery of Extraordinary Magnetoresistance

The EMR effect was discovered by Stuart Solin, et al. in 2000 [1]. Their EMR devices were circular and made of a gold circular shunt in the center of an outside circular semiconductor InSb (Indium antimonide) with 1.3-mm diameter, electron concentration n = 2.6 × $\mathbf{10^{22}}$ $\boldsymbol{m^{-3}}$, and mobility μ = 4.55 $\boldsymbol{m^2/Vs}$. Four evenly-spaced contacts are made by Ti/Pt/Au.

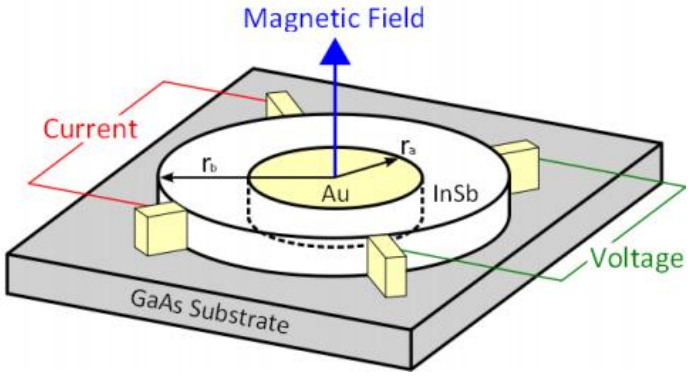

Figure 2.3 Schematic of EMR device made by Solin, et al. [1]

In this original discovery, the central metallic shunt has a much higher conductivity than the semiconductor. An extremely large magnetoresistance, with R(B) at 9 T found to increase by more

than four orders of magnitude, arises due to the device geometry. And a huge magnetoresistance of MR=15200 or a change of 1520000%, was also found in their EMR devices at room temperature.

They also demonstrated the metal shunt filling factor α, defined as $\alpha = \frac{r_a}{r_b}$, can make a huge difference in MR, where r_a and r_b are the inside and outside disk radii of the device. When the filling factor is larger, more current runs through the central gold shunt of low resistance at zero field; and correspondingly, more runs through the narrow area of the semiconductor of high resistance at high field, yielding a larger MR increases. The filling factor α =12/16 or 13/16 has been found to give the largest MR as shown by the solid circles in the plot below, and the filling factor α = 0 (no metal shunt) gives almost negligible MR represented by the open square. Increasing the filling factor beyond the optimal value, MR decreases since the semiconductor channel is too narrow for a large current density.

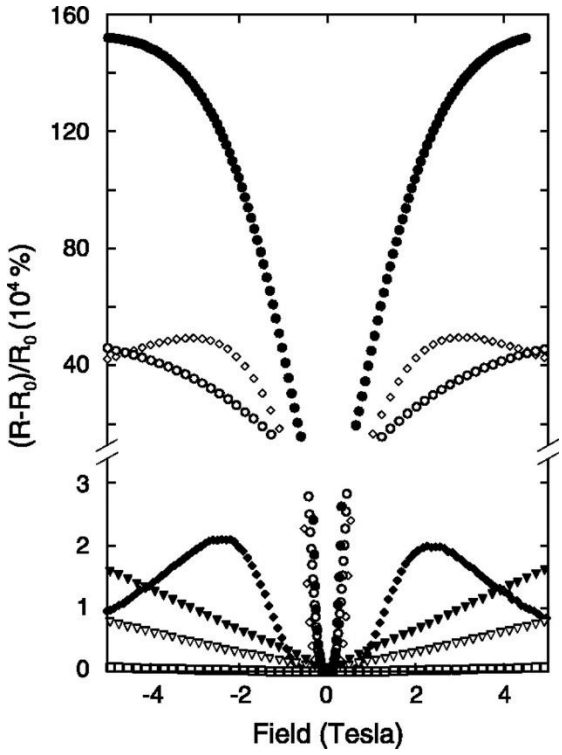

Figure 2.4 Plot of MR versus the field of EMR device made by Solin, et al [1]. The solid circle represents the largest MR corresponding to the filling factor α =12/16. And the open square represents the smallest MR corresponding to the filling factor α = 0.

From this plot, we can see that MR starts at 0 at zero field and increases with the magnetic field. The largest MR saturates at B=5T.

Since MR changes by four order of magnitude with increase of the B field to 5T, the EMR devices show a very high sensitivity to magnetic field. The magnetic sensitivity represents how sensitive the device is to the magnetic field, and it is defined as the derivative of resistance with respect to the magnetic field, expressed as dR/dB. The high EMR effect suggests the EMR device can be used to detect small magnetic field changes and therefore, EMR has received wide interests in application of magnetic sensor and future hard drive [3].

Since its discovery, similar EMR devices have been made by different materials but none to date rivals the largest record of magnetoresistance (MR) reported in Solin's initial devices.

Practical EMR devices in industry such as magnetic sensors have rectangular structures since they are easier to manufacture for use as microscopic field detectors, but there is a conformal equivalence to the circular structures [4]. The rectangular structure is basically two unrolled strips formed by semiconductor and metal.

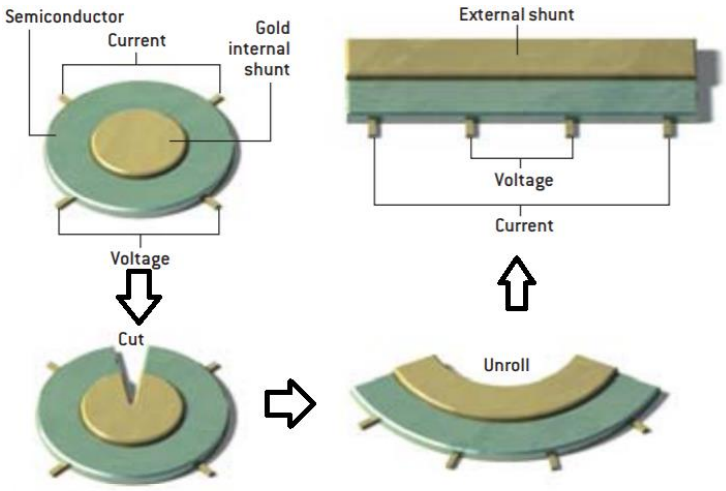

Figure 2.5 Conformal mapping of EMR device [4]. Cut a circular EMR device with four equal-spaced contacts and unroll the metal and semiconductor and get the rectangular structure of two strips formed by semiconductor and metal. The resulting four contacts are equal spaced.

We note that Jian Sun et al. have used COMSOL Multiphysics to perform simulation in rectangular devices and suggest that higher sensitivities could be obtained by using a two-contact EMR device rather than a four-terminal measurement [7].

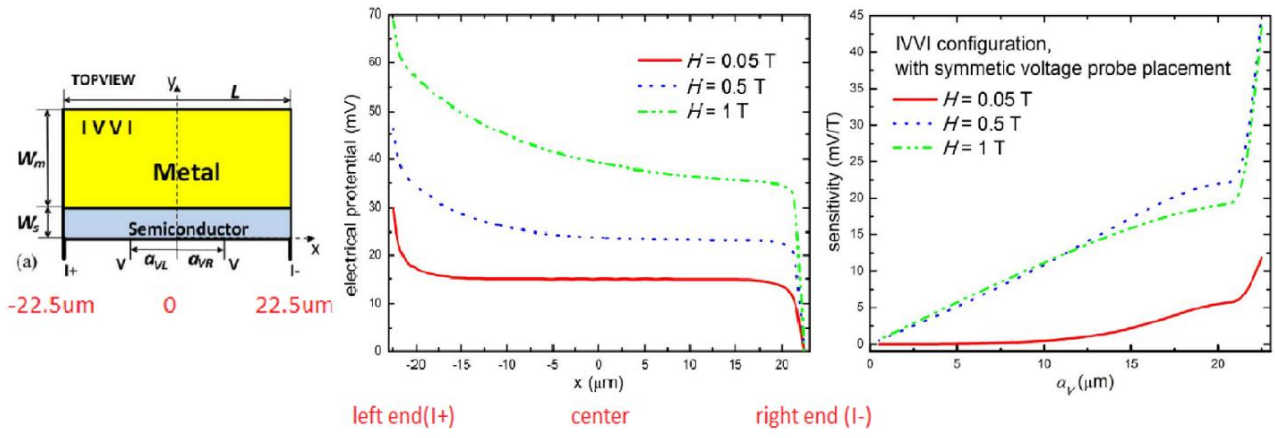

Figure 2.6 Schematic of the device and simulation of electric potential and sensitivity [7]. The two current contacts are at the two ends of the device and the voltage contacts are in the middle.

In their device, the right current lead (I-) is set to ground potential so the potential at the right corner is always zero. Therefore, the electrical potential is high at the left end and gradually decreases to zero towards the right end of the device. We can conclude that if the two voltage probes are infinitely close to the two current probes, the sensitivity becomes the largest. This becomes equivalent to a two-contact rectangular EMR device.

2.3 Extraordinary Magnetoresistance in 2D

In a EMR device made of bulk materials, the material parameters are fixed and adjusting the magnetic field is the only way to vary the EMR response. However, in a 2D EMR device, the charge density of the system is tunable by an external electric field or gate voltage, so it gives a new dimension of control over the MR besides the magnetic field, and the potential to realize greater sensitivity.

One outstanding example of 2D material is graphene. Graphene based EMR devices has also shown interesting magnetoresistance enhancement, with additional advantages of the tunable charge density.

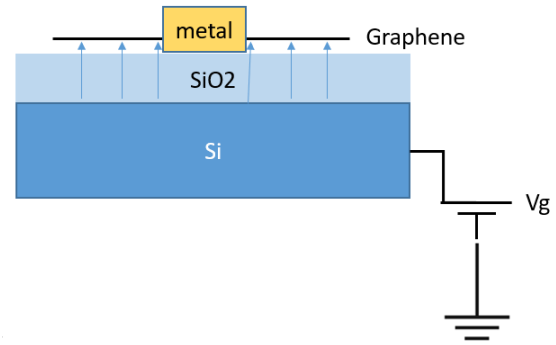

Figure 2.7 Schematic of graphene based EMR device

One of the first publications on graphene-based EMR device with a circular structure used graphene grown by chemical vapor deposition with a central disk made of Ti/Au [4]. Due to its polycrystalline nature, along with impurity residues from transferring CVD graphene from its metal substrate to an oxidized wafer, the graphene devices have a low mobility of only 2500 cm^2/Vs. The largest EMR value achieved in their device is only around 6 (or 600%) at 12T

at room temperature, and the largest sensitivity is 145 Ω/T. These values pale in comparison to the original InSb platform.

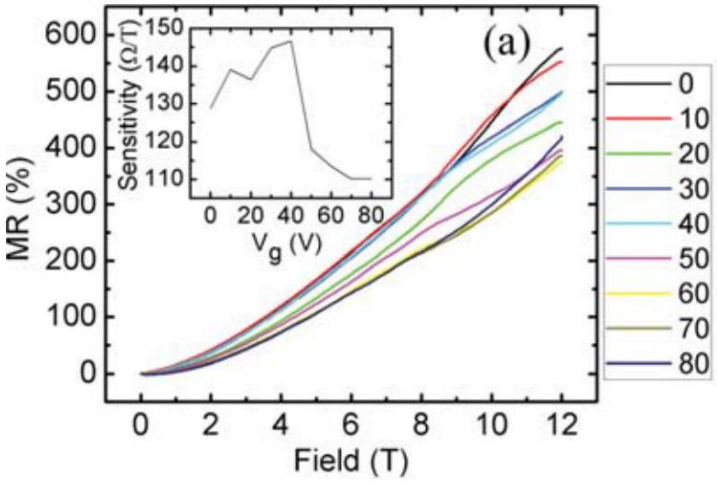

Figure 2.8 MR of the chemical vapor deposition grown graphene device. The colors represent different gate voltages (in V). The inset is the sensitivity with respect to the gate voltage [4].

In the same year, a larger room-temperature MR enhancement of 550 (or 55 000%) at 9 T and a larger two-probe sensitivity of 1600 Ω/T were reported using the mechanically exfoliated graphene instead, in an EMR device with a central metal shunt of Ti/Au. These devices have a higher mobility, varying from 4000 to 7000 cm^2/Vs [5]. Their results were also explored using the simulation performed in a finite element method software, COMSOL.

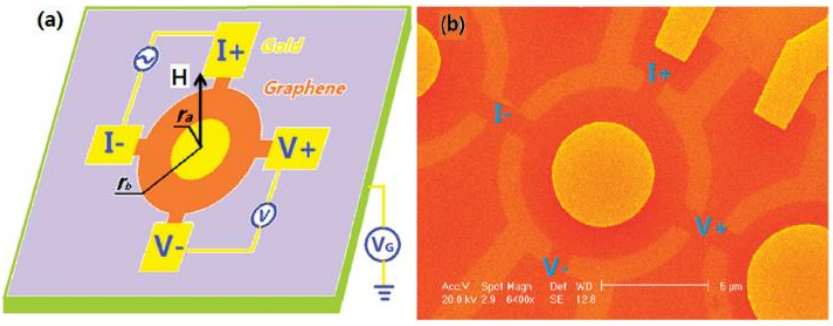

Figure 2.9 Schematic (a) and scanning electron microscope image with fake color (b) of the exfoliated graphene based EMR device [5]. The contact configurations of the EMR measurements of Solin's device, the chemical vapor deposition grown graphene device and the exfoliated graphene device are the same.

The authors also show increasing mobility can further increase MR in calculation.

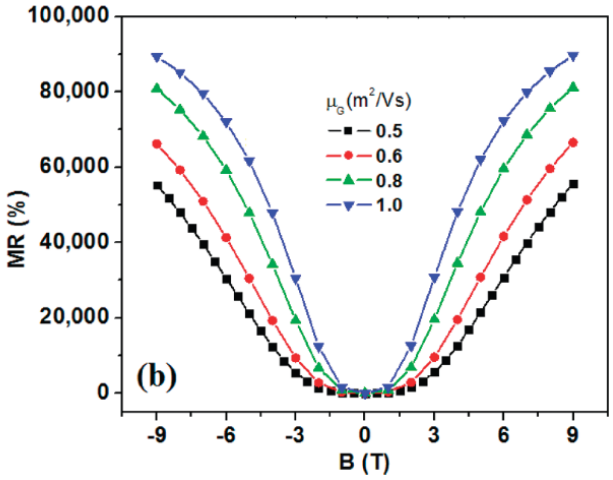

Figure 2.10 Calculated MR vs the magnetic field in different mobility [5]. The MR increases by around a half when the mobility gets doubled.

To understand the effect of the mobility on MR, we need to review the equation (2.13), which is the conductivity tensor of the graphene in this case:

$$\sigma = \begin{pmatrix} \frac{\sigma_0}{1+\mu^2 B^2} & -\frac{\sigma_0 \mu B}{1+\mu^2 B^2} \\ \frac{\sigma_0 \mu B}{1+\mu^2 B^2} & \frac{\sigma_0}{1+\mu^2 B^2} \end{pmatrix}$$

At the high field, the diagonal components of the tensor become negligible and the off-diagonal components dominate. We take one component as an example: $\sigma_{yx} = \frac{\sigma_0 \mu B}{1+\mu^2 B^2} \approx \frac{\sigma_0}{\mu B}$ at high field. When the mobility μ increases at a given field, the conductivity component σ_{yx} decreases, and the

resistance of the sample increases. This causes the MR to increase at the high field since the zero-field conductivity σ_0 should be the same.

Thus, this finding leads us to use encapsulated graphene with much higher mobility in EMR devices, see if graphene can rival or even exceed the state-of-the-art in EMR.

2.4 More Simulations on Extraordinary Magnetoresistance

In 2012, Thomas H. Hewett and Feodor V. Kusmartsev have published an interesting simulation paper on extraordinary magnetoresistance. Their simulation is also based on software COMSOL Multiphysics. The models are based on Solin's device: a circular semiconductor InSb embedded with a central metal Au disk [7].

According to the simulation, MR increases with the conductivity ratio of the metal to the semiconductor σ_m/σ_s. Since σ_m determines the resistance at zero field and σ_s determines the resistance at high field, the larger their ratio is, the larger MR is. The optimal ratio from the simulation is 2430, and MR does not get significantly improved by further increasing the conductivity ratio. Additionally, they also demonstrated that MR increases with the mobility of the semiconductor.

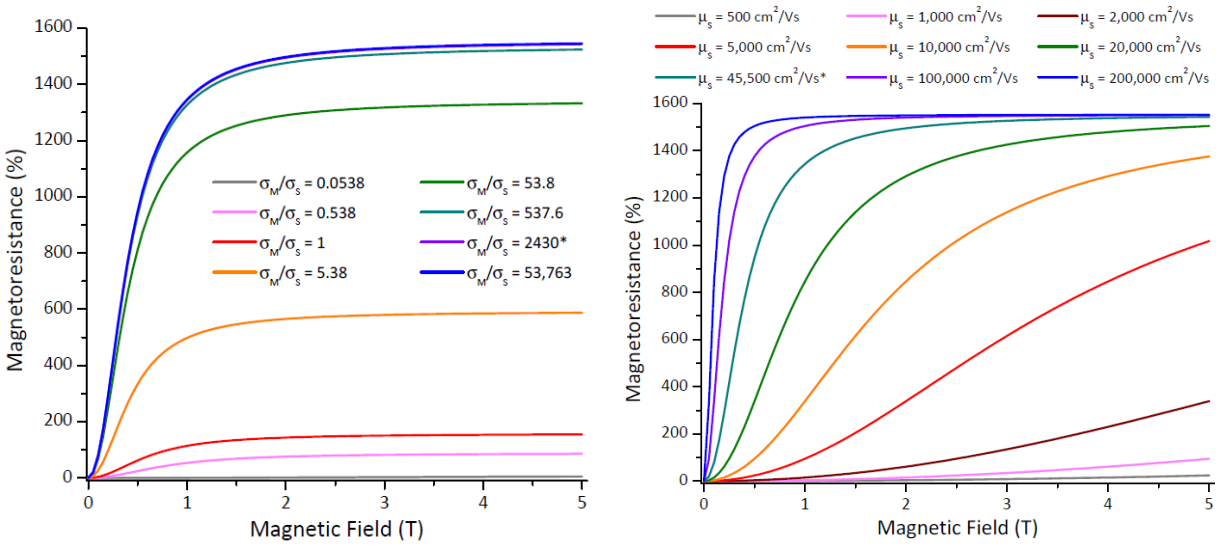

Figure 2.11 Simulated MR vs the magnetic field in different conductivity ratios (left) and mobilities (right) [7].

The contact resistance between the semiconductor and the metal can also impact the MR. In these simulations, MR is the largest without contact resistivity, and begins to decrease as the contact resistivity increases, because the large contact resistivity in the interface between the semiconductor and the metal can impede the current from running through the metal shunt, even at zero magnetic field.

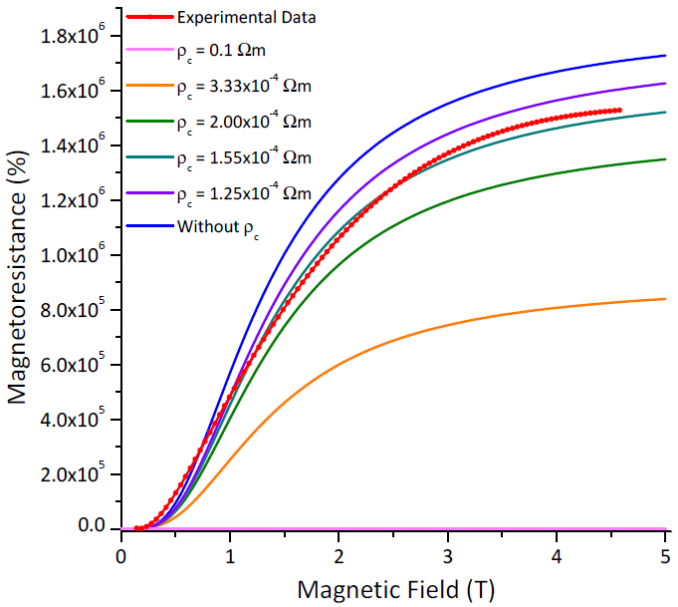

Figure 2.12 Simulated MR vs the magnetic field in different contact resistivities [7].

In a second work on simulation of MR devices, the same authors claimed a multibranched geometry can gives four order of magnitude larger MR than that of the circular geometry with the same materials [2]. We can see the current get squeezed into very narrow channels in 6 locations in the multibranched geometry at high field, contributing to the very large resistance. This multibranched geometry has yet to be studied carefully.

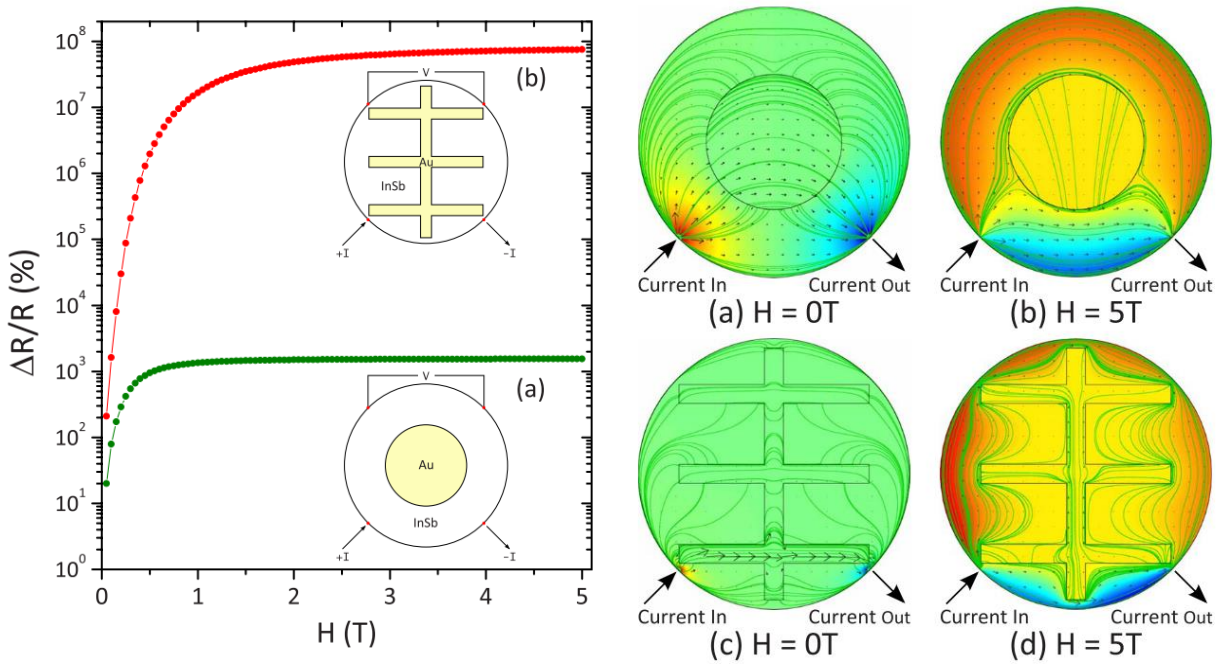

Figure 2.13 Simulated MR vs the magnetic field in a multibranched geometry and a circular geometry (left) and current distribution in the two geometries at zero field and 5 T (right). The background color in the right figures represents the electric potential: brown means high, and blue means low [2].

As for the 2D EMR device, besides the multibranched geometry, Solin et al. have shown that in their simulation, a 10 μm 2D square structure with a square metallic inclusion in the center can give a MR up to 10^5 (or 10^7 percent) for an applied magnetic field of 1 T [8]. This square geometry could be also considered in the future EMR experiment.

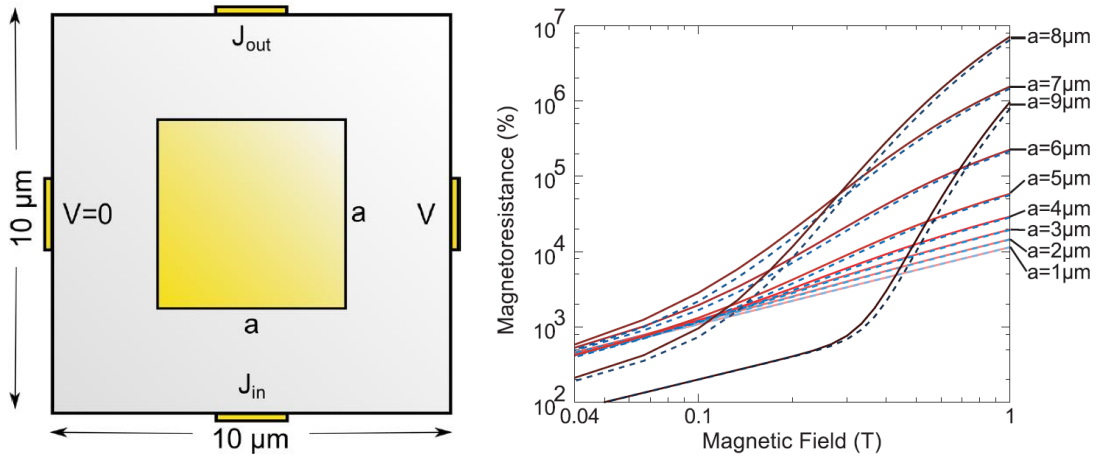

Figure 2.14 A schematic for a 10 μm square EMR device with contacts centered (left) and its MR vs magnetic field for the central metal square of different sizes (right). The dashed lines represent the MR for negative values of the magnetic field [8].

Bibliography

1. S. A. Solin, Tineke Thio, D. R. Hines, J. J. Heremans, *Enhanced Room-Temperature Geometric Magnetoresistance in Inhomogeneous Narrow-Gap Semiconductors*, Science, **289,** 1530 (2000).

2. T. H. Hewett and F. V. Kusmartsev, *Geometrically enhanced extraordinary magnetoresistance in semiconductor-metal hybrids*, Physical Review B **82**, 212404 (2010).

3. S. A. Solin, *Magnetic Field Nanosensors*, Scientific American, **291**, 45 (2004).

4. A. L. Friedman, J. T. Robinson, F. K. Perkins, P. M. Campbell, *Extraordinary magnetoresistance in shunted chemical vapor deposition grown graphene devices*. Appl.

Phys. Lett. **99**, 022108 (2011).

5. Lu, J. et al., *Graphene magnetoresistance device in van der pauw geometry*, Nano Lett. **11**, 2973 (2011).

6. Jian Sun, Chinthaka P. Gooneratne, Jürgen Kosel, *Design study of a bar-type EMR device*, IEEE Sensors Journal, **12**, 1356 (2012).

7. T. H. Hewett and F. V. Kusmartsev, *Extraordinary magnetoresistance: sensing the future*, Cent. Eur. J. Phys., **10**, 602 (2012).

8. Lisa M. Pugsley, L. R. Ram-Mohan, and S. A. Solin, *Extraordinary magnetoresistance in two and three dimensions: Geometrical optimization*, Journal of Applied Physics **113**, 064505 (2013)

Chapter 3:

Extraordinary Magnetoresistance in Encapsulated Graphene Device

The discovery of the extraordinary magnetoresistance (EMR) effect by Solin and coworkers has led to widespread interest in using this phenomenon for magnetic sensing applications [1-3].

On the other side, the advent of graphene in 2004, having tunable and bipolar conductivity, was soon followed by a first generation of graphene-based EMR devices [3-5]. These were built from graphene supported on SiO2, either by mechanical exfoliation or grown by chemical vapor deposition. While a sizable EMR effect was achieved, these devices have generally fallen well short of their semiconductor counterparts.

Recently, significant improvement in graphene devices has been realized through the encapsulation of graphene in flakes of hexagonal boron nitride (hBN), an atomically-flat 5 eV gap insulator with a honeycomb lattice alternately arranged by B atoms and N atoms [6]. hBN has a layered structure similar to the graphene lattice, and it can be easily exfoliated into thin 2D layers, even down to monolayer. Weak van der Waals forces that combine the hBN interlayers can be used to make the heterostructure with graphene.

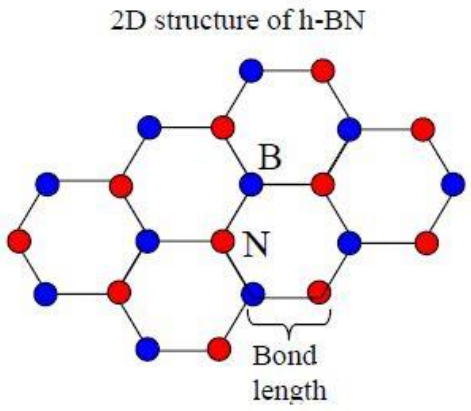

Figure 3.1 Schematic of honeycomb lattice structure of boron nitride.

In encapsulated graphene devices, the hBN protects the graphene from extrinsic sources of disorder including e.g. water and adsorbed hydrocarbons, and much higher quality transport is achieved [7]. Since increased device mobility has been linked to an enhanced EMR as show in Section 2.4, it may be worthwhile to investigate EMR devices using encapsulated graphene.

Here we fabricate EMR devices based on flakes of monolayer graphene sandwiched between hBN flakes, each approximately 30 nm thick. Monolayer graphene and hBN are exfoliated onto oxidized silicon wafer chips and then assembled into stacks using a dry-transfer technique [8]. The device geometry is defined by reactive ion etching to create a disk with outer radius r_b, and a concentric circular hole with radius r_a is also removed. Electrical contacts are made by depositing a 4/80-nm-thick layer of Ti/Al, yielding several voltage and current leads at the external disk edge, and the central metal shunt that connects to the entire inner perimeter. For uniformity, up to several devices were made from a single graphene/hBN stack, as shown in Figure 3.2 (a). Electronic transport measurements in both two- and four-terminal configurations were performed at 300 K in

a Quantum Design PPMS with a 9 T magnet. A gate voltage, V_g, applied to the conducting Si substrate is used to control the carrier density and hence conductivity of the graphene. Devices are made with varying ratios of the metallic shunt to outer radius, so that $r_a/r_b = 0$ corresponds to a graphene device without the metal shunt and $r_a/r_b = 1$ corresponds to a pure metal disk without graphene.

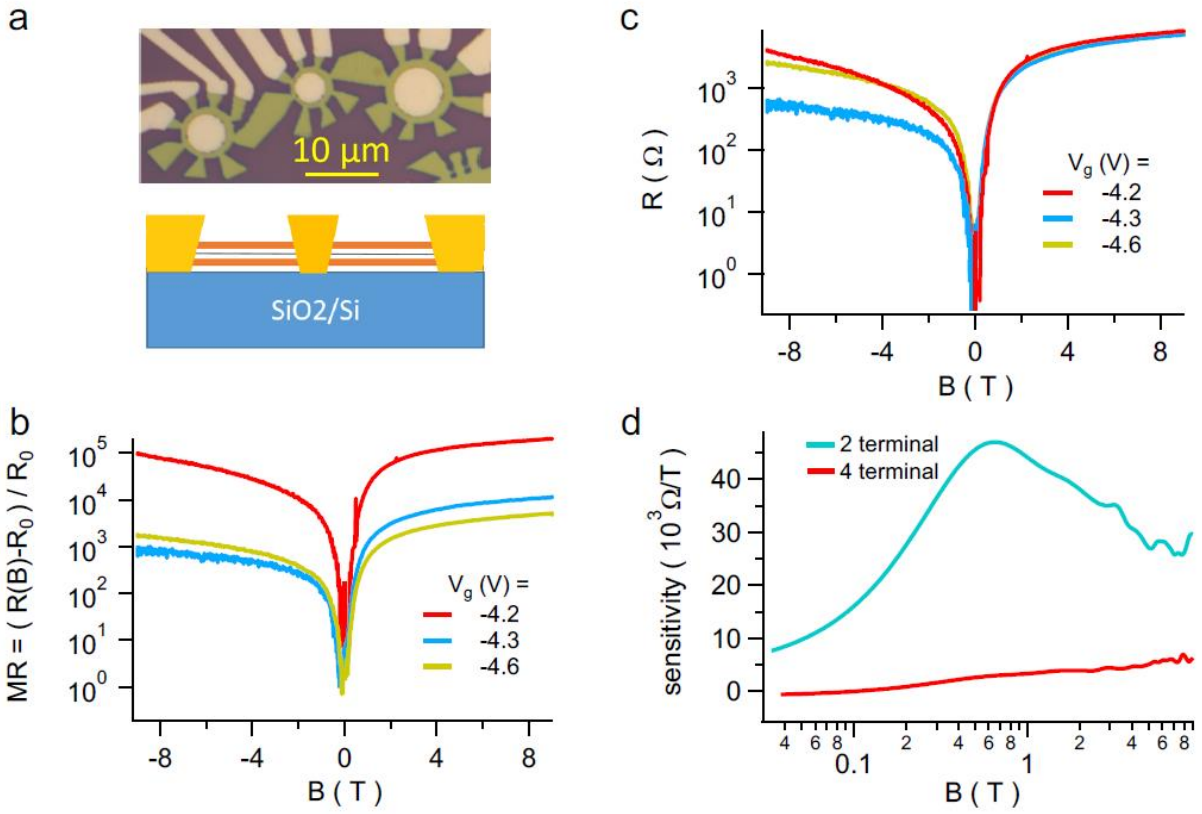

Figure 3.2 (a) Microscope image of a set of three devices fabricated from a single graphene/hBN stack. Contacts and central metallic shunt are made by edge contacts to exposed graphene. Schematic shows side view of device geometry. (b) Magnetoresistance, $MR = [R(B) - R_0]/R_0]$, for the device with highest observed EMR effect at room temperature. The MR shows a strong dependence on back gate voltage. (c) The as-measured (un-normalized) resistance for the same gate voltages as in (b). The resistance itself shows little change with V_g. (d) The sensitivity, dR/dB, for the same device, at $V_g = -4.2V$. The red (cyan) trace was calculated from data measured in a four- (two-) terminal configuration. Note the log-scale of the B-field axis.

Figure 3.2 (b) shows the normalized magnetoresistance, $MR = [R(B) - R_0]/R_0]$, from the device having the highest observed EMR effect, for three closely spaced gate voltages which nonetheless exhibit a remarkable variation in magnitude of the EMR. In contrast the measured resistance, $R(B)$, for the same three traces is shown in Figure 3.2 (c) where, at least for positive magnetic field, the resistances overlap almost identically. Thus, the variation in MR must be due to changes in the value of $R_0(V_g)$.

Typically, circular EMR devices are measured using four contacts spaced at 90 degree relative to each other, but in this case device design constraints or poor electrical contacts led us to use four neighboring contacts on one side of each device instead. Moreover, the metallic shunt is not always concentric with the outer device radius. These features are known to lead to asymmetry in the EMR [9], and are likely responsible for the observed asymmetry between positive and negative magnetic fields in these traces, as shown in Figure 3.2 (b) and (c).

While MR is a standard figure-of-merit for EMR devices, it depends on the value of R_0 which, in these devices, is strongly dependent on the applied gate voltage. Yet the variation of resistance when a field is applied is the quantity we are most interested in, particularly as R(B) is strongly non-linear, and much of the field response occurs over the lowest one or two teslas. Thus, in addition to plotting the MR, we also plot in Figure 3.2 (d) the sensitivity, or dR/dB, that has also used to characterize the EMR response [4, 5, 10]. Here we discover that the sensitivity of encapsulated graphene can greatly exceed that of graphene-on-oxide devices.

In particular, Figure 3.2 (d) shows the sensitivity calculated for the same device at $V_g = -4.2V$, taking the derivative for data measured in a four-terminal configuration, and also for the same

device and V_g but with data acquired in a two-terminal voltage-biased configuration. The four-terminal measurement yields a modest slope of order dR/dB≈1 kΩ/T which can be anticipated from the resistance change seen in Figure 3.2 (c), and which is roughly the same as the best sensitivity reported for graphene-on-oxide devices [5]. However the two-terminal measurement yields a far higher sensitivity across the entire field range, with a maximum approaching 50 kΩ/T. Moreover, while the MR is dramatically affected by small changes in the gate voltage, the resistance itself is not, and therefore such large sensitivities do not require fine-tuning of the gate voltage.

The reason for this remarkable difference between the two- and four-terminal measurements is simply that the two-terminal, by definition, captures the entire voltage drop across the device while the four-terminal picks out a reduced value. This effect was theoretically described by Sun et al. in a design study of rectangular EMR devices, using numerical calculations that revealed an enhanced sensitivity as the voltage contacts in a four-terminal configuration were brought increasingly closer to, and eventually merged with, the current contacts, as shown in Figure 2.6. Taken together, it appears the highest sensitivity EMR devices can be fabricated in a simple two-terminal configuration, and that the platform of high mobility encapsulated graphene enables devices to be tuned to regions of highest sensitivity (highest resistance change for a given applied field).

In Figure 3.3 we show a comparison of both the MR and the sensitivity (calculated using data from two-terminal measurements) for two sets of devices. In the first set shown in Figure 3.3 (a) and (c), the outer diameter of the device was fixed at 5.5 μm but the ratio r_a/r_b of the shunt to outer device diameters was varied. In contrast in Figure 3.3 (b) and (d), the ratio was fixed at 0.74 while

the outer diameter was varied. In prior EMR studies, the MR is generally found to reach a maximum for a shunt-to-outer diameter ratio of 3:4 [9], and on the whole this is what we see in Figure 3.3 (a), along with the MR decreasing with the ratio. However, the trend of the sensitivity data is precisely the opposite, namely, the smallest ratio yields the largest sensitivity. At first glance this is surprising, but we note the MR is a four-terminal measurement and thus is sensitive to the change in voltage at a pair of contacts located close to the metallic shunt, while the two-terminal data from which the sensitivity is determined captures the potential drop through the entire device, including regions far from the shunt.

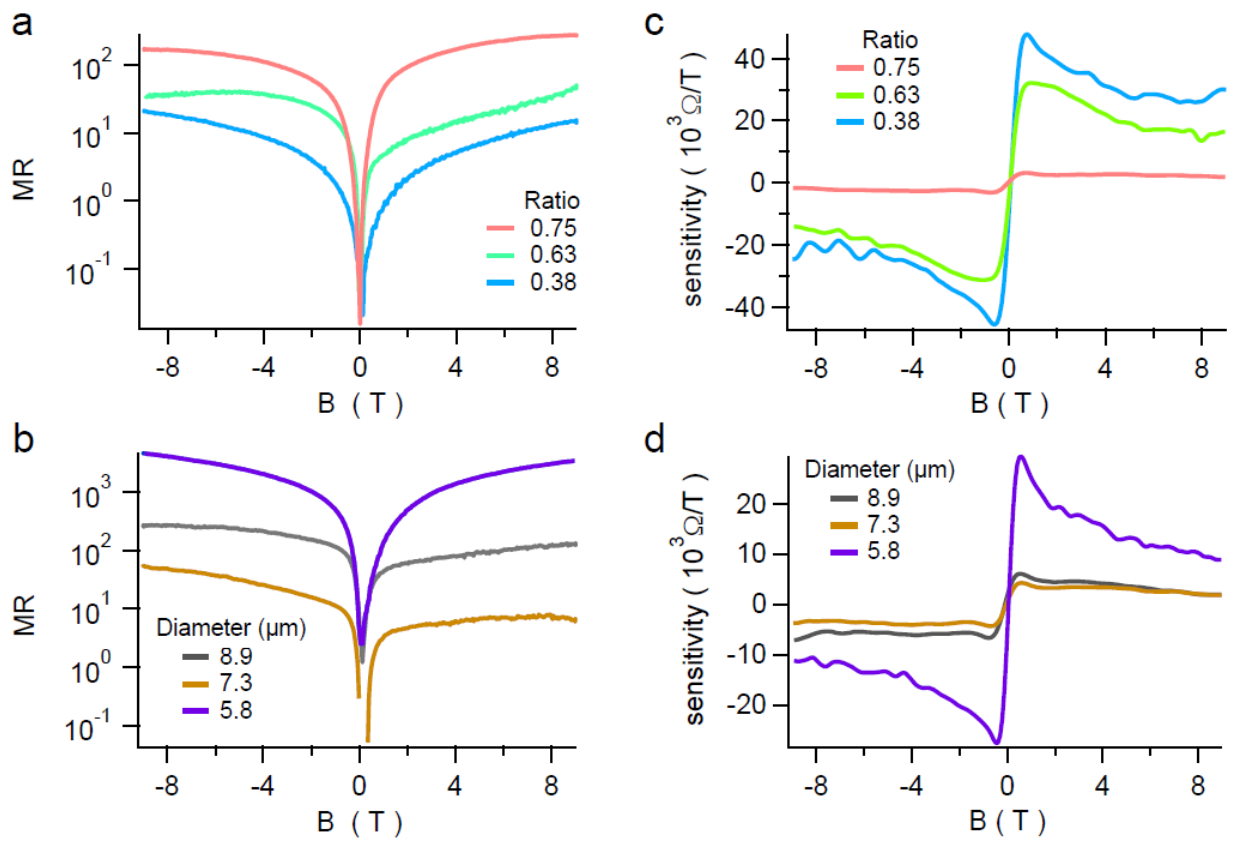

Figure 3.3 The MR (a) and sensitivity (c) for devices with varying shunt-to-outer diameter ratios but fixed outer diameter of 5.5 μm. The MR (b) and sensitivity (d) for devices with varying outer diameter at fixed ratio $r_a/r_b = 0.74$. Here all MR traces are measured in a four-terminal configuration, while the sensitivity is calculated from data acquired in a two-terminal voltage-biased measurement.

In a magnetic field, the charge carriers are deflected from the center of the shunt. The larger the magnetic field is, the more charge carriers pass through the two sides of the device. However, in a fixed magnetic field, the smaller the ratio is, the more charge carriers also pass through the two sides, and thus, the measured resistance is higher since the two sides are the high-resistance graphene area.

The data for varying the overall diameter is less conclusive. In Figure 3.3 (b) there is no clear dependence of the MR on device size. The sensitivity is found to be largest for the smallest diameter device, but it is the middle device that has the smallest sensitivity (and also smallest MR).

Encapsulated graphene devices can vary widely in quality. During the process in which the hBN/graphene/hBN stack is assembled, it is common to find regions with bubbles, wrinkles, or torn graphene. As much as possible we attempted to fabricate devices from the smooth regions, but it is possible that some of the variation noted here arises from inhomogeneities, and also asymmetry in the device fabrication (e.g. an off-center metallic shunt).

In conclusion, we have investigated the extraordinary magnetoresistance effect in encapsulated graphene devices. We find the magnetoresistance is enhanced by over four orders of magnitude from its zero field value in the best devices. We also find enhanced values of the sensitivity, dR/dB, reaching values of 50 kΩ/T, which exceeds prior reports in graphene-based devices by a factor of

up to 30. Encapsulated graphene is thus a promising platform for high-sensitivity measurements of magnetic fields using the EMR effect.

Note: The study on sensitivity is still a work in progress. The final form will be presented in the paper to be submitted later. The title of the paper should be: Highly sensitive extraordinary magnetoresistance in encapsulated monolayer graphene devices.

Bibliography

1. S. A. Solin, T. Thio, D. R. Hines, and J. J. Heremans, Science 289, 1530 (2000).
2. S. A. Solin, D. R. Hines, A. C. H. Rowe, J. S. Tsai, Y. A. Pashkin, S. J. Chung, N. Goel, and M. B. Santos, Applied Physics Letters 80, 4012 (2002).
3. T. Hewett and F. Kusmartsev, Central European Journal of Physics 10, 602 (2012).
4. A. L. Friedman, J. T. Robinson, F. K. Perkins, and P. M. Campbell, Applied Physics Letters 99, 022108 (2011).
5. J. Lu, H. Zhang, W. Shi, Z. Wang, Y. Zheng, T. Zhang, N. Wang, Z. Tang, and P. Sheng, Nano Letters 11, 2973 (2011).
6. Y. Kubota, K. Watanabe, O. Tsuda, and T. Taniguchi, Science 317, 932 (2007).
7. C. R. Dean, A. F. Young, I. Meric, C. Lee, L. Wang, S. Sorgenfrei, K. Watanabe, T. Taniguchi, P. Kim, K. L. Shepard, and J. Hone, Nature Nanotechnology 5, 722 (2010).

8. L.Wang, I. Meric, P. Y. Huang, Q. Gao, Y. Gao, H. Tran, T. Taniguchi, K.Watanabe, L. M. Campos, D. A. Muller, J. Guo, P. Kim, J. Hone, K. L. Shepard, and C. R. Dean, Science 342, 614 (2013).
9. S. A. Solin and T. Zhou, in International Conference on Solid State Devices and Materials (The Japan Society of Applied Physics, 2001) p. 570.
10. J. Sun, C. P. Gooneratne, and J. Kosel, IEEE Sensors Journal 12, 1356 (2012).

Chapter 4:

P-N Junction:

Theory, Experiment and Simulation

4.1 Basics of P-N Junction

An intrinsic semiconductor has no impurities and should have a balance of positive charges (holes) and negative charges (electrons). Additional charges can be added when the impurities (dopants) are introduced into a semiconductor. In a doped or extrinsic semiconductor, the number of the positive charges and the number of negative charges are generally not equal any more. The p-type semiconductor has larger hole concentration than electron concentration, and the n-type one has more electrons than holes.

When a p-type semiconductor and a n-type semiconductor join, electrons near the p-n interface diffuse into the p region and combine with holes leaving behind positively charged ions which cannot move in the n region, and eventually form a negatively charged region in p region. In the same way, holes near the interface diffuse into the n region and leaves the negatively charged ions in the p region, and eventually form a positively charged region in n region. A strong electric field appears near the interface due to the unbalanced charges, which counterbalances the diffusion of

both types of charges. Eventually the two opposite charged regions near the interface reaches the equilibrium state, and a p-n junction is formed.

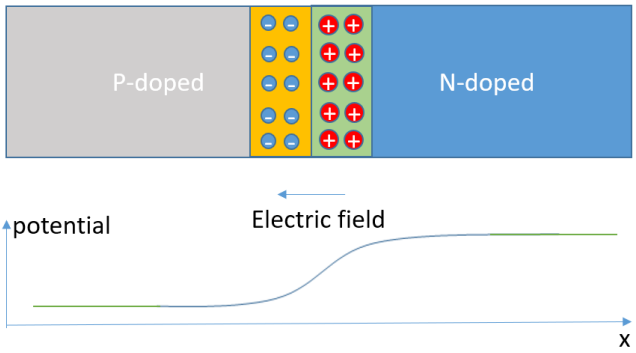

Figure 4.1 Schematic of a p-n junction and its electric potential.

The p-n junction is widely used as diode in industry, which only allows current to move in one direction since the electric potential difference in the junction blocks electrons to move to a lower-potential region. We can also understand this effect as the electric field in the junction stops the electrons from moving to its opposite direction.

4.2 Metal-graphene Junction

Graphene has many properties in common with semiconductors. After graphene gets into contact with the metal, charge doping from the metal changes the electric potential and charge density of graphene in the contact area. Therefore, a metal-graphene junction is formed.

There are two types of metal-graphene contacts: surface contact and edge contact. The surface contact is an area contact, but the edge contact occurs only along a line since graphene is a one-atom-thick 2D material.

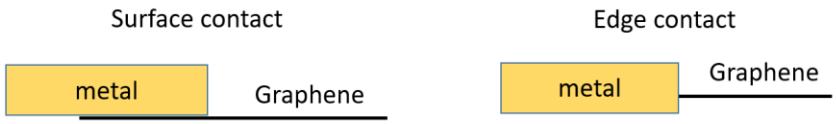

Figure 4.2 Schematic side view of surface contact and edge contact between graphene and metal.

4.2.1 Surface Contact between Graphene and Metal

When the metal surface contacts is made with graphene, for several metals Al, Ag, Cu, Au and Pt(111) the surfaces have only physisorption to the graphene so the bonding is weak and the electronic structure of graphene does not change. Certain other materials including Co, Ni, Pd, and Ti surfaces, however, covalently bind and interact more strongly with graphene due to chemisorption, and can perturb the electronic structure of graphene significantly [1]. When the metal meets graphene, charges transfer between them due to the differences of their work functions (in the simplest picture), and graphene get either n-doped or p-doped. Adsorption of graphene on Al, Ag, Cu, Co, Ni, Pd (111) and Ti (0001) surfaces lead to n-type doping, while Au and Pt (111) substrates lead to p-type doping of graphene.

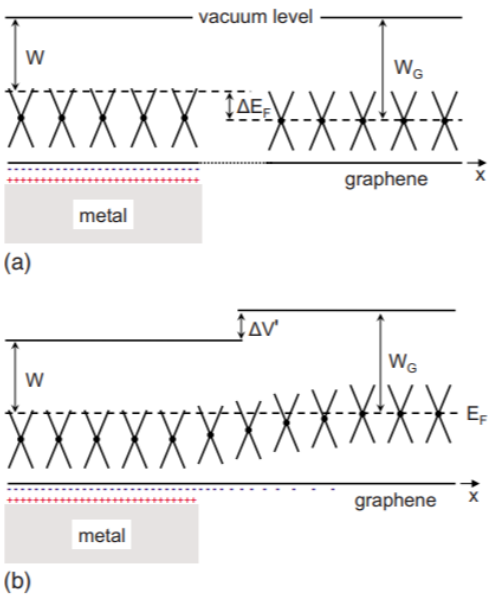

Figure 4.3 Schematics of a graphene partly in contact with a metal showing the potential shift caused by the charge transfer [1]. The upper plot shows two separate graphene: the graphene on the metal surface is n-doped in this case, and the graphene far away from the metal is still free standing and unperturbed. The lower plot shows when the two graphene pieces connect, the rearrangement of the charges give rise to the potential shift and band bending.

In a paper by Xia and Avouris, et al., it was further reported that charge doping from surface-contact metal can even cause asymmetries in the traces of resistance [2].

The metal contacts made by palladium and gold dope both the graphene underneath them and over a short range into the graphene channel (that is not covered by metal) close to the contacts due to direct contact and interaction between palladium and graphene. However, the applied gate voltage can change the carrier type in the graphene channel far from the contact. For example, a metal that n-type dopes graphene will lead to a pn-junction when the bulk of the graphene is gated to p-type conduction.

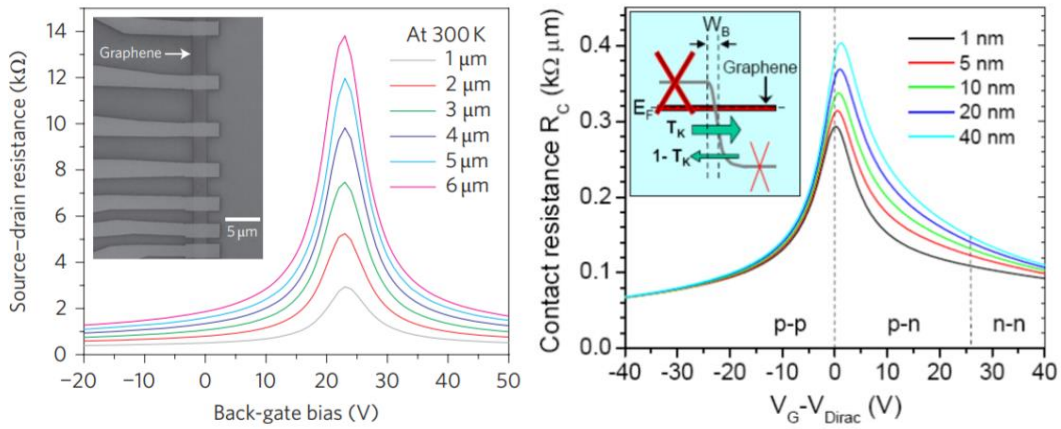

Figure 4.4 Measured room-temperature resistance (left) and calculated contact resistance (right) of a graphene partly covered by metal as a function of gate voltage [2]. Both plots have asymmetries in which n branches are higher than the p branch in the traces, suggesting p-type doping in graphene. And the asymmetries increase with the length (left) of the graphene channel and characteristic width (right). The inset in the left plot is scanning electron image of the graphene device covered by 7 metal contacts made from palladium and gold. And the inset in the right plot is schematic of the potential of graphene vs the distance, the left and right parts of the profile represent the potentials of graphene under the metal and in channel respectively.

According to their calculation, the energy differences between the Dirac point and Fermi level in the metal-doped graphene ΔE_{FM} and graphene channel ΔE_{FG} both change with the gate voltage. ΔE_{FG} changes more with the gate voltage than ΔE_{FM} does suggesting the metal could screen the electric field and therefore the graphene covered by metal is less sensitive to the gate voltage.

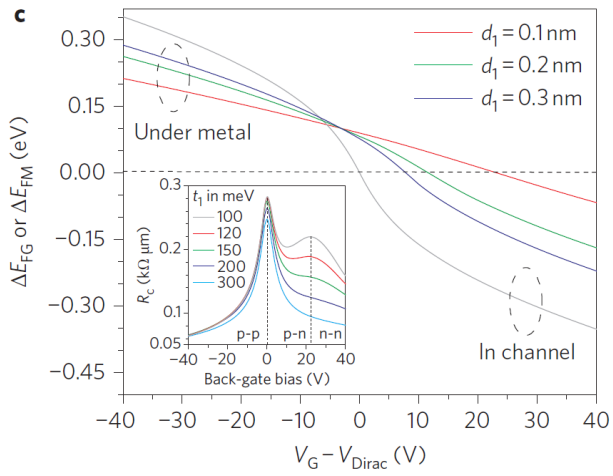

Figure 4.5 Calculated energy differences as a function of gate voltage [2]. The red, green and blue traces are for the graphene under the metal, and the grey trace is for the graphene channel without the metal coverage.

The authors also demonstrated that the contact resistance is not sensitive to the different potential profiles (linear, exponential, etc.) used in the calculation. Therefore, they used the exponential profile

$$U(x) = U_0 \frac{1}{1 + e^{2\ln(3(x/W_B - 1))}} \tag{4.1}$$

for their calculations. W_B is the characteristic width over which the potential of graphene changes by a half.

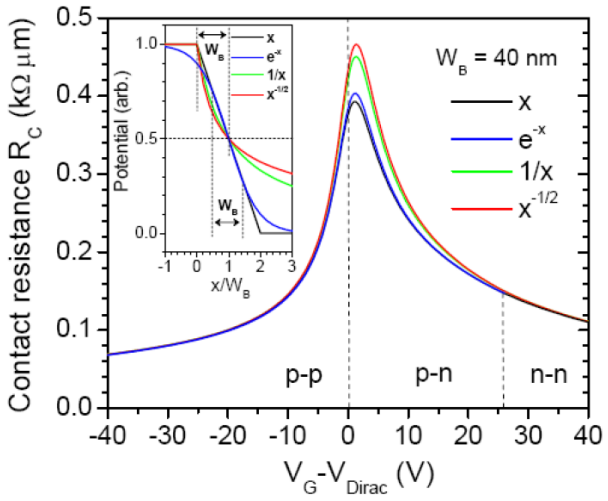

Figure 4.6 Calculated contact resistance as a function of gate bias using different potential profiles with the fixed W_B=40 nm [2]. The inset are different potential profiles used in calculation.

They calculated the contact resistance as a function of the gate voltage for titanium-covered graphene and showed the asymmetry of its trace is opposite to that of palladium-covered graphene. In the titanium case, the n branch of the contact resistance is lower than its p branch. Therefore, titanium induces n-type doping in graphene.

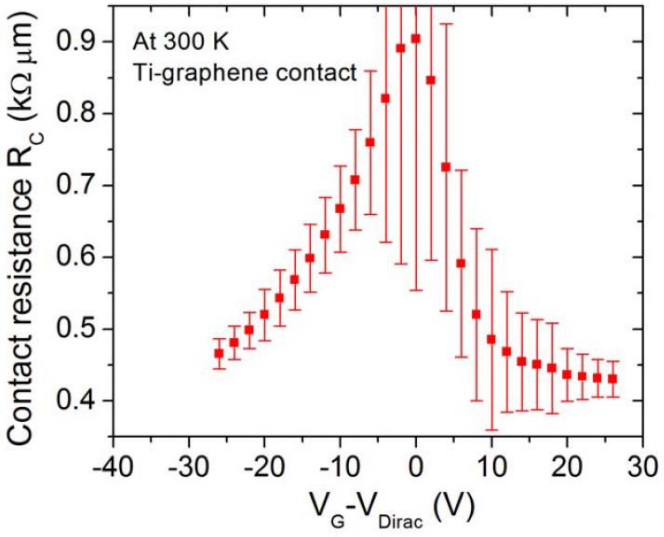

Figure 4.7 Calculated contact resistance vs the gate voltage for titanium-covered graphene [2].

4.2.2 σ Bonds in Edge Contact and π Bonds in Surface Contact

In a theoretical paper published in 2014, Gao and Guo have shown that compared to the surface contacts, graphene edge contacts can contribute to a much lower contact resistance due to their shorter bonding distances, stronger overlaps of electron orbitals, and lower and narrower interface barriers. The shorter binding distance leads to larger overlap between electron wavefunctions of metal atoms and edge atoms, and therefore, the larger binding energy and the smaller interface barrier height [3].

They used *Ab initio* density functional theory (DFT) calculations and non-equilibrium Green's functions (NEGF) simulations and demonstrated that different contact resistances can be achieved in different edge terminations in the metal-graphene edge contact due to different binding distances, overlaps of electron orbitals, and barriers across the interface from different chemical interaction.

			Cr-X (Å)	X-C (Å)	Binding energy (eV/carbon)
Side	(100)	X = C	1.83	n/a	0.32
	(110)	X = C	2.02	n/a	0.75
Edge	(100)	X = C	0.64	1.44	6.8
		X = O	1.26	1.41	5.5
	(110)	X = C	1.42	1.43	5.5
		X = O	1.44	1.35	3.4
		X = H	2.31	1.12	0.11
		X = F	2.18	1.39	0.12

Table 4.1 The binding distances and binding energies for Cr-graphene surface and edge contacts with edge terminations indicated by X [3]. The Cr-C terminations are highlighted.

Dean et al. also claimed in the surface contact between graphene and metal, the lack of surface bonding sites in π bonds on the surface of graphene causes the lack of chemical bonding, strong orbital hybridization and large contact resistance [4]. Their experiments showed the contact resistance for edge contacts can be remarkably low (as low as 100 ohm·μm in some devices) in the 1D atomic edge of the encapsulated graphene in contact with the metal made by 1 nm Cr/15 nm Pd/60 nm Au, and the contact resistance is also asymmetric to the gate voltage: n branch of the contact resistance is much lower than its p branch.

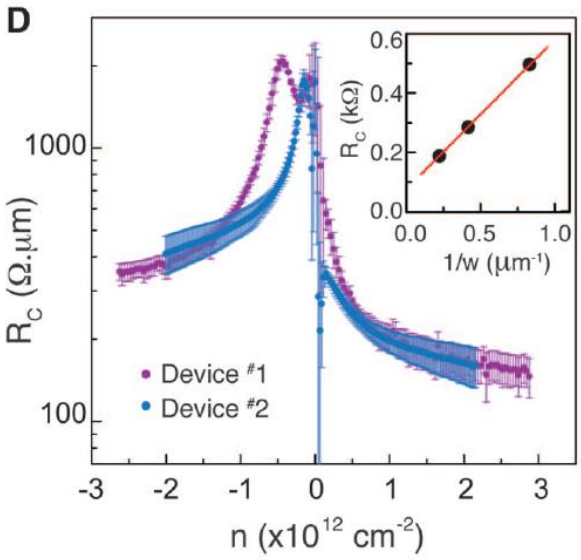

Figure 4.8 Calculated contact resistance vs the charge density (proportional to the gate voltage) for two edge-contact graphene devices [4].

They also suggested that reactive ion etch process used in sample fabrication may bring some additional interfacial species, such as oxygen, which can help to improve bonding and increase the transmission of charges through the barrier of the contact resistance. They also showed that the

high mobility of graphene encapsulated by two boron nitride thin films can lead to ballistic transport in graphene at 1.7K since the mean free path is greatly improved.

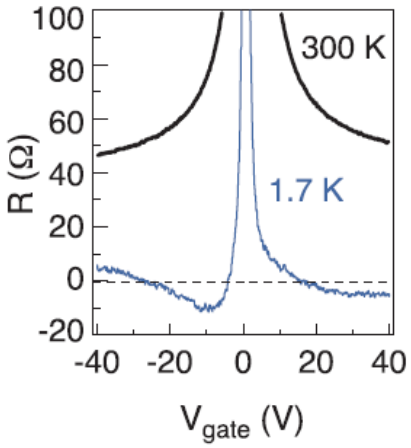

Figure 4.9 The plot of measured resistance vs gate voltage in a square encapsulated graphene device at 300K and 1.7K [4]. The negative resistance at 1.7K suggest the charges get into the ballistic transport regime.

Goddard et al., gave more details in the bonding of surface and edge contact [5]: In the surface-contact graphene interfaces, only the π orbitals of carbon atoms contribute to the cohesion to the surface metals; however, in the edge-contact metal-graphene interfaces, both the π orbitals and σ orbitals contribute to the cohesion. Either unpaired (zigzag) or involved in a weakened in-plane π bond (armchair), the σ electrons in the surface carbon atoms could play substantial roles in cohesion and hence transmission of charges.

4.3 Experimental Discovery of Asymmetry in Gate-Voltage-Dependent Resistance of Edge-Contacted Graphene

In principle an advantage of graphene-based EMR devices is the inherent tunability of graphene via applying gate voltages to the substrate. In regular graphene devices without a shunt, the resistance is a maximum at charge neutrality and falls off with increasing electron or hole charge density; this is the so-called "Dirac peak" [7]. In shunted EMR devices made of graphene on oxide, the resistance maximum survives but is rather broad [8, 9].

In contrast, in our encapsulated graphene EMR devices mentioned in Chapter 3 the resistance maximum also survives but it invariably shows a strong asymmetry near charge neutrality; and more importantly, the resistance can become negative. An example is shown in Figure 4.10, which contains the zero-field resistance corresponding to the traces in Figure 3.2 (b), for devices with the same ratio but varying outer diameters. In encapsulated graphene devices, the mean free path of charge carriers can be of order μm even at room temperature [4], which is approximately the spacing between the shunt and outer diameter of our devices. Thus transport in these devices is nearly ballistic, and as a consequence "negative" resistances may arise due to geometric resonances in scattering.

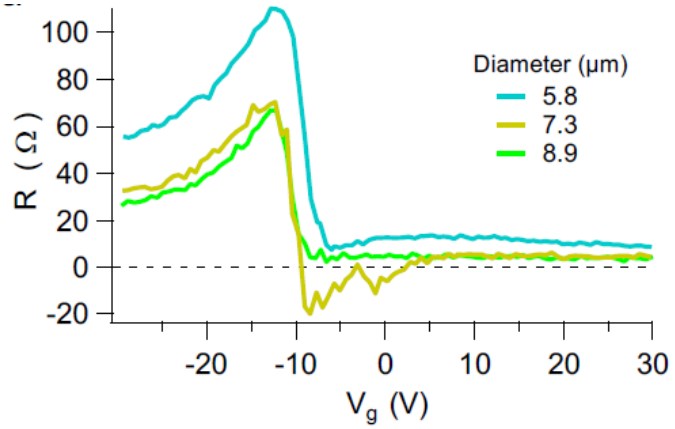

Figure 4.10 Asymmetry in the gate-voltage-dependent resistance at zero magnetic field and room temperature, in three devices of varying diameters.

We compare the asymmetries in gate-voltage-dependent resistance at zero magnetic field and room temperature in three different experiments, and see the asymmetries in the edge-contacted graphene are much stronger than that in the surface-contacted graphene. This could arise from the better overlap of the metal and carbon orbitals in the edge-contacted graphene than in surface-contacted graphene, where the metal atoms encounter the graphene π orbitals that will not form covalent bonds.

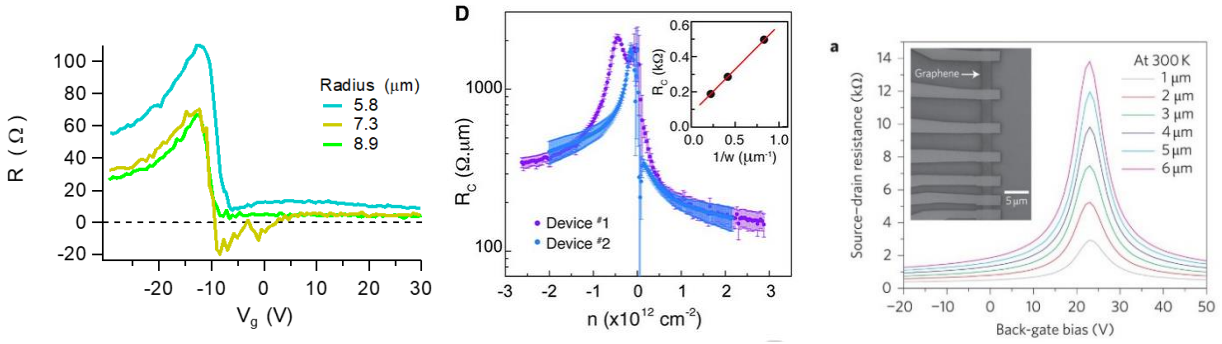

Experiment data of our EMR device | Corry's edge-contacted device | Xia's Surface-contacted device

Figure 4.11 Comparison of the asymmetries in gate-voltage-dependent resistance at zero magnetic field and room temperature from tree different experiments.

4.4 Two Models

The metal shunt in our EMR graphene devices are composed of titanium and aluminum. The origin of asymmetry in the zero-field resistance in our edge-contacted graphene devices arises from the p-n junction that can occur at the interface of graphene with metals, especially titanium which

directly contacts graphene. This issue has been extensively investigated in the context of metallic contacts to graphene devices.

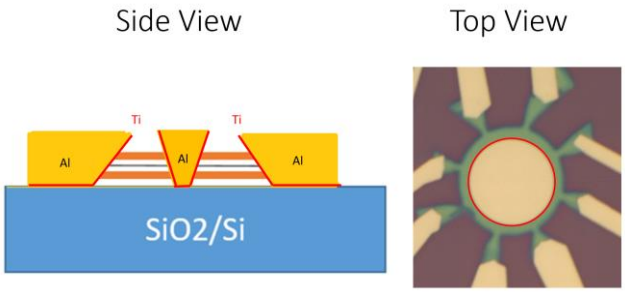

Figure 4.12 Schematic of metal contacts and graphene on Si wafer (left) and photo of our EMR device (right). The red circle on the right plot represents the titanium metal, which directly contacts graphene.

According to Khomyakov et al., the work function of the free-standing graphene is 4.5eV, and work function of the Ti-covered graphene is 4.17eV [1]. Since the work function of graphene is given by the position of the Fermi level ($W = -E_F$), Fermi energy of a free-standing graphene is -4.5eV, and Fermi energy of the Ti-covered graphene is -4.17eV relative to the vacuum level. Our models are based on edge-contacted graphene, and we expect the Fermi energy of graphene at the contact interface of graphene and Ti should still be -4.17eV. Therefore, we can get the schematic of the potential of graphene changing with the distance from the edge of the metal shown in the picture below.

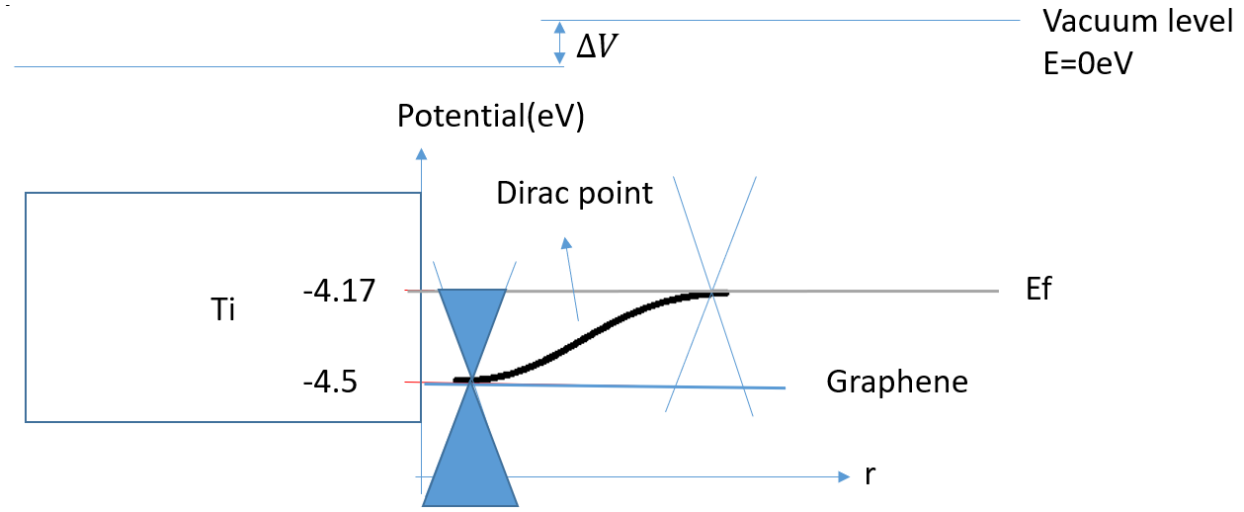

Figure 4.13 Schematic of the potential of graphene changing with the distance from the edge of the metal. The black thick line is the profile of Dirac point.

Set the energy of the Dirac point as zero, we compare the energy difference between the Fermi level and Dirac point (E=0):

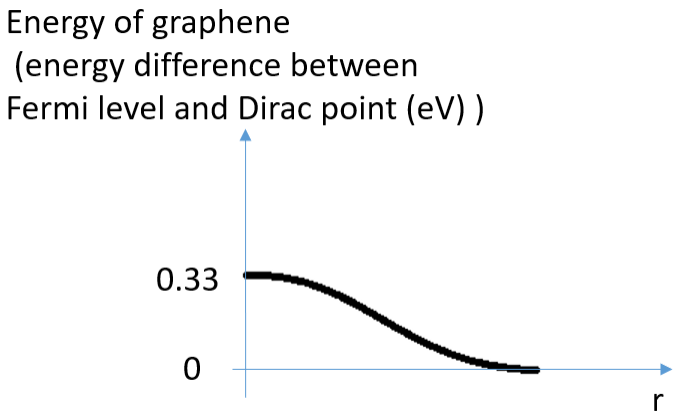

Figure 4.14 Schematic of the energy difference between the Fermi level and Dirac point. The energy difference decreases as the distance from the metal edge increases.

We use the finite element simulation software COMSOL. The details of this software and the simulation are in the Appendix. To get the resistance or voltage between two voltage probes in the device, we need to get the conductivity of the device for simulation. The process is shown below:

Potential Profile

=> Energy difference between Fermi level and Dirac point

=> charge density

=> conductivity of the device = conductivity (energy)

=> current or electric potential distribution in the device

=> resistance or voltage between two points in the device

We use the exponential profile given by Avouris et al. but do some modification to their equation (4.1) to make it fit our case, the potential of graphene in our device is:

$$P(x) = 0.33 \times \frac{1}{1 + e^{2\ln\left(\frac{3(x-r)}{W_B}\right)}} \tag{4.2}$$

r is the radius of the circular metal disk. $P(x = r) = 0.33$ and $P(x = \infty) = 0$.

The exponential profile from our equation is plotted in Mathematica to confirm that it fits the plot of energy difference between the Fermi level and Dirac point shown in the figure above.

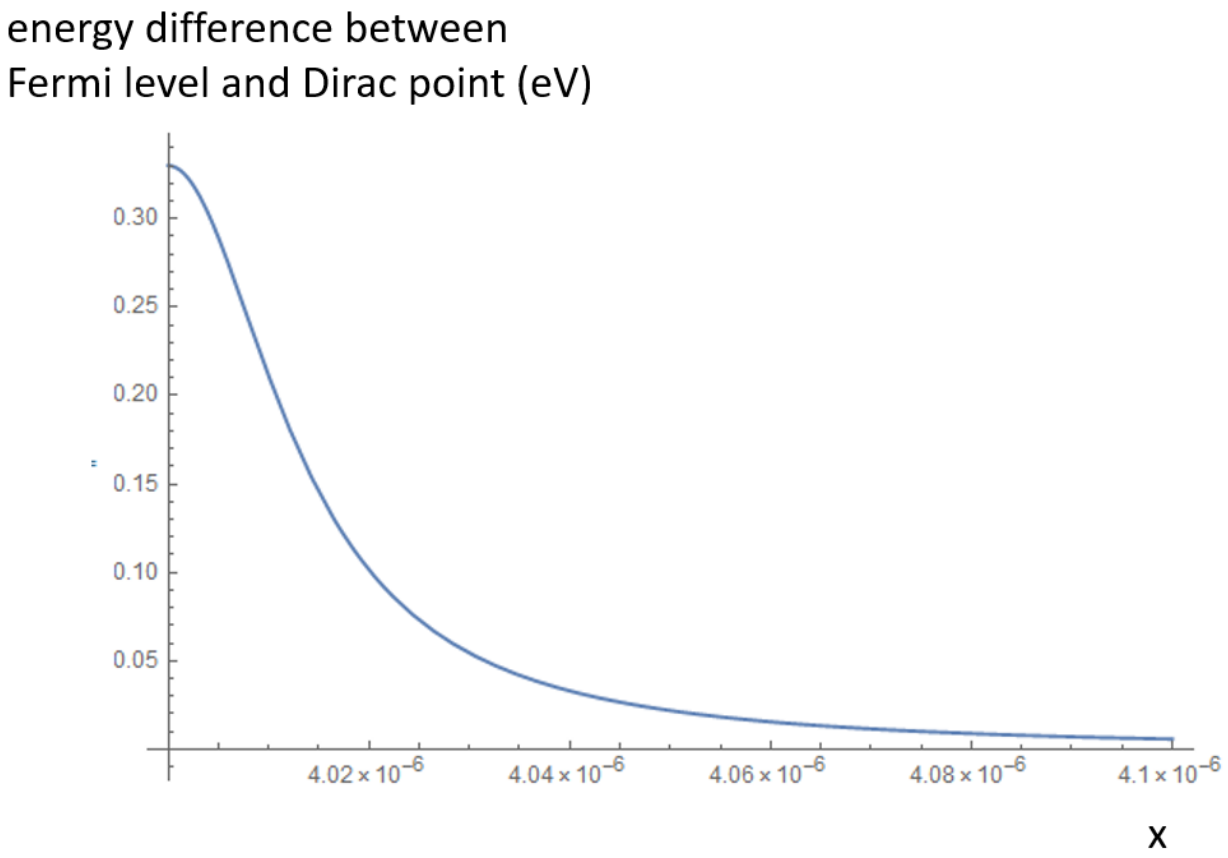

Figure 4.15 Plot of exponential profile from our equation (4.2) as a function of distance away from the metal edge, by Mathematica. The radius of the metal shunt $r = 4\mu m$ is used in this calculation.

The first model:

In our first model, we assume the potential of graphene at the metal edge is not fixed and changes with the gate voltage as the intrinsic graphene does. The energy difference can be expressed as:

$$\Delta E_F = \pm \hbar v_F \sqrt{\pi n_d(r)}$$

$n_d(r)$ is the charge density of the edge-contacted graphene doped by the metal at zero gate voltage, or the charge density of graphene purely due to doping.

$$|n_d(r)| = \left(\frac{\Delta E_F}{\hbar V_F}\right)^2 / \pi$$

$$n_{total} = \alpha V_g + n_d(r)$$

n_{total} is the total charge density of edge-contacted graphene doped by the metal at any gate voltage, or the charge density of graphene considering both effects of doping and gate voltage. The charge density of graphene is:

$$\sigma_g = e\mu|n_{total}| + \sigma_{min}$$

$\sigma_{min} = 4e^2/h$ is the minimal conductivity of graphene.

$$\sigma_g = e\mu \left|\alpha V_g + sign(\Delta E_F)(\frac{\Delta E_F}{\hbar V_F})^2/\pi\right| + 4e^2/h$$

where $\Delta E_F = W - W_G = \frac{1}{1+e^{2\ln\left(\frac{3(x-r)}{W_B}\right)}} * 0.33$.

In the first model, $\Delta E_F = P(x)$ as equation (4.2).

We can then put the equation of the conductivity into COMSOL for simulation.

The conductivity of graphene therefore can be expressed as a function of the distance from the metal edge and the gate voltage.

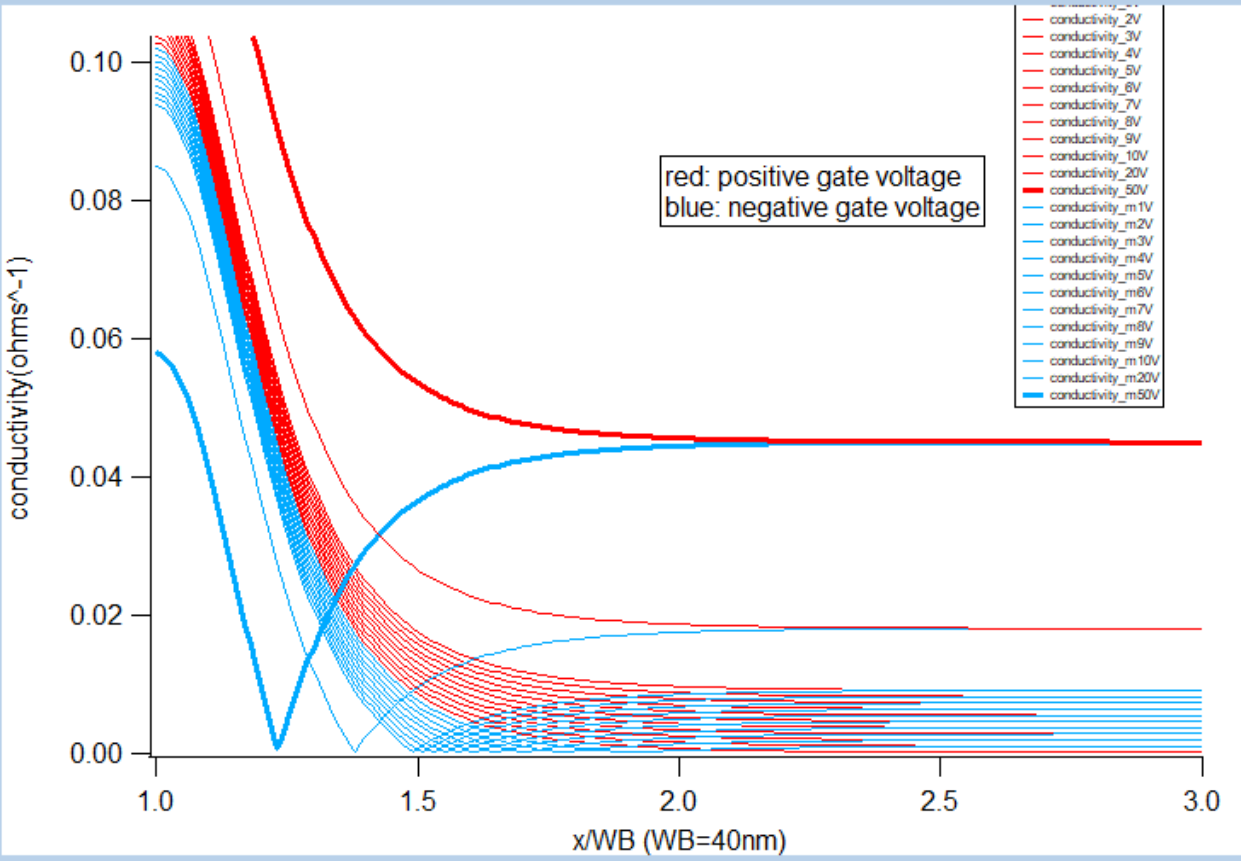

Figure 4.16 The calculated conductivity as a function of distance at different gate voltages. W_B is the characteristic width over which the potential height changes by a half. Note: The radius of the metal disk is set as $r = W_B$ in my initial calculation. The general profiles of the conductivity traces should be the same if r is changed to micron level (though the positions of the kinks would shift to the right). The more accurate calculation will be provided in the second model.

In this figure, the conductivity changes with the gate voltage applied to the device. The red traces represent the positive gate voltages, and the blue traces the negative voltages. Look at Figure 4.13, positive gate voltages induces more electrons into the system, so the graphene near the metal edge and far away from the metal forms a n-n junction, which does not limit the current, so its conductivity is not small; the negative gate voltages, however, reduces the number of electrons or induces the holes in the system, the graphene near the metal edge and far away from the metal

forms a n-p junction, of which the conductivity is small. Therefore, a kink appears in each blue trace as the result of the absolute value of a negative value inside in the equation of σ_g.

However, Song and Cho et al. use the capacitance experiments to demonstrate the work functions of graphene under several metal electrodes such as Cr, Au, Pd, etc. are pinned or fixed no matter what the gate voltage is. This gives us a different insight on the physics modeling of the metal-graphene edge contact [6].

The second model:

In this model, the potential or work function of graphene in contact with the edge of the metal is fixed or pinned, and does not change with the gate voltage since the electrons in a 3D metal do not change with the gate voltage and therefore fix the electrons of graphene at the edge of the metal too. On the other hand, the graphene far away from the metal is free-standing, so its potential should be as that of the intrinsic graphene and free to move with the gate voltage.

The large density of states in the titanium metal contact serves to pin the Fermi level in graphene so that it is highly doped (most metals yield n-type) near the contact. But out in the graphene bulk, the carrier density may still be freely varied by application of a gate voltage. Thus for some range of gate voltages, a p-n junction will arise near the contacts, serving to increase the effective contact resistance. While the use of four-terminal measurements prevents this from appearing in resistance measurements of uniform graphene devices, the effect of the metal shunt in the middle of our

devices is not removed, and the impact of pinning the Fermi level at the metal-graphene interface ought to appear in the measurement.

To verify this picture, we have modeled transport through an EMR device, assuming an edge-contacted geometry for the metallic shunt as sketched in the plot below.

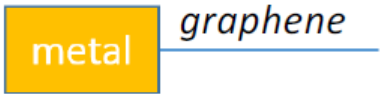

Figure 4.17 Schematic of metal and edge-contacted graphene.

In models of surface-contacted graphene, the weak metal-graphene coupling allows the graphene Fermi level to move in response to an applied gate voltage, even for graphene that is directly under the metal [2]. In our edge-contacted graphene, we assume that covalent bonding at the graphene-metal interface firmly pins the density in graphene at the interface, no matter what gate voltage may be applied. At points in the graphene away from the interface, the potential relaxes back to match the value in the bulk (e.g. set by the gate voltage) over a characteristic distance W_B.

In this model, Equation (4.2) is still correct but it does not represent the energy difference we seek any more since we need to fix the energy difference at the metal edge. Therefore, we set the energy difference as a linear function of the potential $P(x)$:

$$\Delta E_f = aP(x) + b$$

where a and b are constants.

According to the definition, at the metal edge: $x = r, P(x = r) = 0.33eV$, so $\Delta E_f = 0.33eV \times a + b = 0.33eV$, suggesting the energy of graphene is fixed at the metal edge no matter what the gate voltage is.

Far away from the metal: $x = \infty, P(x = \infty) = 0$, so $\Delta E_f = b = \Delta E_{fg}$, which is the energy of the free-standing graphene depending on the gate voltage.

From these two equations, we can get

$$\Delta E_f = (1 - \frac{\Delta E_{fg}}{0.33})P(x) + \Delta E_{fg}$$

The electrical conductivity of which is represented by our mathematical equations:

$$\sigma = e\mu|n| + \sigma_{min} \tag{4.3}$$

$$|n| = (\frac{\Delta E_f}{\hbar v_f})^2/\pi \tag{4.4}$$

$$\Delta E_f = (0.33eV - \Delta E_{fg})\frac{1}{1+e^{2\ln\left(\frac{3(x-r)}{W_B}\right)}} + \Delta E_{fg} \tag{4.5}$$

$$\Delta E_{fg} = \pm\hbar v_f\sqrt{\pi\alpha|V_g|} \tag{4.6}$$

Here, n is the charge density, $\mu = 8m^2/Vs$ is the mobility used in simulation, $\sigma_{min} = 4e^2/h$ is minimal conductivity of graphene, ΔE_f is the energy difference between the Fermi energy and the Dirac point of graphene, ΔE_{fg} refers to energy difference of graphene far away from the metal, v_f is the Fermi velocity, W_B is the characteristic width over which the potential height changes by 50%, *x* is the radius/distance away from the center of the device, *r* is the radius of the metal shunt, $\alpha = 7 \times 10^{10} cm^{-2}V^{-1}$ is a constant, and V_g is the gate voltage.

Therefore, the charge density and the conductivity can be both expressed as the distance (or radius) and gate voltage. As the gate voltage increases from negative to positive, the charge density

increases. The traces of the charge density and the conductivity are very similar to each other except those at the negative gate voltage because of the absolute sign in the conductivity equation.

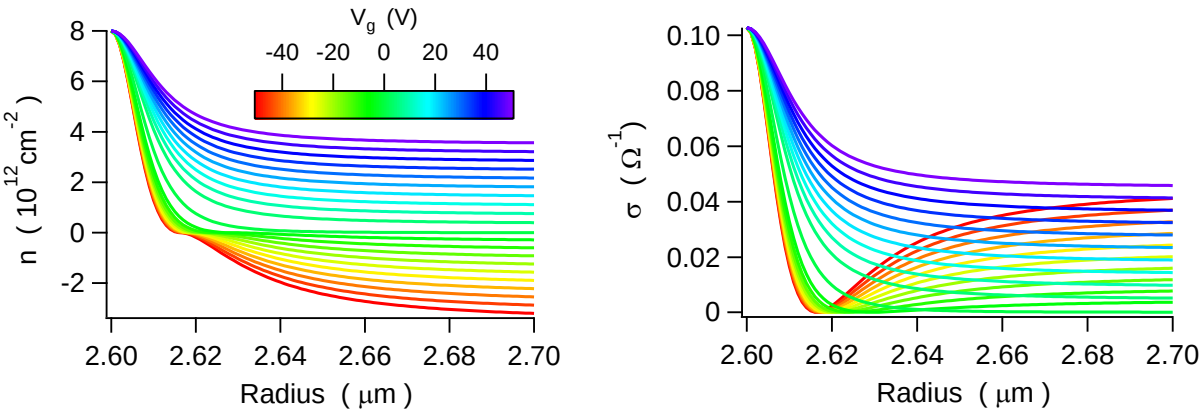

Figure 4.18 Calculated charge density and conductivity as a function of the distance at different gate voltages. The calculation is based on the characteristic width $W_B = 40\ nm$ and the radius of the metal disk $r = 2.6\ \mu m$ same as that of the real device. The charge density and the conductivity both are fixed at the metal edge, but gradually get more influnced by the gate voltage as the distance from the metal edge increases.

The two figures above show the density and conductivity profiles for a range of gate voltages, in a model device with $r_a = 2.6\ \mu m$. As expected, for gate voltages $V_g < 0$ when the graphene bulk is p-type, the conductivity reaches a minimum a short distance away from the graphene-metal interface due to the appearance of a p-n junction. So, in Figure 4.10 the device resistance overall reflects the fact that charge is less likely to traverse the metal shunt due to an effectively enhanced contact resistance, and the remaining path around the shunt is through the more resistive graphene.

4.5 Simulations in COMSOL

To see how the two models work, we perform simulation in COMSOL. From the simulation based on **the first model**, the voltage between the two voltage probes as a function of the gate voltage can be expressed as:

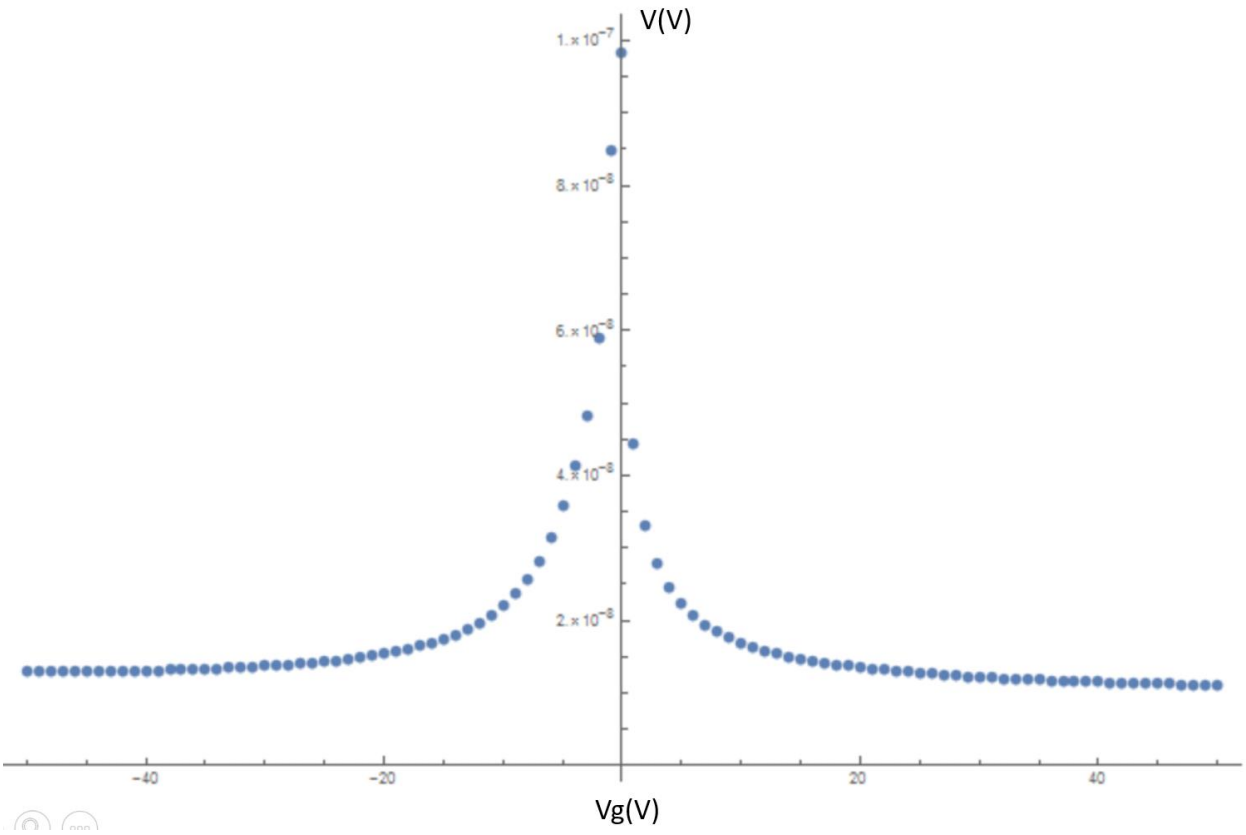

Figure 4.19 The calculated gate-voltage-dependent voltage from the first model. The radius of the metal disk is set as $r = 2.6\ \mu m$ same as the real device in the simulation. The current is 100 nA. Even though the characteristic width is set as 100 nm, the calculated asymmetry in the trace is not as strong as that of our experimental data.

Since the current is a fixed value, the asymmetry in the voltage reflects that in the resistance. Even though asymmetry appears in this calculated trace, the asymmetry is not strong as our experimental data suggests.

Since the doping from the metal shifts the Fermi level of graphene, the Dirac point of the doped graphene should not be at zero gate voltage as that of the intrinsic graphene. We adjusted the equation to shift the Dirac point to –10V which is the value I saw a lot in my previous graphene devices.

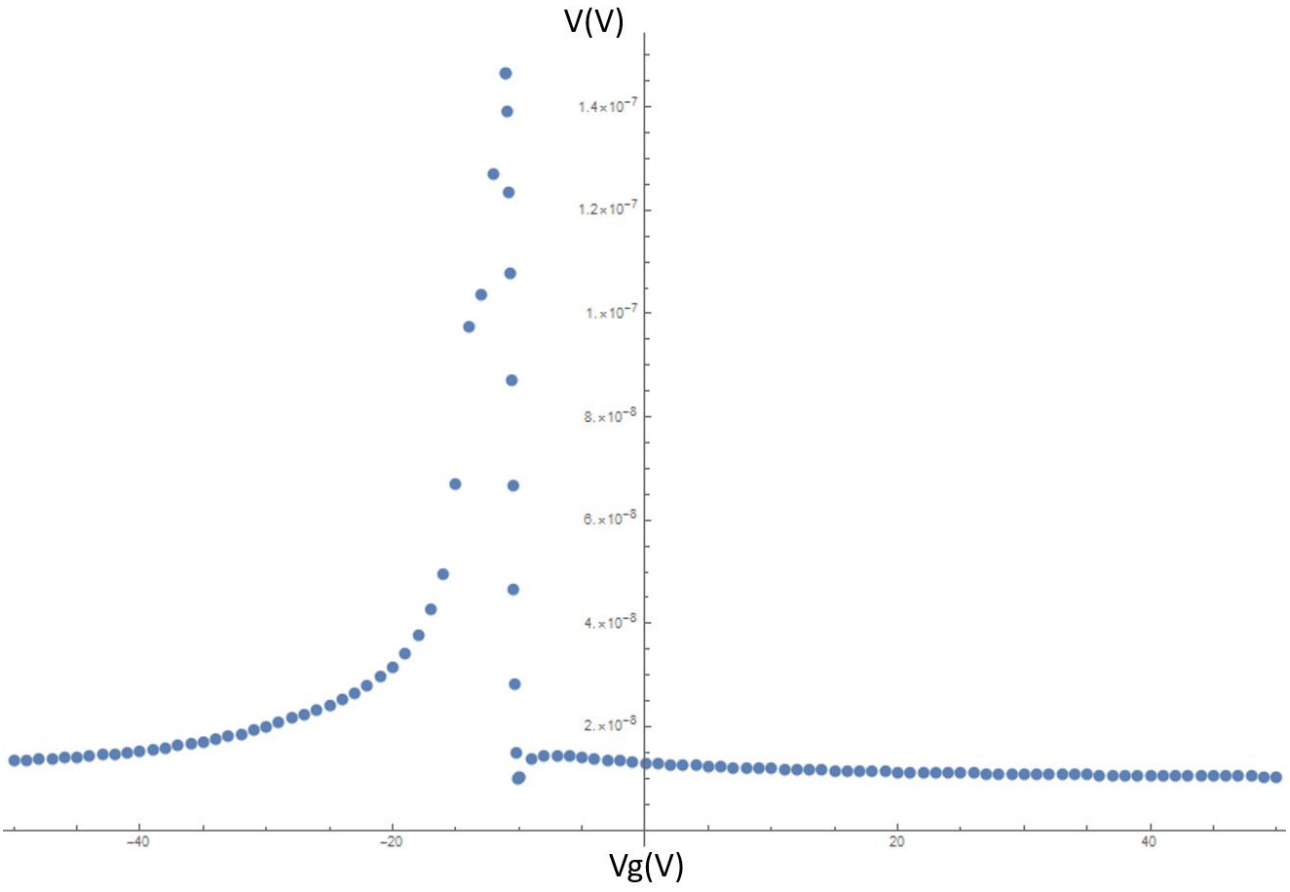

Figure 4.20 Calculated voltage as a function of the gate voltage from the first model with Dirac point adjusted.

A stronger asymmetry appears after shifting the Dirac point away from zero gate voltage. Thus, the electron-hole asymmetry in the gate-dependent voltage (or resistance) is dependent on the doping of graphene in our first model: the asymmetry is much stronger in doped graphene than in the intrinsic graphene.

However, by performing simulation based on **the second model**, we also get a stronger asymmetry in the gate-voltage-dependent voltage.

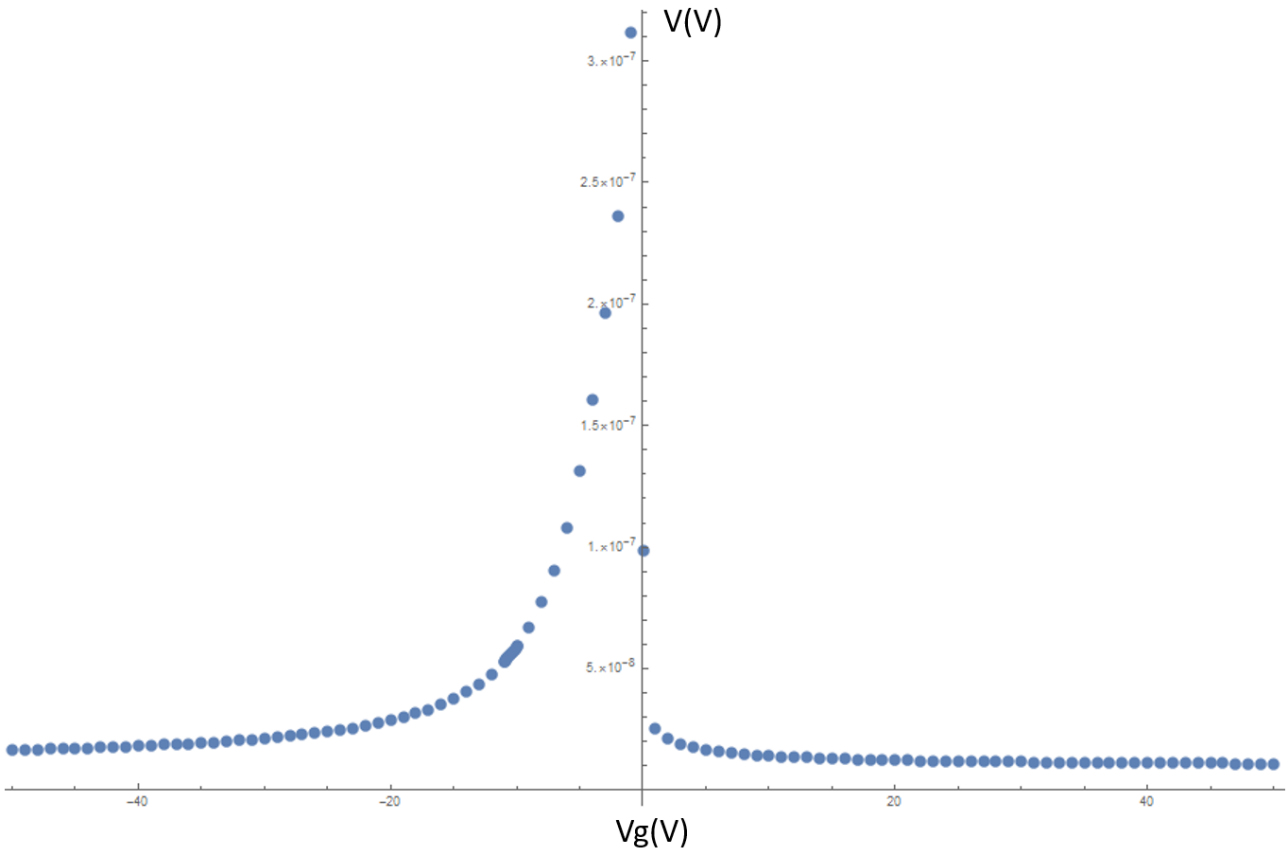

Figure 4.21 The calculated gate-voltage-dependent voltage from the second model. The current is 100 nA. The characteristic width is set as 100 nm (same as the value used in the first model to compare the result), the calculated asymmetry in the trace is comparable with that of our experimental data.

Even though we haven't adjusted the Dirac point in the equation of the second model, the trace still has a strong asymmetry which resembles our experimental data in the way that the hole branch is noticeably higher than the electron branch, and the electron side of the peak has a sharp decrease with the gate voltage. Hence, we conclude the second model makes a better physics prediction than the first model.

We use the second model to simulate the resistance as a function of the gate voltage at different characteristic widths.

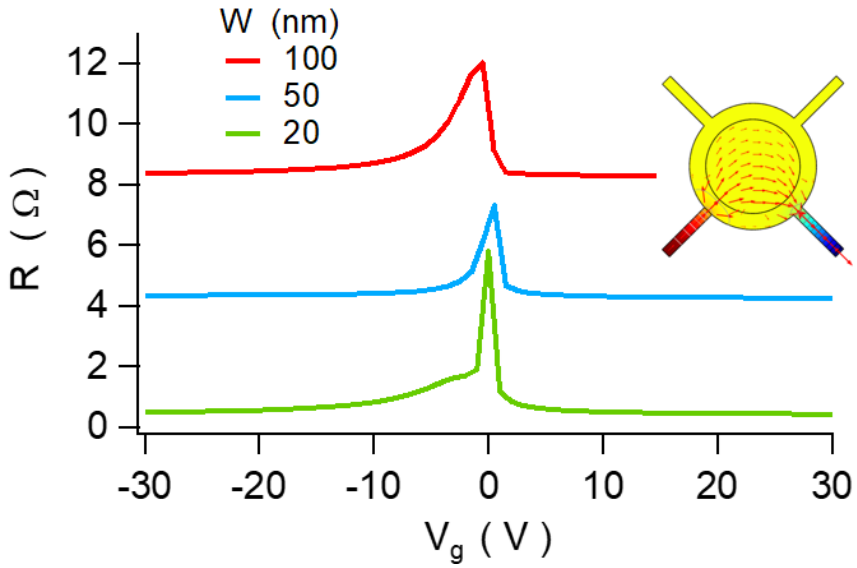

Figure 4.22 Calculated resistance as a function of the gate voltage at different characteristic widths.

Despite the simplicity of our model, a reasonable agreement with our experimental data in the Figure 4.10 is achieved with the best results for W = 100 nm: a similar asymmetry appears, over a gate voltage range not too much less than we observe. The asymmetry gets stronger as the characteristic width increases. A large characteristic width leads to a large doped area in graphene, and hence, a "longer" p-n junction.

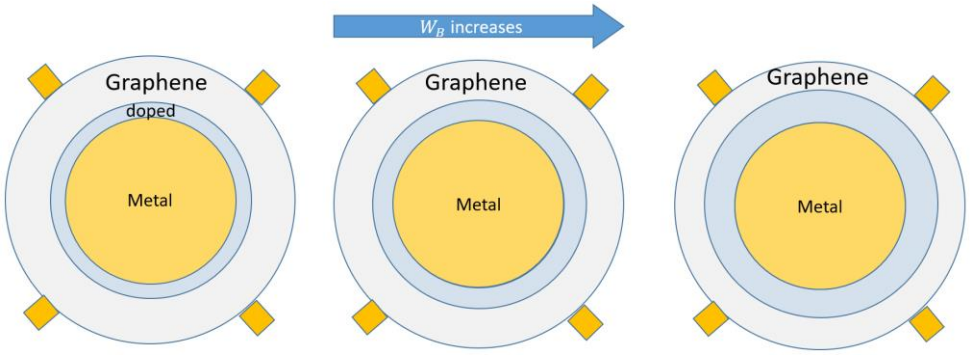

Figure 4.23 Schematic of doped area (light blue) in graphene (silver) near the metal (yellow) edge increases with the characteristic width. The whole area of graphene could be doped if graphene is heavily doped while its radius is small.

The kinks in the conductivity traces shown in Figure 4.17 represent the lowest conductivity and the highest resistivity as the major contributor to stop the current flow. The kinks move away from the metal edge as the characteristic width increases, suggesting the doped area of graphene increases and the intrinsic area decreases. If the radius of graphene is small, the kinks in the traces could go to the end of the device or even out of the range which suggests the whole area of graphene is doped.

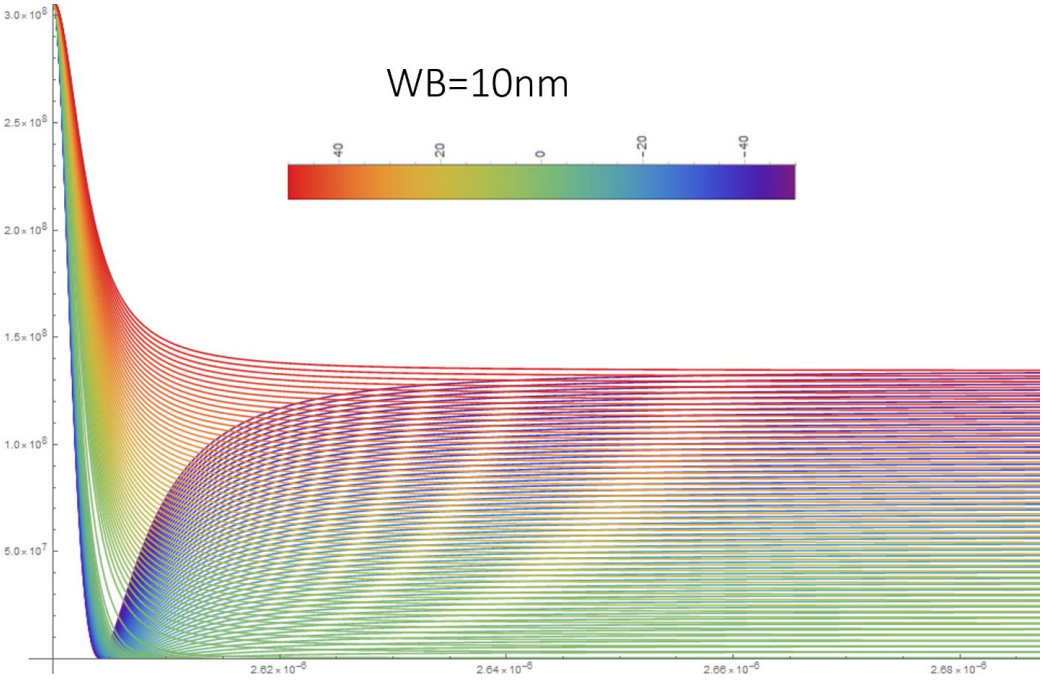

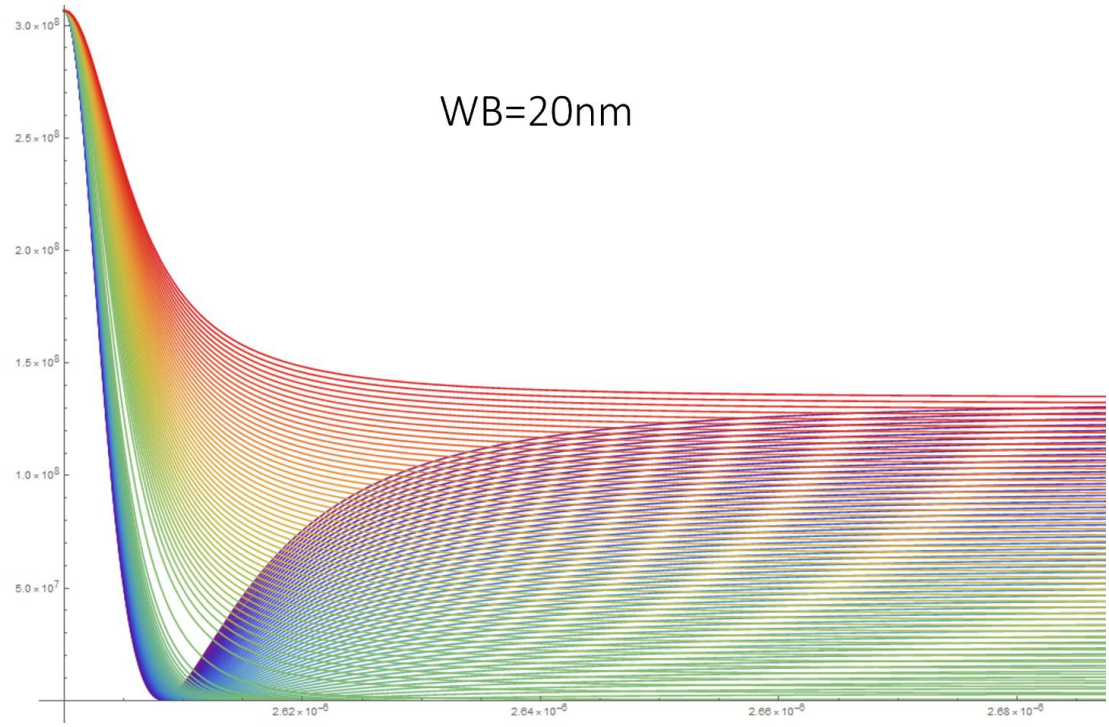

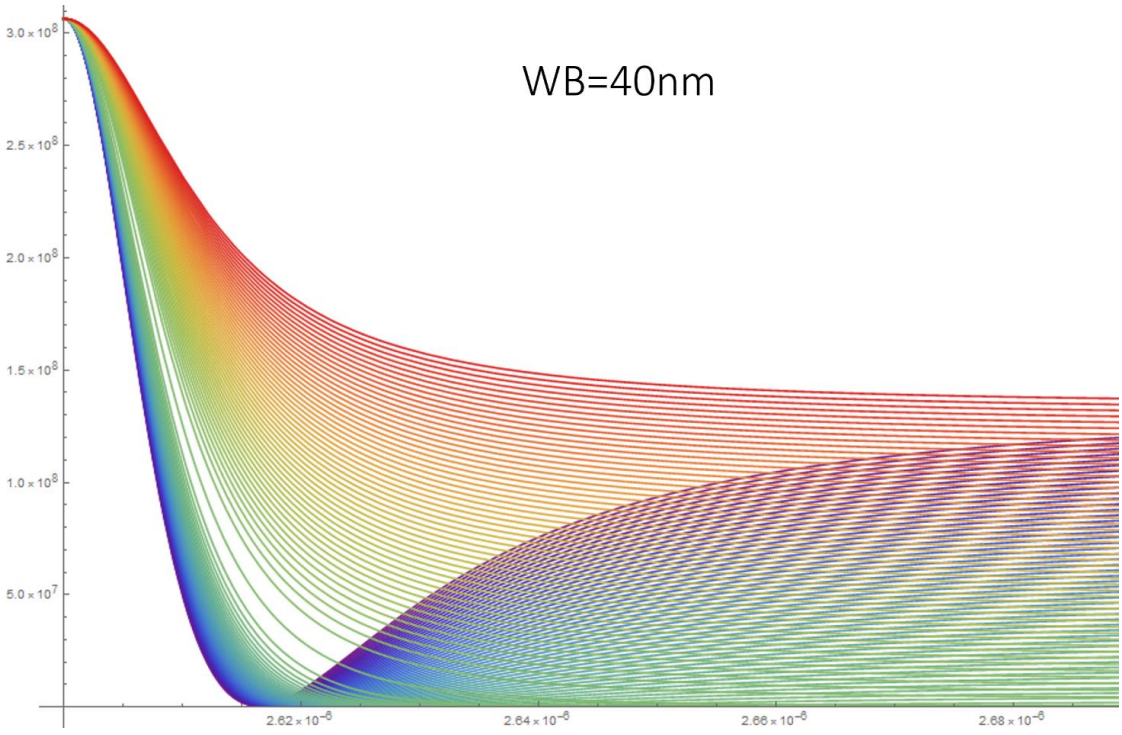

In summary, we demonstrate that an asymmetry in the gate voltage response of the zero-field resistance is traced to the presence of p-n junctions near the graphene-metal interface, and a model of edge-contacted graphene is in reasonable agreement with these observations.

Bibliography

1. P. A. Khomyakov, G. Giovannetti, P. C. Rusu, G. Brocks, J. van den Brink, and P. J. Kelly, *First-principles study of the interaction and charge transfer between graphene and metals.* Physical Review B, **79**, 195425 (2009).
2. F. Xia, V. Perebeinos, Y.M. Lin, Y. Wu, and P. Avouris, *The origins and limits of metal–graphene junction resistance*, Nature Nanotechnology, **6**, 179 (2011).
3. Q. Gao and J. Guo, *Role of chemical termination in edge contact to graphene*, APL Materials, **2**, 056105 (2014)
4. L. Wang and C. R. Dean et al., *One-Dimensional Electrical Contact to a Two-Dimensional Material, Science*, **342**, 614 (2013)
5. Y. Matsuda and W. Goddard III et al., *Contact Resistance for "End-Contacted" Metal-Graphene and Metal-Nanotube Interfaces from Quantum Mechanics*, J. Phys. Chem. C, **114**, 17845 (2010)
6. Seung Min Song, Jong Kyung Park, One Jae Sul, and Byung Jin Cho, *Determination of Work Function of Graphene under a Metal Electrode and Its Role in Contact Resistance*, Nano Lett., **12**, 3887 (2012)
7. K. S. Novoselov, A. K. Geim, S. V. Morozov, D. Jiang, Y. Zhang, S. V. Dubonos, I. V. Grigorieva, and A. A. Firsov, Science 306, 666 (2004).
8. A. L. Friedman, J. T. Robinson, F. K. Perkins, and P. M. Campbell, Applied Physics Letters 99, 022108 (2011).
9. J. Lu, H. Zhang, W. Shi, Z. Wang, Y. Zheng, T. Zhang, N. Wang, Z. Tang, and P. Sheng, Nano Letters 11, 2973 (2011).

Chapter 5:

Conclusion

5.1 Summary

This dissertation explored the phenomenon of extraordinary magnetoresistance (EMR) and p-n junction in boron nitride encapsulated monolayer graphene devices. Chapter 1 introduced the fundamentals of graphene, especially its basic physical properties relevant to the experimental results presented in Chapter 3. Chapter 2 switched to the topic of extraordinary magnetoresistance, from the theory to its first discovery in 3D, and to EMR in 2D.

With enough background provided in Chapter 1 and 2, the experimental section began in Chapter 3. We performed room-temperature electrical transport measurements on gated encapsulated monolayer graphene devices in a magnetic field up to 9T, and found the extremely large EMR values and the largest reported values of the sensitivity to magnetic fields. In many devices the zero-field resistance can be vanishingly small and even become negative due to ballistic transport. We also explored the effects of the sizes of the devices and the ratios of metallic disk to graphene on the EMR and sensitivity.

Chapter 4 first started with p-n junctions in the semiconductor and surface-contacted graphene, which is followed by a discussion of σ bonds in edge contact and π bonds in surface contact. Then it talked about my experimental data showing strong electron-hole asymmetry in gate-dependent resistance at zero field results from a resistive p-n junction in the heavily electron-doped area of

graphene near the central metallic shunt. Two models were built to explain the physics behind the asymmetry and led to calculation and simulation in COMSOL to verify the picture.

5.2 Outlook

There are still many new and interesting problems to address with EMR in edge-contacted graphene. Figure 3.2 suggests the EMR and the sensitivity show the opposite dependence on the ratio of the shunt to outer device diameters, however, both show no clear dependence on the device size possibly due to inhomogeneities in graphene or off-center metallic shunt. These phenomena could be experimentally explored more.

The experiments in this dissertation were performed at room temperature. I have also measured the field-dependent resistance at 10K, which showed Shubnikov–de Haas effect. Since the aluminum is a major component of the central metal shunt in our devices, and it is a type-I superconductor with critical temperature $T_c = 1.2$ K, what would happen to the EMR when the aluminum is superconducting and has no resistance? Will EMR become much larger at a small field $H < H_c = 0.01$T? Since the thickness of aluminum is 90 nm, the thin film aluminum could remain superconducting in a field higher than H_c because of the magnetic flux vortices. Any other interesting phenomenon could be observed at such low temperature?

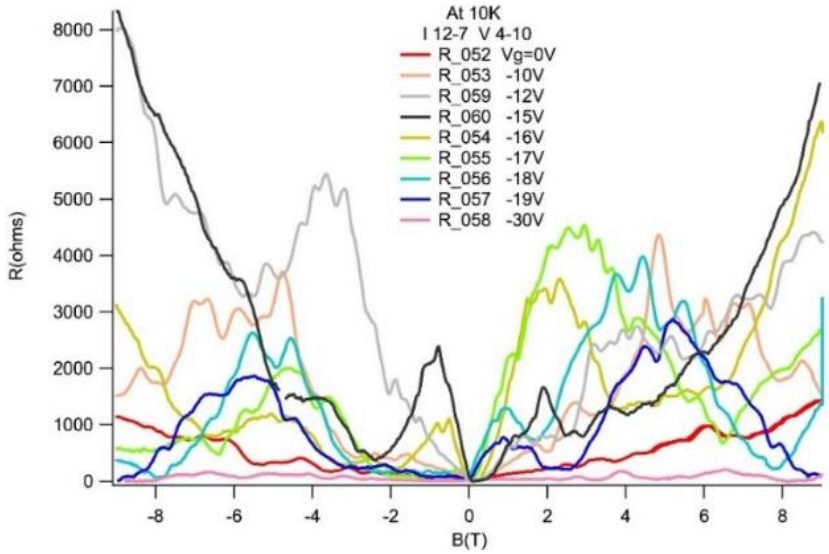

Figure 5.1 Magnetoresistances of EMR devices at 10K at different gate voltages.

Additionally, the gate-dependent resistance of my many other EMR devices show double humps in their Dirac peaks. It could also result from the inhomogeneities in graphene. Although the simulation in COMSOL that considered inhomogeneities in graphene gives a similar result, it still needs more concrete evidence.

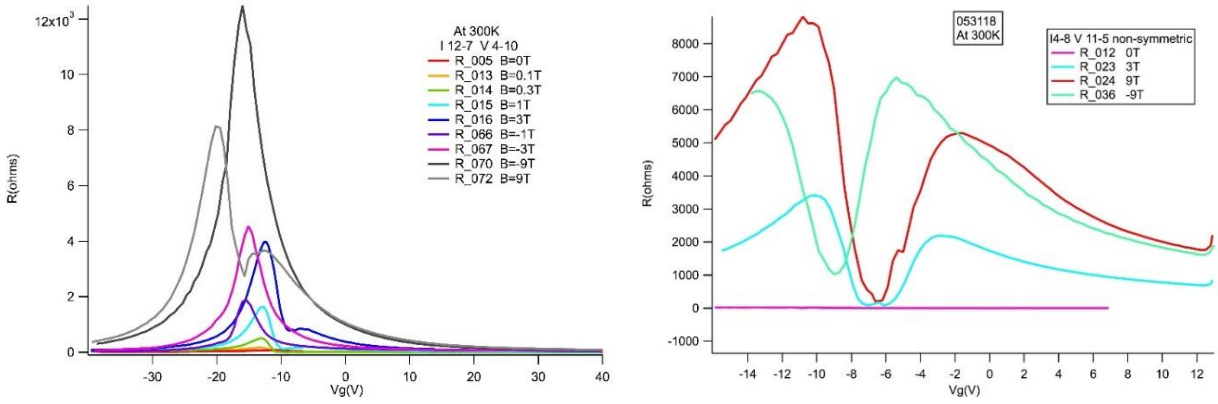

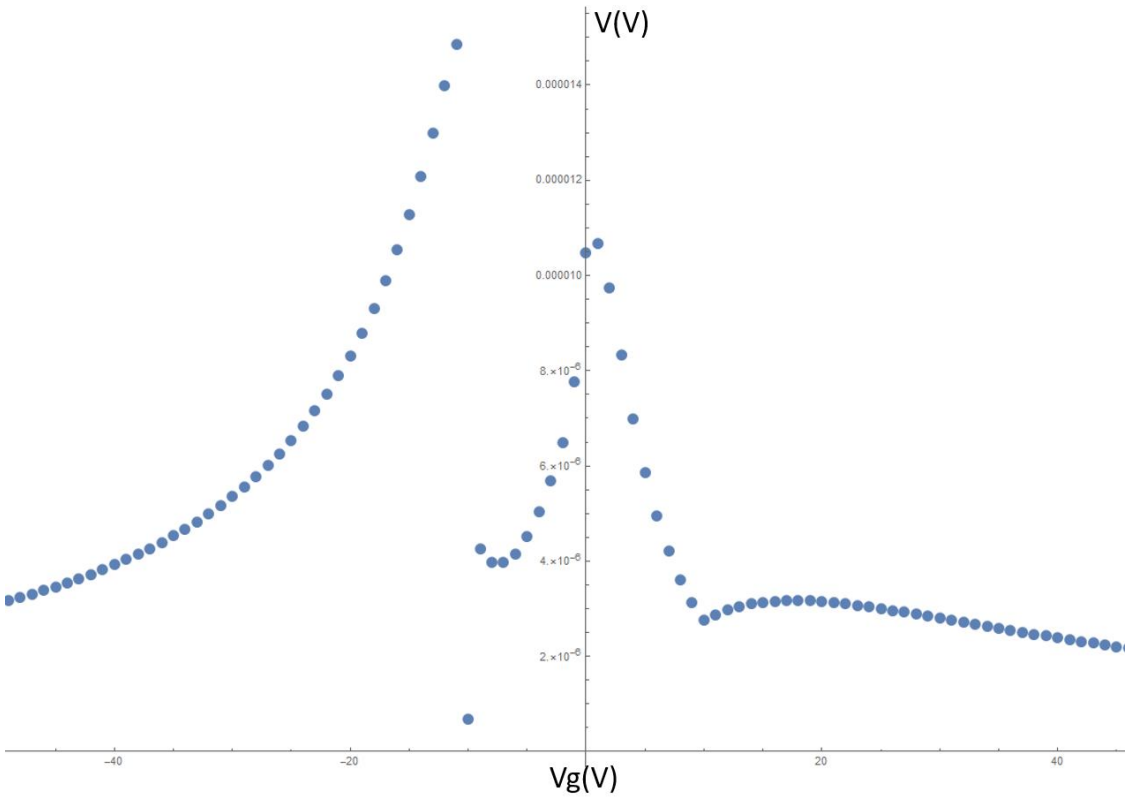

Figure 5.2 (Top) Gate-dependent resistances of EMR devices at different gate voltages. (Bottom) Simulated gate-dependent resistance in COMSOL.

Besides the EMR project, I have four unfinished projects and very much hope to finish them. In the project of spin-orbit coupling in graphene on HfO2, we hope graphene could inherit the strong spin-orbit coupling from atomic-layer-deposited HfO2 in order to make graphene a 2D topological insulator. This research has potential applications in topological insulator quantum supercomputer. One device has been measured and many beautiful plots came out from it. Even though we didn't see the weak antilocalization in the weak localization measurements possibly because the HfO2 is not clean enough to provide high mobility in graphene, 20 more devices I made are still waiting to be measured.

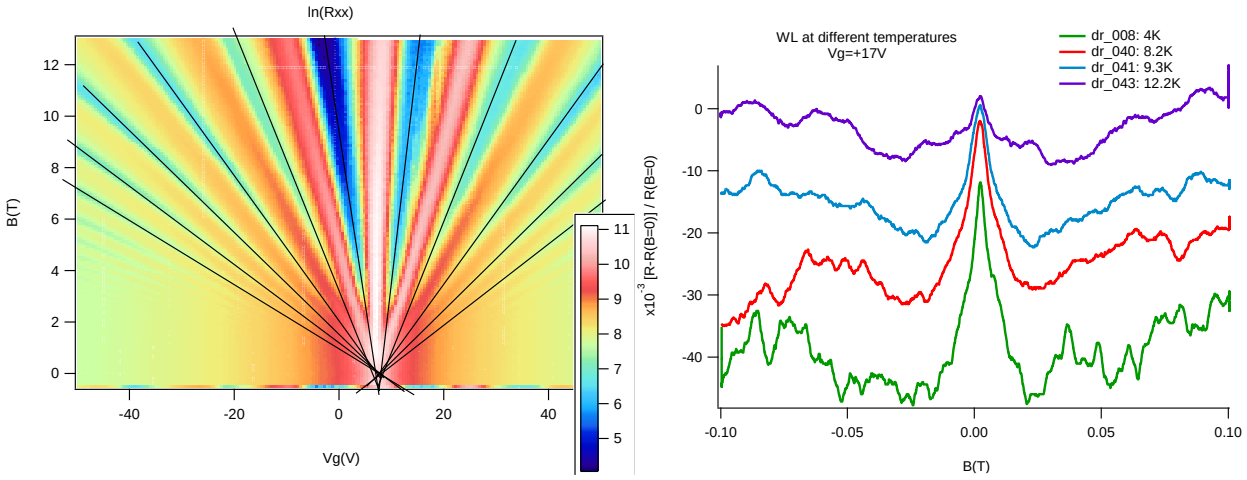

Figure 5.3 (Left) Landau fan diagram of graphene-on-HfO2 devices at 10K. The color represents the resistance. (Right) Weak localization measurements at different temperatures.

In the germanium telluride (GT) project, our goal is to experimentally confirm the ferroelectricity is largely enhanced in GT thin film, as suggested by theoretical work of Li Yang's group in our department. This project has applications in ferroelectric capacitors, ferroelectric RAM and RFID cards. One device of 30nm-thick GT was measured, and the resistance measurements vaguely suggest there are gate and magnetic field dependences. Even though germanium telluride may not be a layered material and is very hard to exfoliate to get thin films, I was still able to get some thin films that could be but have not been measured yet.

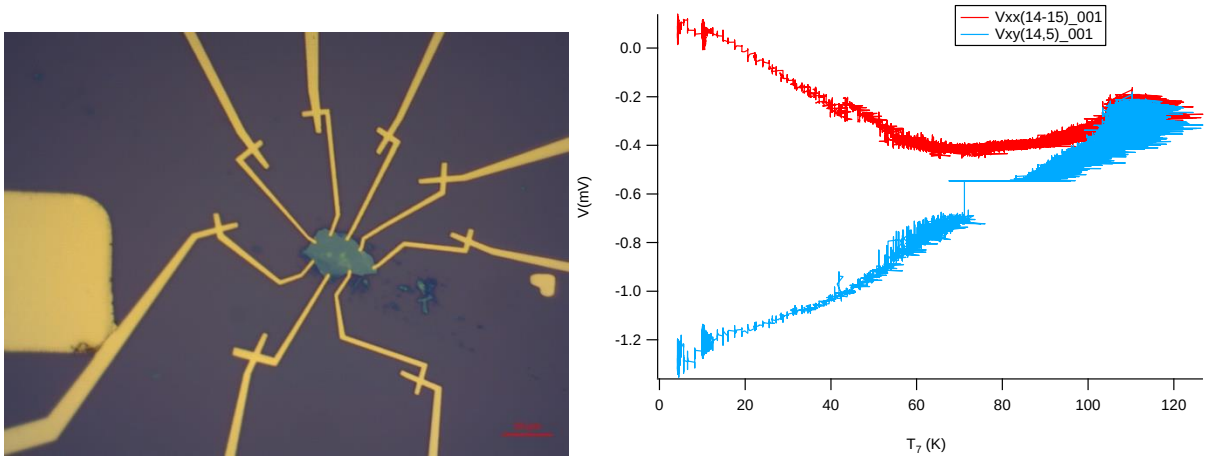

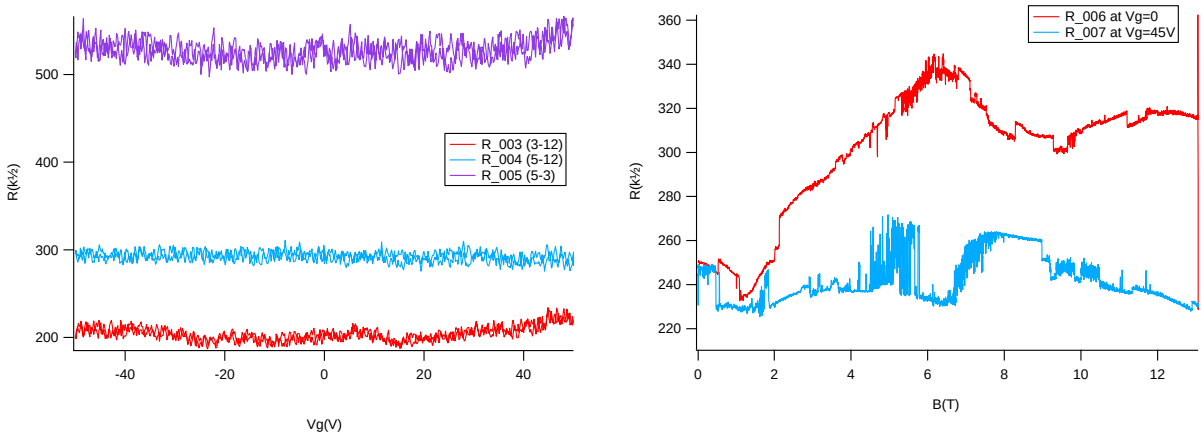

Figure 5.4 (Top Left) Microscopic image of germanium telluride thin film device. (Top Right) The voltages across the device versus the temperature (the kink in blue trace is an error in sensitivity of lock-in). (Bottom) Its resistances versus the gate voltage and magnetic field.

In the project of periodic-lattice electrical potential on encapsulated graphene, we aim to use the periodic-lattice electrical potential to artificially induce a superlattice in graphene. The holes in the top boron nitride film were drilled by focused ion beam, and two new devices have been made but never get a chance to get measured.

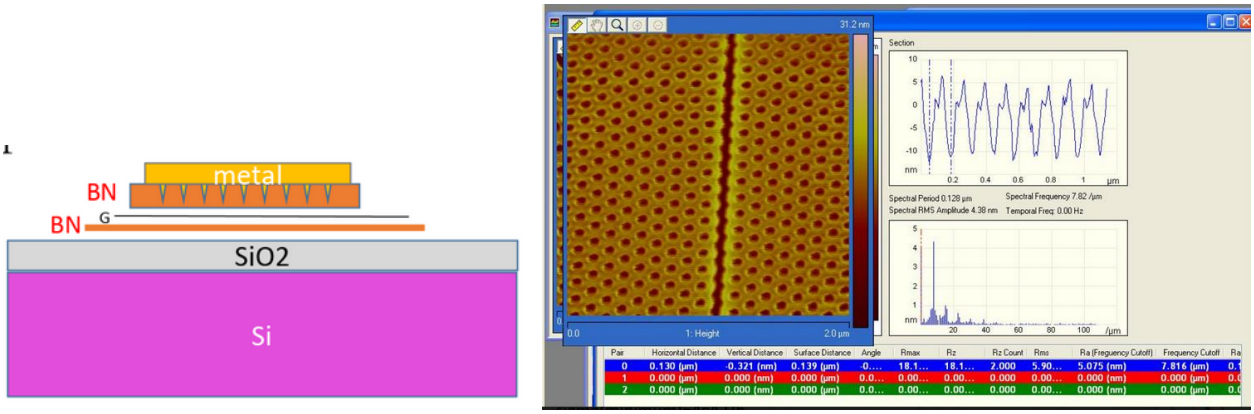

Figure 5.5 (Left) The schematic of encapsulated graphene devices with the top boron nitride films with periodic-lattice holes filled by metal. (Right) Atomic force microscope image and profile of the holes.

In the project of hydrodynamics of encapsulated graphene, we wish to use a more precise way to experimentally confirm the viscosity of electrons in graphene studied in other papers. I made several encapsulated graphene devices including monolayer graphene devices and bilayer graphene devices, and collected some data showing the negative resistance which may be a sign of viscous electrons. But I was switched to other projects and didn't get a chance to finish this project either.

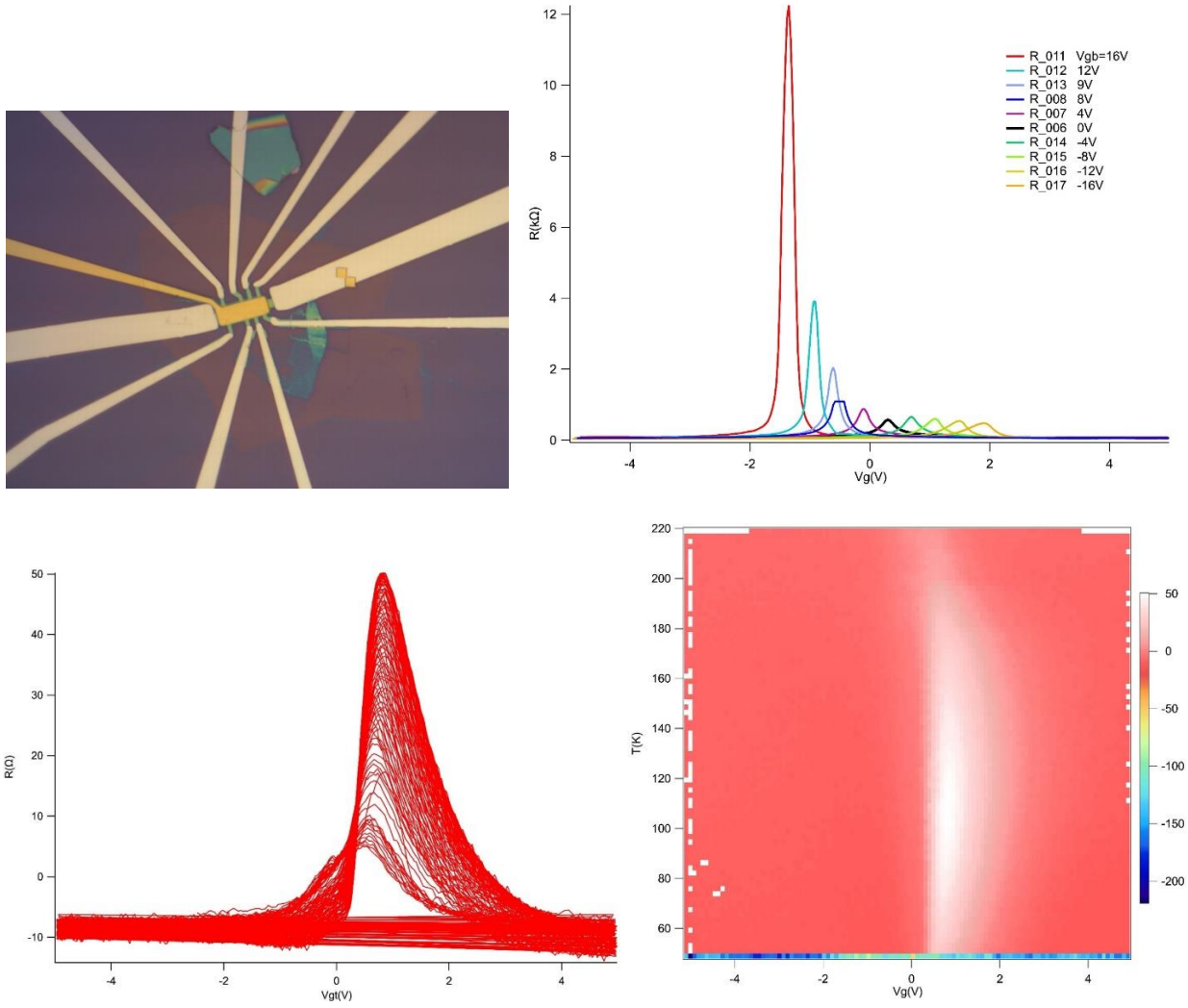

Figure 5.6 (Top left) Microscopic image of encapsulated graphene device with a top gate. (Top right) Top-gate-dependent resistance at different back gate voltages. (Bottom) Gate-dependent resistance shows negative values.

Appendix A

Instruments and Techniques

The encapsulated graphene devices widely used in transport measurements are made by boron nitride/graphene/boron nitride stacks. The boron nitride is an insulator with similar hexagonal structure and can be exfoliated for flat and clean thin films. Use the boron nitride thin films to encapsulate graphene and squeeze out the air between them can remove the hydrocarbon in the air attached to graphene, which is a major source of contamination that compromise the carrier mobility of graphene.

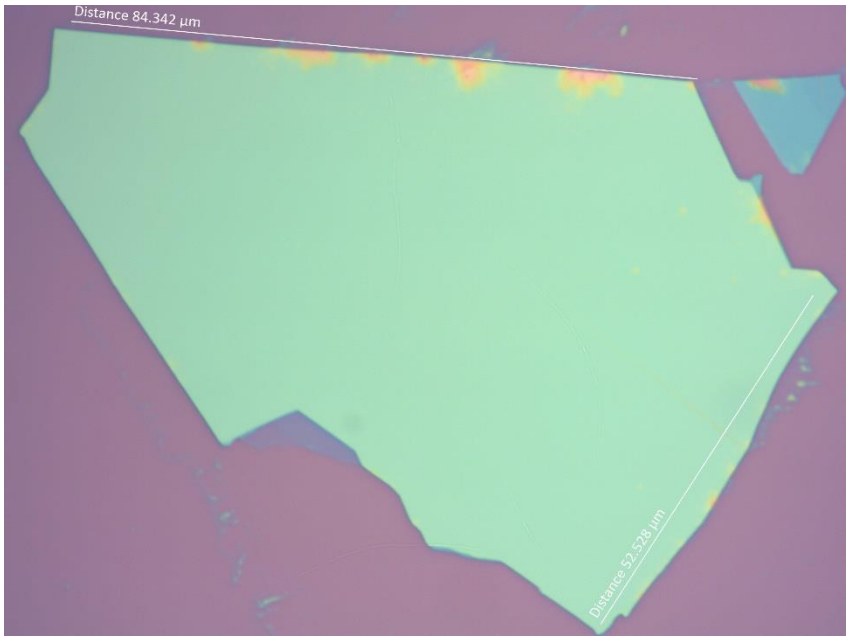

Figure A.1 Photo of boron nitride thin film (its light green color suggests its thickness is around 30nm).

The process of making encapsulated graphene device is:

(a) Make boron nitride/graphene/boron nitride stack.

(b) Spin coat the resist and use electron beam lithography to define the patterns of wires.

(c) Etch the stack to expose the edge of graphene.

(d) Deposition of metal wires to electrically connect graphene.

(e) Spin coat the resist and use electron beam lithography to define the geometry of the device. This step can also happen before step (b).

(f) Etch the stack to get the desired geometry of the device.

Then we get the desired geometry of the device connected with the metal wires.

In the figures below, I use the Hall-bar device as an example. The process for making any device is the same.

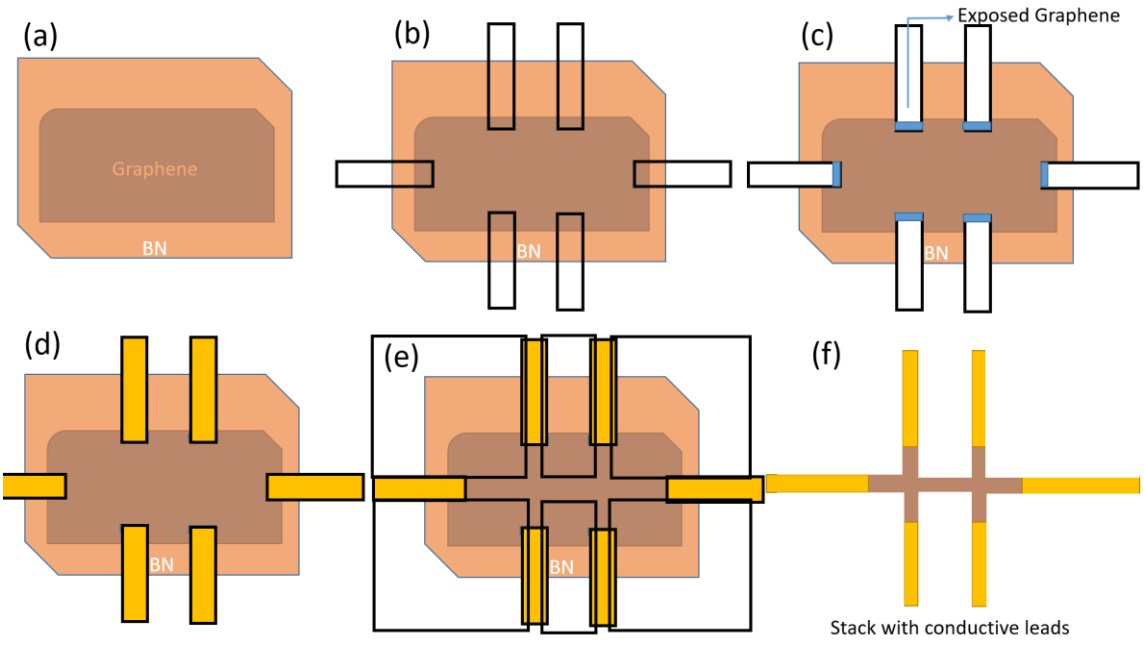

Figure A.2 Illustration of fabrication process of encapsulated graphene device.

The details of device fabrication and relevant instruments are shown in the following sections.

A.1 Probe Station and Stacking of Graphene

We use the probe station to transfer boron nitride film and graphene to make heterostructures.

Figure A.3 Photo of probe station (left) and the heater control (right).

A polypropylene carbonate (PPC) film coated soft and transparent gel-like polydimethylsiloxane (PDMS) block mounted on a glass slide is used to pick up and drop down graphene and thin boron nitride films to form van der Waals heterostructure.

The recipes for spin coating PPC:

(1) Prebake the substrate at 100 Celsius for 1 minute.

(2) Spin coat PPC.

(3) Post bake at 100 Celsius for 2 minutes.

The process of making boron nitride/graphene/boron nitride stack is shown below:

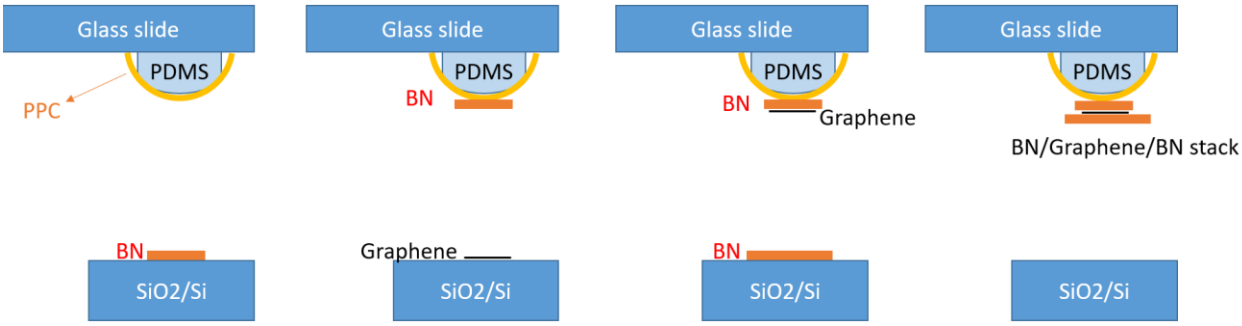

Figure A.4 Schematic of the process of stacking.

A.2 Scanning Electron Microscope and Electron beam Lithography

A scanning electron microscope (SEM) is widely used in physics research and semiconductor industry to characterize nanomaterials. SEM accelerates a beam of electrons to scan the surface of the sample and interact with atoms within, generating various signals with information about the

surface topography and composition of the sample, and producing images of the sample. The resolution of SEM can be better than 1 nanometer. In the most common SEM mode, the secondary electrons emitted by atoms excited by the electron beam are detected.

After our graphene stack is made, the stack along with the surface of the substrate are spin coated with two to three layers of transparent resist sensitive to the electron beam, called Poly(methyl methacrylate) (in short, PMMA). The resist is used for writing pattern to help etch the sample into the desired shape or deposit metal wires to electrically connect the graphene. For etching, two layers of 950PMMA are good enough to protect the sample. For depositing metal wires, two layers of 495PMMA and one layer of 950PMMA should be used. 495 and 950 represent 495,000 and 950,000 molecular weight respectively.

The recipes for spin coating PMMA are:

(1) Prebake the substrate at 150 Celsius for 1 minute.
(2) Spin coat 495PMMA and postbake at 150 Celsius for 2 minutes. And repeat this step as needed.
(3) Spin coat 950PMMA and postbake at 150 Celsius for 2 minutes.

To help us locate the micrometer-size device on the centimeter-size substrate in optical microscope, alignment marks are written/drawn in the PPMA by our Scanning Electron Microscope -- JEOL JSM-7001 LVF Field Emission SEM with the help of a software called Nabity Electron Beam Lithography (e-BL) pattern writing system (also called Nanometer Pattern Generation (NPGS) System) which controls the beam to write pattern. The process is called electron-beam lithography.

Figure A.5 Photo of scanning electron microscope.

The solubility of the resist is changed by the electron beam, so the exposed regions of the resist can be selectively removed by a developing process--immersing the chip in a cold solvent which is the composition of Isopropyl alcohol (IPA) and deionized water (the ratio is 3:1).

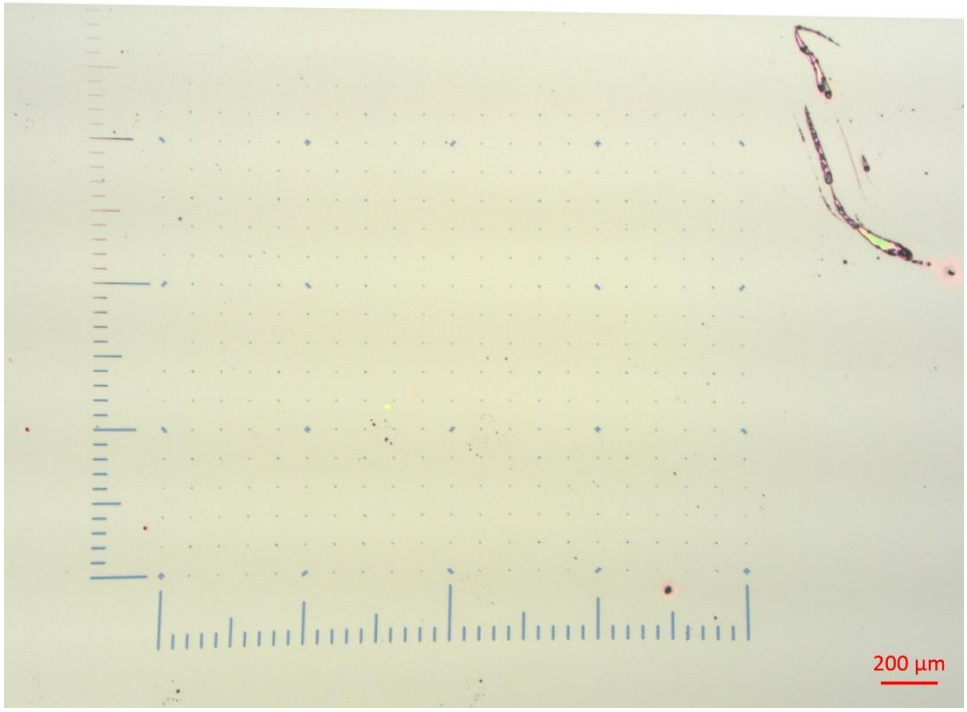

Figure A.6 Photo of alignment marks in PMMA.

One advantage of using PMMA is that it can be rewritten for several time as long as it is not over-exposed to the electron beam. We design the pattern we want for our sample in the NPGS system and then use electron beam lithography to write the pattern on the PMMA. After development, the ideal case for depositing metal wires is to get an undercut in the resist to help the lift off process later. The reason why undercut appears is because the molecular weight of 495PMMA is around a half of that of 950PMMA so it is dissolved faster in developer.

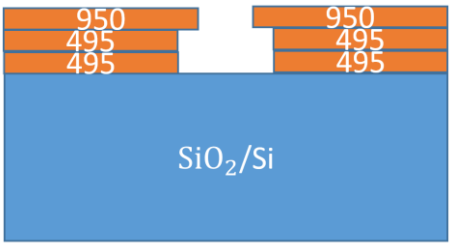

Figure A.7 Schematic of undercut in three-layer PMMA resist. The thickness of each layer of PMMA is in micrometer-size level so the thickness of the real resist should be negligible compared to the thickness of the substrate.

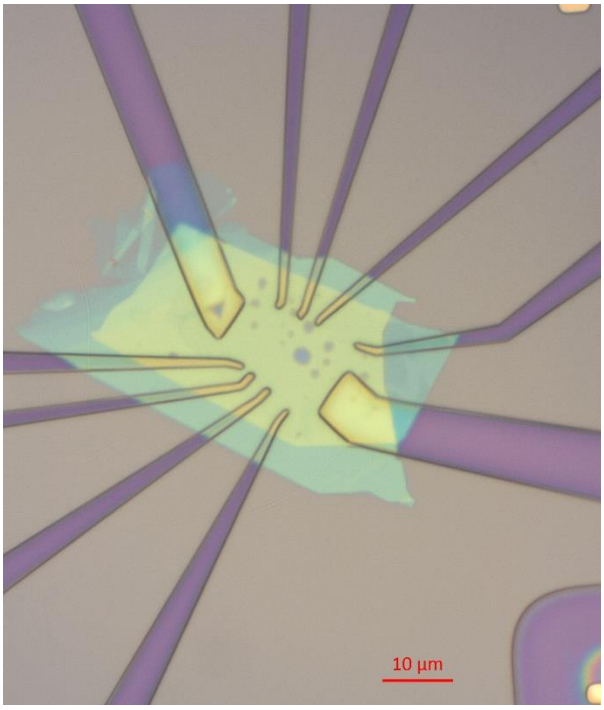

Figure A.8 Photo of EBL pattern in device. The purple color is the exposed regions of Si substrate, and represents the pattern of wires written on the PMMA for metal deposition later.

A.3 Heidelberg Laser Writer

An alternative way to make pattern is to use the Heidelberg laser writer in our cleanroom. It is very beneficial to use the laser writer for the large-scale patterns since it writes fast and saves a lot of time. Another advantage of using the laser writer is no need of alignment marks as long as the

resist is transparent to the infrared light of the camera used to locate the sample. The experience tells us that we can see the sample underneath if the resist surface is smooth.

Figure A.9 Photo of Heidelberg laser writer system.

The system we use is Heidelberg DWL66+ Laser writer. It concentrates the ultraviolet light with a wavelength of 375 nm into a laser beam to pattern a single photoresist layer. It can be considered as an advanced version of UV mask aligner that performs photolithography without using photomask, instead it controls the location of UV beam to write patterns. The laser writer has two laser heads: 10 millimeter head and 2 millimeter head. The laser spot size(diameter) of the 10 millimeter head is 2 micrometer, and that of the 2 millimeter head is 600 nanometer. So the

smallest feature size that can be written by the 2 millimeter head is around 600 nm. The resist thickness can range from 100 nm to 100 µm.

The resist we use in the laser writer is KL IR Lift-Off 15 Dual-Tone Photoresist. It can be used both as a positive resist and a negative resist. The negative resist mode is used for lift-off process.

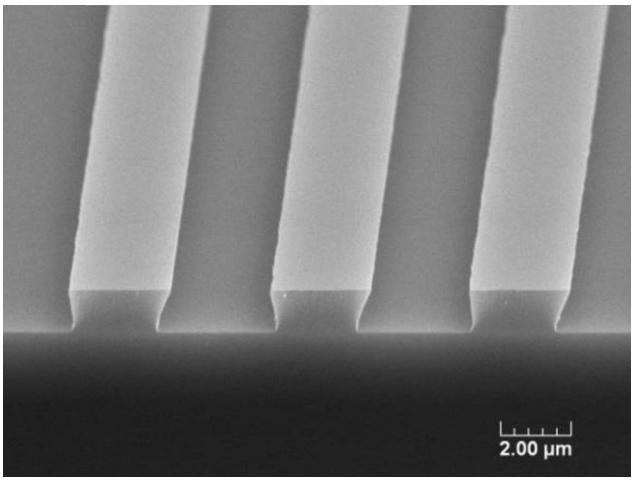

Figure A.10 Scanning electron microscope image of the KL IR resist with undercuts [1].

KL IR patterning for Lift-off Process is:

(1) Spin coat at 5000 rpm (and get the thickness of 1.18 micrometer).

(2) Negative soft bake at 105 Celsius for 90 s.

(3) Laser writer exposure by 10 mm head: Focus 0, Power 70 mW, Filter 50%, Intensity 80%, Exposure runs two times (optimized). Results: 2 um feature comes out to be close to 2 um.

Or

Laser writer exposure by 2 mm head: Focus 0, Power 47mW, Filter 12.5%, Intensity 100% (optimized). Results: 2 um feature comes out to be 1.68 um.

(4) Post Bake (reversal bake) at 130 Celsius for 90 s -- Very critical step.

(5) Flood exposure by mask aligner in power of $150\ \mathrm{mJ}/cm^2$.

(6) Develop for ~45 seconds in MIF-319. Watch the pattern carefully to prevent over development.

Note: there is a small difference in exposure parameters for writing on resist directly on silicon substrate and on boron nitride film. The light reflection rates are different on the substrate and on the boron nitride film, so the secondary exposure on the surrounding resist is different. Therefore, it is a good idea to do test run in small scale first to optimize the exposure parameters before the actual exposure, otherwise you may get a pattern wider than you expect.

One disadvantage of using laser writer is that it cannot draw clear patterns smaller than 1.68 um. So we still have to use electron beam lithography when we want to have smaller patterns. Another disadvantage of using this system is the drifting of the laser beam: we can see there is a misalignment of a few micrometers between the pattern and the sample after ten-minute beam exposure. The drifting is always happening independent of exposure, so the shorter time the process takes, the smaller drifting you get.

When the patterns of the wires are drawn, the next step is deposition of metal.

A.4 Electron Beam Evaporator

The electron beam evaporator accelerates the electrons to bombard the metal source in a high vacuum, and the heated metal atoms are transformed from solid state into gaseous phase and coated on the substrate along with the chamber.

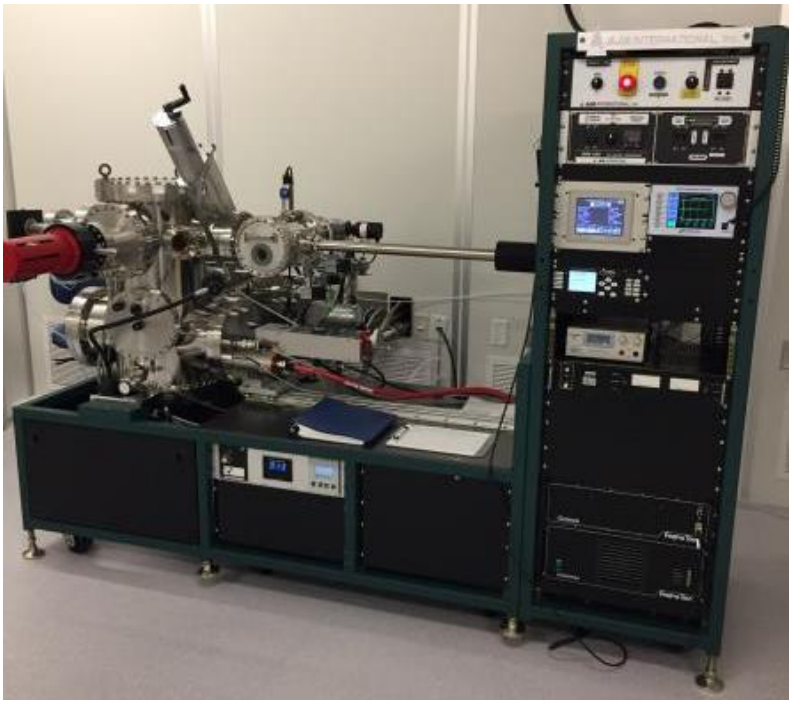

Figure A.11 Photo of electron beam evaporator system.

We use the AJA International e-beam instrument to deposit titanium (as an adhesion layer) and aluminum in a very high vacuum ~$1e^{-9}$ torr.

The parameters we use in electron beam evaporation is:

Base pressure: 1.2×10^{-9} torr. Spin the sample holder for uniform coating.

Titanium: 70 mA current, 1.4 Å/s evaporation rate, 4 nm thickness.

Aluminum: 190 mA, 2.4 Å/s, 80 nm.

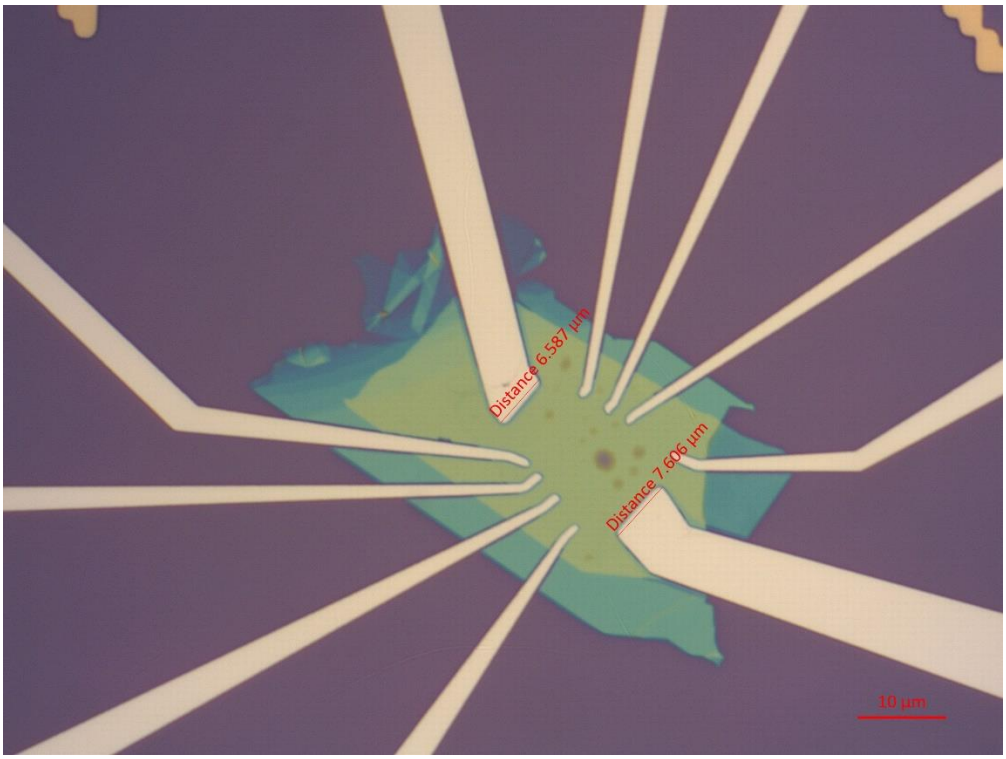

Figure A.12 Photo of device with Al wires (white) made by electron beam evaporation.

Note: Every time the evaporation chamber gets open for repair, moisture and air get in it. We need to wait for more than a week to pump down to low enough pressure (smaller than 2×10^{-8} torr) before reuse, otherwise the lift-off could be very bad (you can see a lot of wrinkles appear on the metal film after evaporation).

A.5 Thermal Evaporator

The thermal evaporation is also a way for metal deposition. It heats up the metal source to evaporate and coat on the substrate. However, the edge-contact resistance of the device resulted from thermal evaporation is huge, in megaohms, suggesting bad contacts. Our guess is the pressure in the thermal evaporator cannot get low enough (the lowest pressure is $\sim 10^{-6}$ millibar), so the metal atoms to form contact get oxidized very quickly.

We only use thermal evaporator for non-edge-contact evaporation.

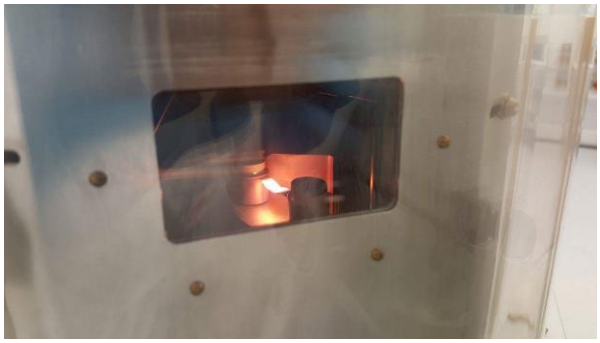

Figure A.13 Photos of Edwards auto 306 thermal evaporator. The lower photo is taken when the evaporator is heating up and evaporating the gold source.

The parameters we use in thermal evaporation is:

Base pressure: 1.9×10^{-6} millibar.

Cr (adhesion layer): 3.8 A current, 1.5 Å/s evaporation rate, 4.5 nm thickness.

Au: 4 A, 4.7 Å/s, 90 nm.

After evaporation, we put the substrate into acetone at 50 Celsius for more than half an hour for lift-off. If the undercut of the resist is in good shape, then lift-off process should not be hard. According to my experience, the lift-off process after thermal evaporation is much easier than that after electron beam evaporation.

And then, we perform spin coating process and the electron beam lithography process again to write pattern for reactive ion etching.

A.6 Reactive Ion Etching

The wet etching could bring impurities to contaminate graphene since it uses liquid chemicals to remove materials from a wafer, the dry etching is used to etch high-mobility graphene devices. We use reactive ion etching, which generates plasma and drives high-energy ions to hit wafer surface and chemically react with it. We use Oxford Plasma Lab 100 Inductively Coupled Plasma (ICP).

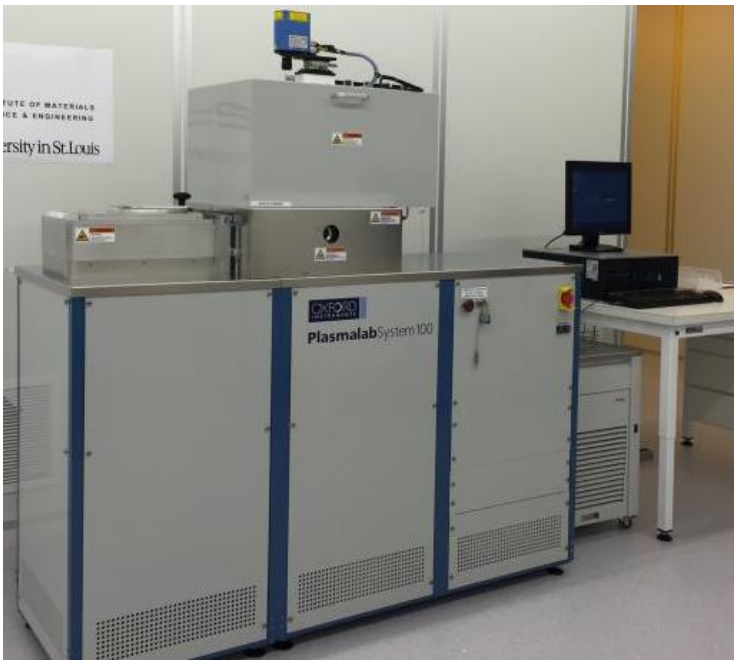

Figure A.14 Photo of reactive ion etching system.

The recipes I use for etching boron nitride/graphene/boron nitride stack is:

SF_6 50 sccm and O_2 5 sccm. RF power 100 W and ICP power 100 W. Pressure 50 mtorr. Etch 7 seconds for 60 nm-thick device.

Figure A.15 Schematic process of reactive ion etching and evaporation.

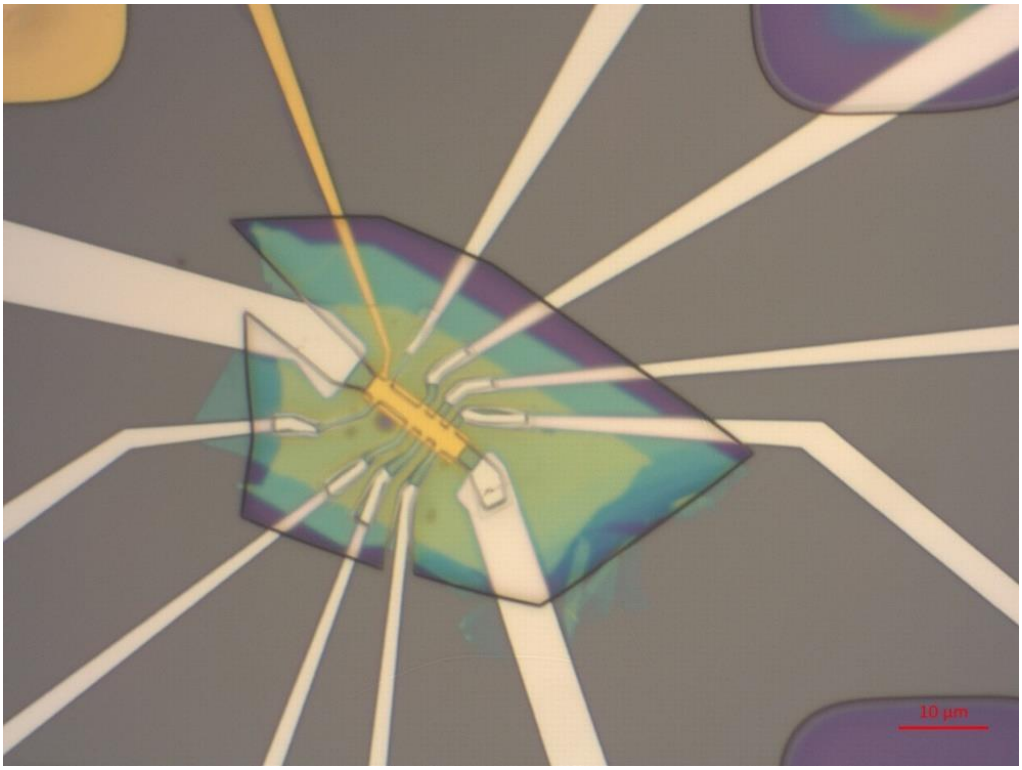

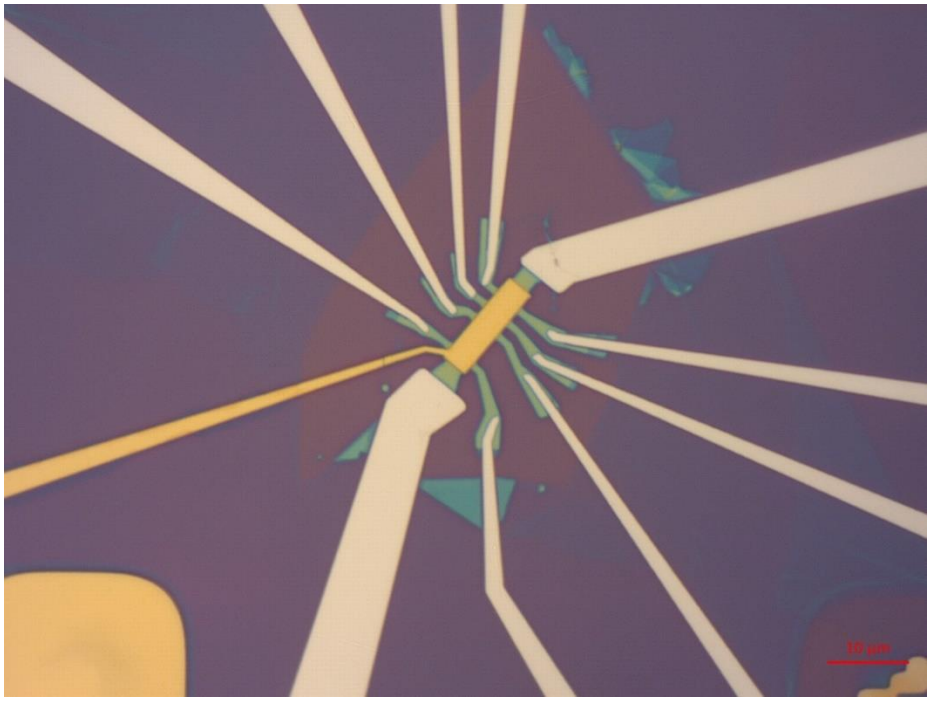

Figure A.16 Pictures of device before and after etching. The Au top gate (yellow) was made by the thermal evaporation.

A.7 Physical Property Measurement System

The measurement system we use is the Physical Property Measurement System (PPMS), which consists of a 9-tesla superconducting magnet in a helium dewar with sample temperature range from 2K to 400K. It is like a small version of dilution refrigerator, and it has advantages such as easier operation, faster cool down rate and faster ramp rate of the magnet compared to the dilution refrigerator. The downsides of using PPMS are the minimal ramp rate of its magnet is still too fast

to get high-resolution 3D plots of R vs Vg and B when we simultaneously sweep the gate voltage and the magnet, so we have to sweep the magnet back and forth several times to compensate it.

Figure A.17 Picture of PPMS and measurement instruments.

Bibliography

1. KL IR resist image reproduced from website: http://micromaterialstech.com/wp-content/uploads/2015/06/Image-Reversible-Resist-LiftOff-ver2.pdf

Appendix B

Measurement Circuit

Before the transport measurements, we measure the contact resistances (the resistances of contacts between the metal and graphene) first to make sure enough contacts working for our measurements.

The circuit diagram for contact resistance measurements is shown below:

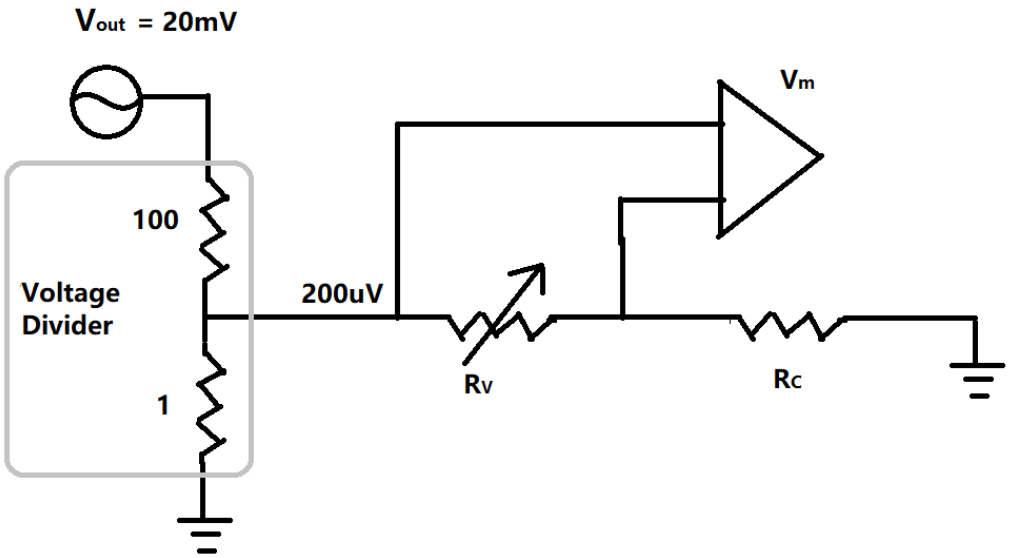

Figure B.1 Circuit diagram for contact resistance measurement.

Voltage divider 100:1 is used to transform the output voltage 20 mV into 0.2 mV or 200 μV.

R_V is variable resistor.

R_C is contact resistance of graphene device.

V_m is the measured voltage.

Only one contact of the graphene device is connected in series with the variable resistor and all the rest are grounded so that only one contact resistance is measured each time. The current is same in the same metal wire, so the current runs through R_C and R_V is the same:

$$\frac{200\mu V - V_m}{R_C} = I = \frac{V_m}{R_V}$$

Then the contact resistance can be expressed as the measured voltage and resistance used in the variable resistor as

$$R_C = \frac{200\mu V - V_m}{V_m} R_V$$

When the variable resistor is adjusted so that the measured voltage is a half of the voltage provided ($200\ \mu V$ in this case), the voltages across the variable resistor and the contact should be the same, then the contact resistance is equal to the resistance in the variable resistor. This is how we found the contact resistance.

After the contact resistance measurements, we perform the four-wire transport measurements. We use EMR measurement as an example:

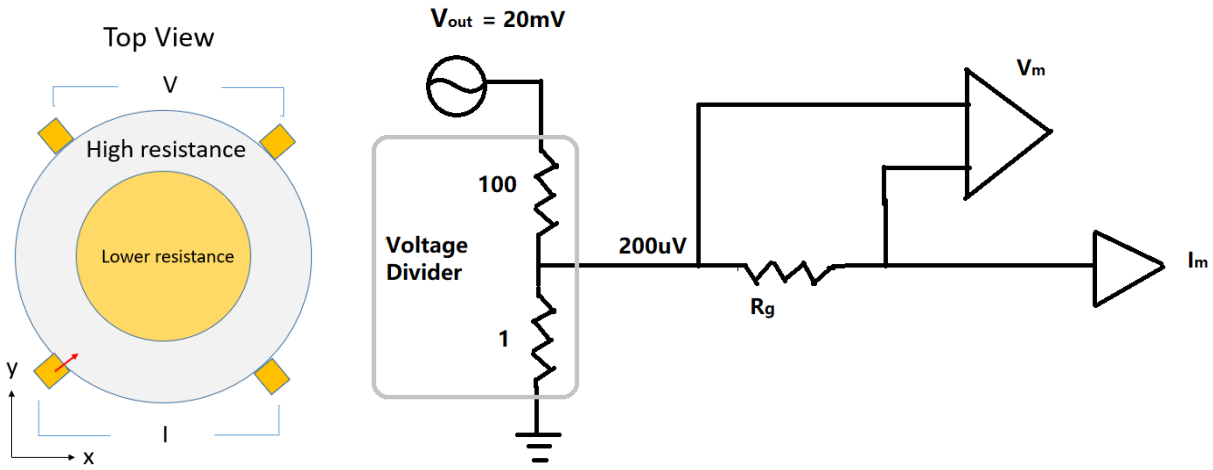

Figure B.2 Circuit diagram for 4-wire resistance measurement

R_g is the measured resistance of graphene.

I_m is the measured current.

The circuit diagram is similar to that of contact resistance measurement. In the 4-wire resistance measurement there is no variable resistor, and we directly measure the voltage across two contacts of the graphene device and the current running through the device. So the resistance of the device is $R_g = V_m/I_m$.

Appendix C

Contact Resistance

From my experience, the contacts with resistance smaller than 10K ohms are good for measurements and those with resistance larger than 10K ohms could have large noise in signal. And the larger the contact resistance is, the larger the noise is, and the less usable the contact is.

I have made around eighty graphene devices, many of them have only three contacts with small contact resistance and others with huge contact resistance (some of them have mega ohms). I have tried many ways to solve this problem, but none of them seem to work until I made contact interface between the metal and the graphene wider.

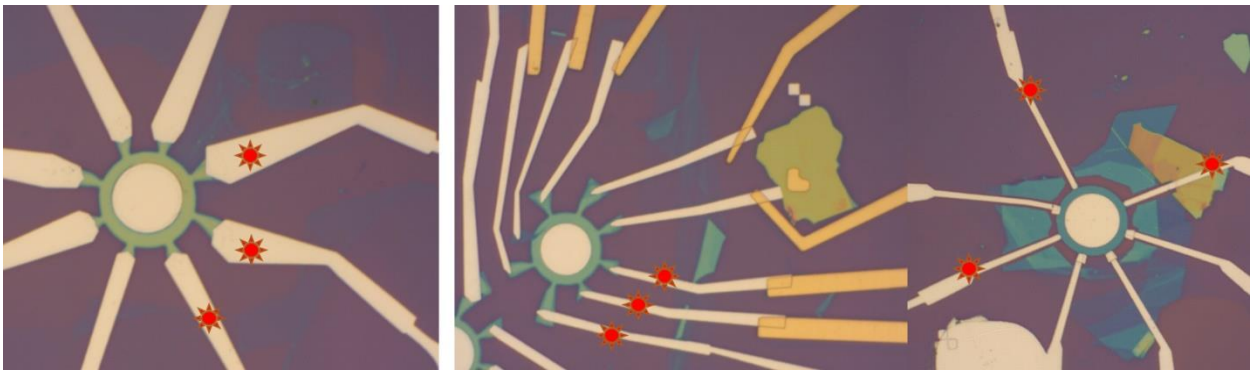

Figure C.1 Photos of devices before I made contact area larger. Each red mark suggests one working contact while the rest are bad contacts.

After I made those contact areas larger, the number of working contacts get statistically improved: most contacts of each device work. The reason is simple: the contact interface between 2D graphene and 3D metal is only a 1D line. So the contact resistance is inversely proportional to the contact width. The wider the contact width is, the smaller the contact resistance is.

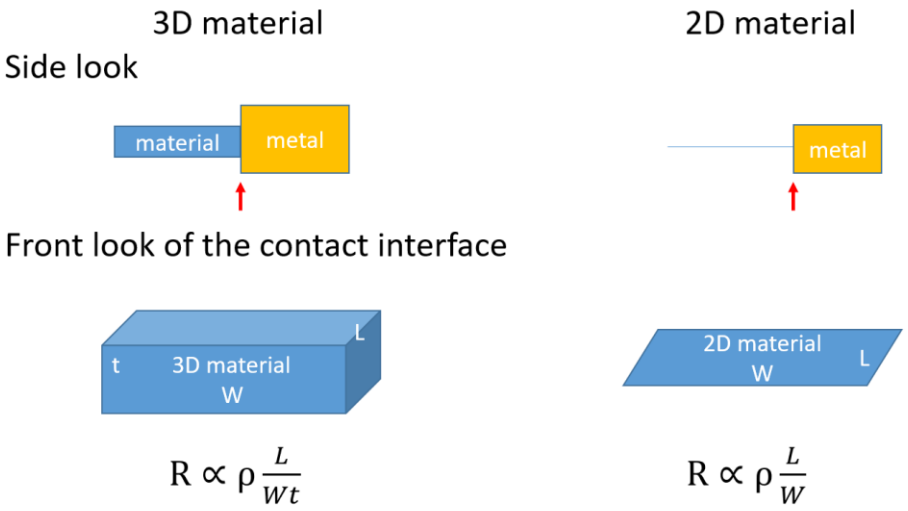

Figure C.2 Schematics of the 3D and 2D contact interfaces.

Below is an example of comparison of wide contact interfaces and narrow contact interfaces, the Al wires and the graphene contacts were intentionally made wider in the left figure to make the contact interfaces wider:

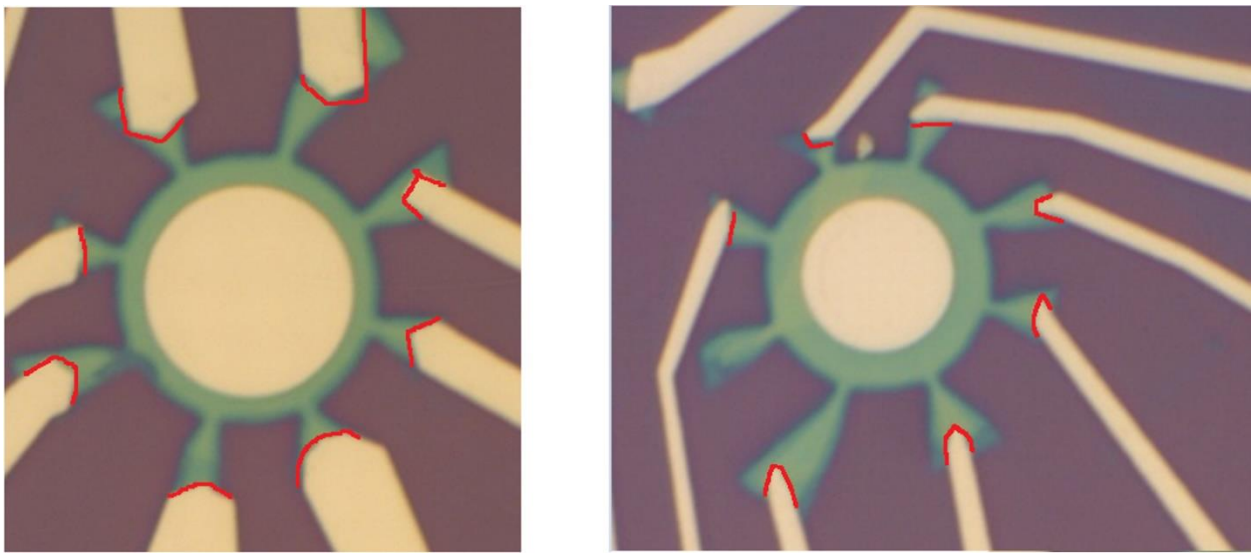

Figure C.3 Schematics of the wide (left) and narrow (right) contact interfaces. The interfaces are shown in red color.

Figure C.4 Photos of devices after I made contact area larger.

Another way to make contact resistance smaller is to use the Heidelberg Laser Writer to write the wiring patterns before evaporation, and most of the contacts work without widening the contact interfaces. It is likely that the undercut of the single-layer KL IR resist is not as wide as that of the three-layer PMMA resist.

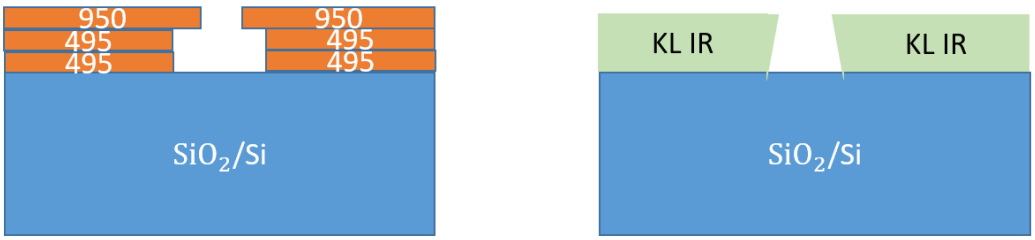

Figure C.5 Schematics of the undercuts of PMMA resist and the KL IR resist.

The wider the undercut is, the larger contact area between graphene and the metal get etched away, and then the deposited metal makes no connection with the graphene. This could be the reason why the same designed wiring pattern results in different contact resistances for the KL IR and PMMA. We can clearly see gaps between graphene and metal wires in the figure below:

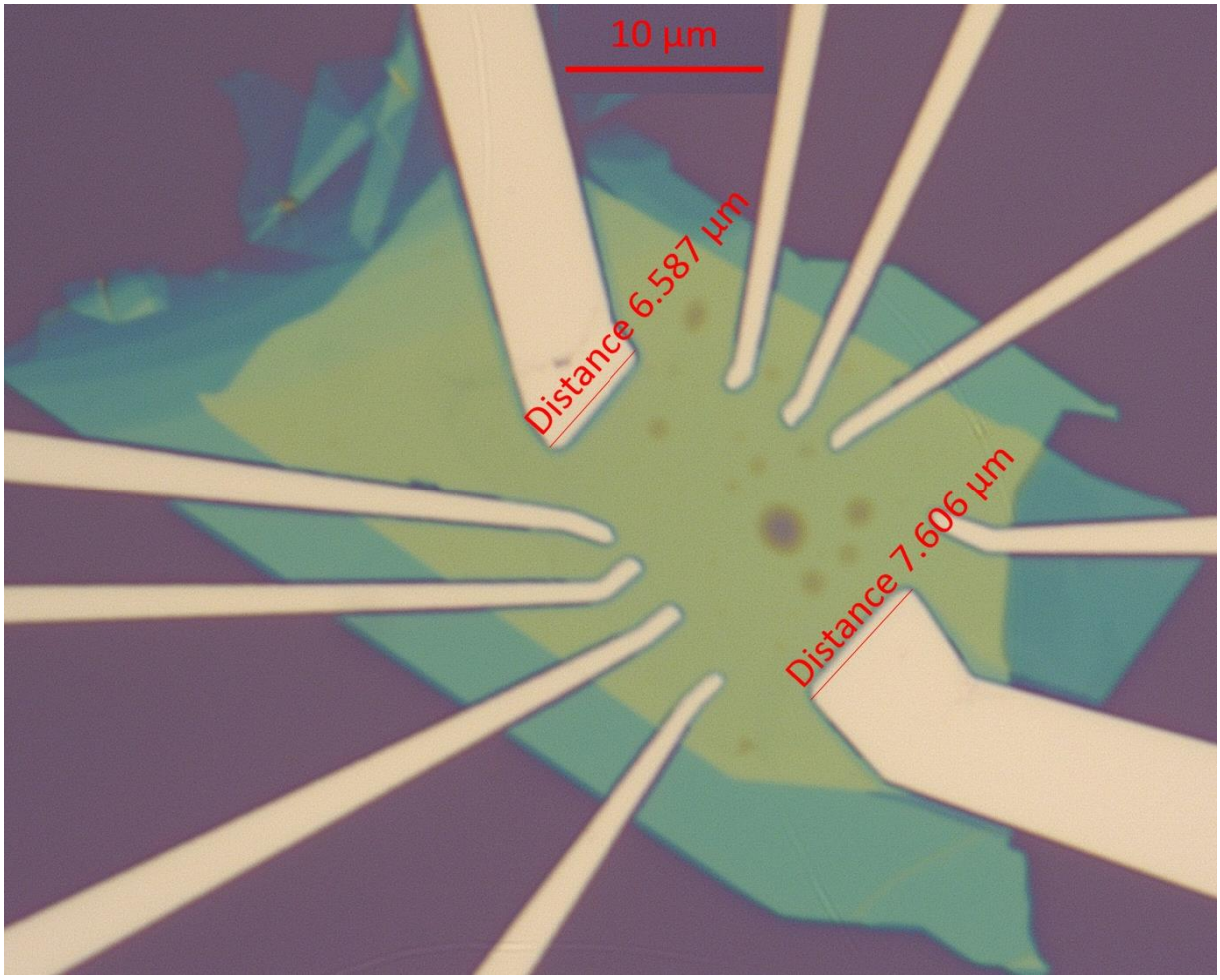
10 µm
Distance 6.587 µm
Distance 7.606 µm

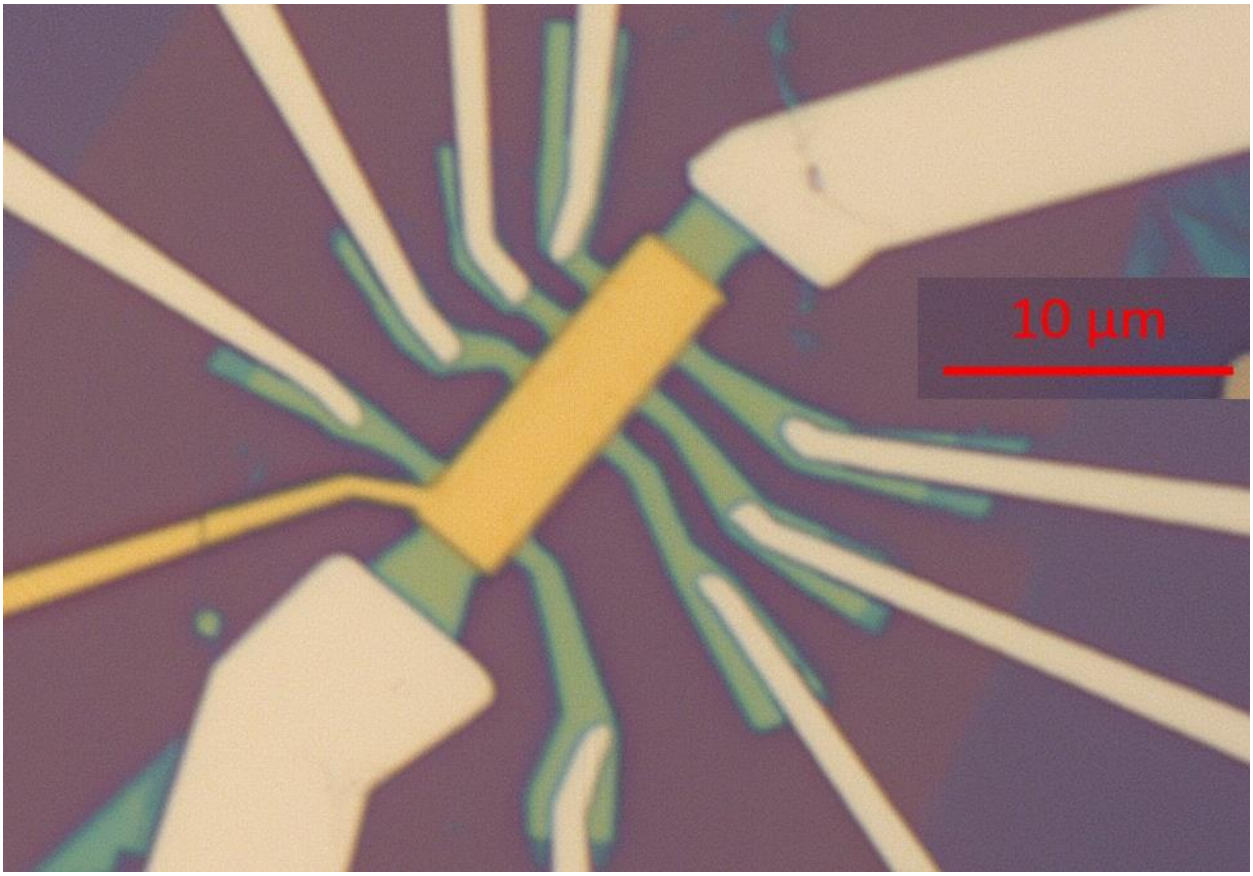

Figure C.6 Photos of wide gaps between metal contact and graphene. This is how we lose contacts.

To further understand this, we should take scanning electron microscope images of two undercuts in PMMA and KL IR for comparison.

One easy way to fix the gaps is making bandages on the contact areas to fill the gaps and repair electrical connections.

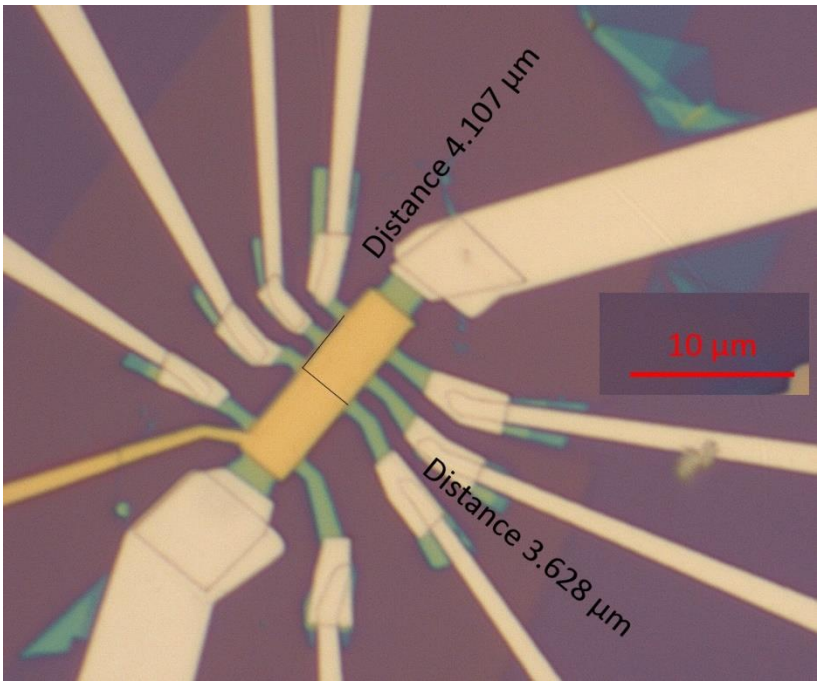

Figure C.7 Photo of metal bandages made to fill the gaps and repair the contacts.

Appendix D

Simulation by COMSOL Multiphysics

The simulation we use in our EMR project is based on the finite element method, which is a numerical method subdividing a large system into smaller and simpler parts called finite elements. These finite elements are modelled by the simple equations, which are then assembled into a larger system of equations to model the entire problem.

COMSOL Multiphysics is a finite element analysis, solver and simulation software for electrical, mechanical, fluid, and chemical applications. We use COMSOL Multiphysics 5.3a in our EMR project for simulation of the effect of p-n junction.

The process to set up the simulation is as follows:

(1) The Space dimension we select is 2D, the Physics module used is AC/DC -- Electric Currents, and the Study selected is Stationary.

(2) Define the geometric structure of the device. The radii of the metal disk and graphene can be set accordingly.

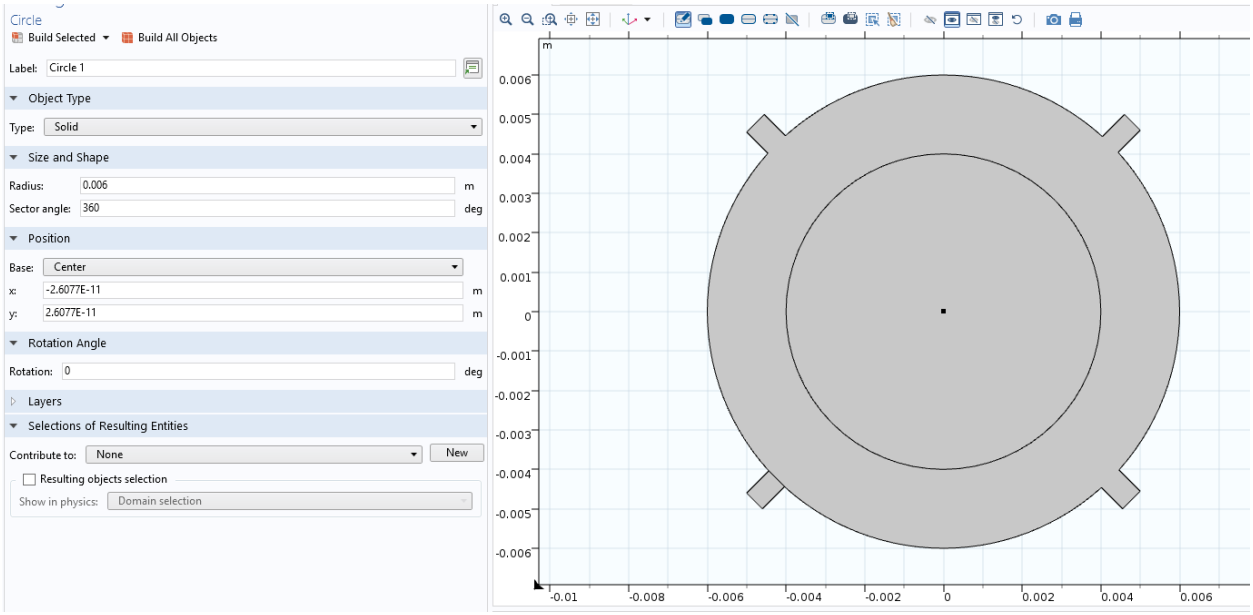

(3) The metal shunt is set to be Al. The thickness of deposited Al shunt in our experiment is 70 nm, but in COMSOL its thickness is set to be 0.335 nm the same as that of Graphene since their thickness cannot be set separately in the 2D setting (in COMSOL the same out-

of-plane thickness has to be set for all domains). To proportionally compensate the thickness change, I changed the conductivity of Al from 3.774e7 S/m to 788.597e7 S/m. The calculation is simple, the conductivity σ can be expressed as the resistivity ρ or as the resistance R, the length l, the width ω and the thickness t:

$$\sigma = \frac{1}{\rho} = \frac{l}{R\omega t}$$

$$\sigma \mathrm{t} = \frac{l}{R\omega}$$

Since we only change σ *and* t in the setting, R, l and ω should not change:

$$\sigma_{Al} \mathrm{t}_{Al} = \sigma \mathrm{t}_{G}$$

Since $\sigma_{Al} = 3.774e7 S/m, \mathrm{t}_{Al} = 70nm, \mathrm{t}_{G} = 0.335nm,$

We can get $\sigma = 788.597e7 S/m$. This is the adjusted conductivity of Al with the same thickness of graphene.

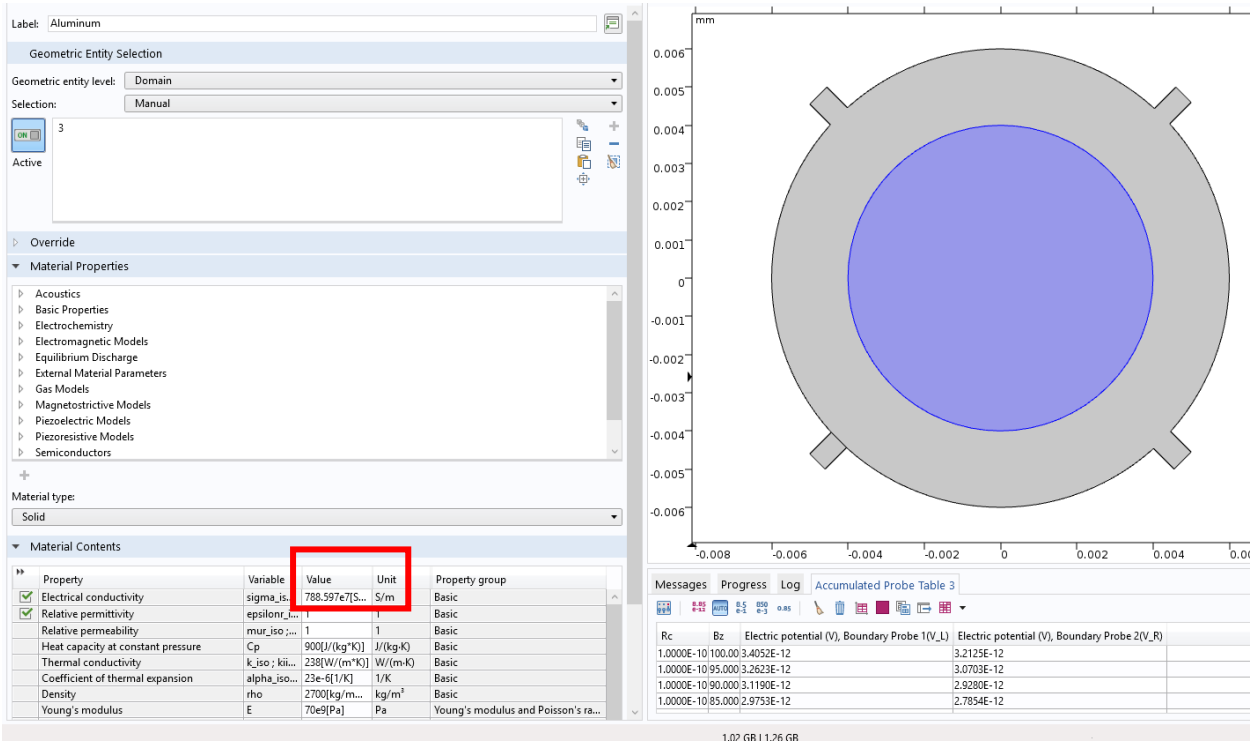

(4) The outer ring is graphene, the electrical conductivity of which is represented by our mathematical equations (4.3) to (4.6), which include the effect of doping and gate voltage.

$$\Rightarrow \sigma_g = \text{(1.602e-19*u*abs(7e14*Vg+7.347145e17*sign(1/(1+exp(2*log(3*(sys2.r-2.6e-6)/W)))*0.33)*(1/(1+exp(2*log(3*(sys2.r-2.6e-6)/W)))*0.33)^2)+sigma\_m)/0.335e-9}$$

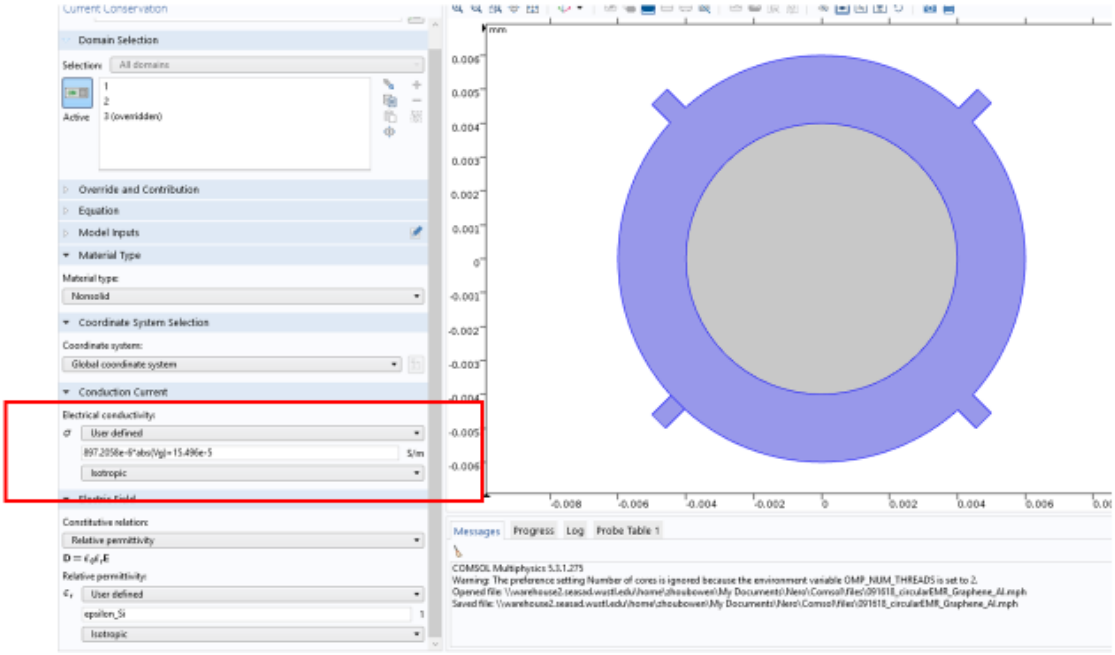

(5) The top two probes are voltage probes, and the bottom left probe is current source with I=100 nA. The bottom right probe is grounded.

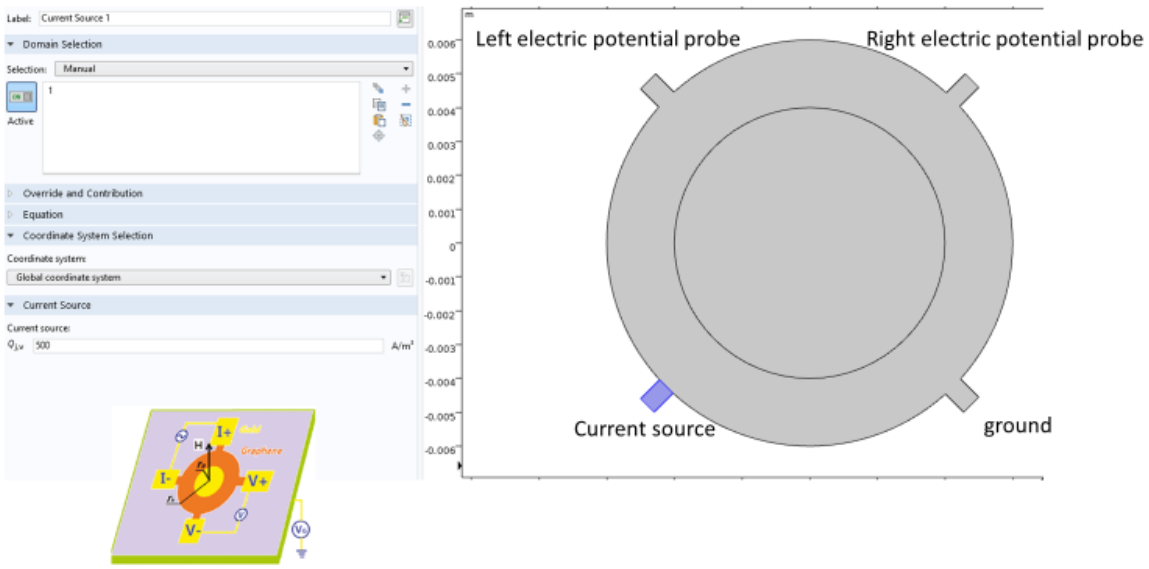

(6) The 2D setting only has x axis and y axis and doesn't not have z axis. So the 2D setting in COMSOL doesn't allow any physics vector in z direction, such as the electric field perpendicular to the plane. But there is a way to encounter this issue: in the setting of parametric sweep, we can set the range of the gate voltage we want to sweep with, and the gate voltage is already included in the equation. The right picture below shows the meshed device, which is ready for calculation.

$$\Rightarrow \sigma_g = (1.602e\text{-}19*u*abs(7e14*Vg+7.347145e17*sign(1/(1+exp(2*log(3*(sys2.r-2.6e-6)/W)))*0.33)*(1/(1+exp(2*log(3*(sys2.r-2.6e-6)/W)))*0.33)^2)+sigma\_m)/0.335e\text{-}9$$

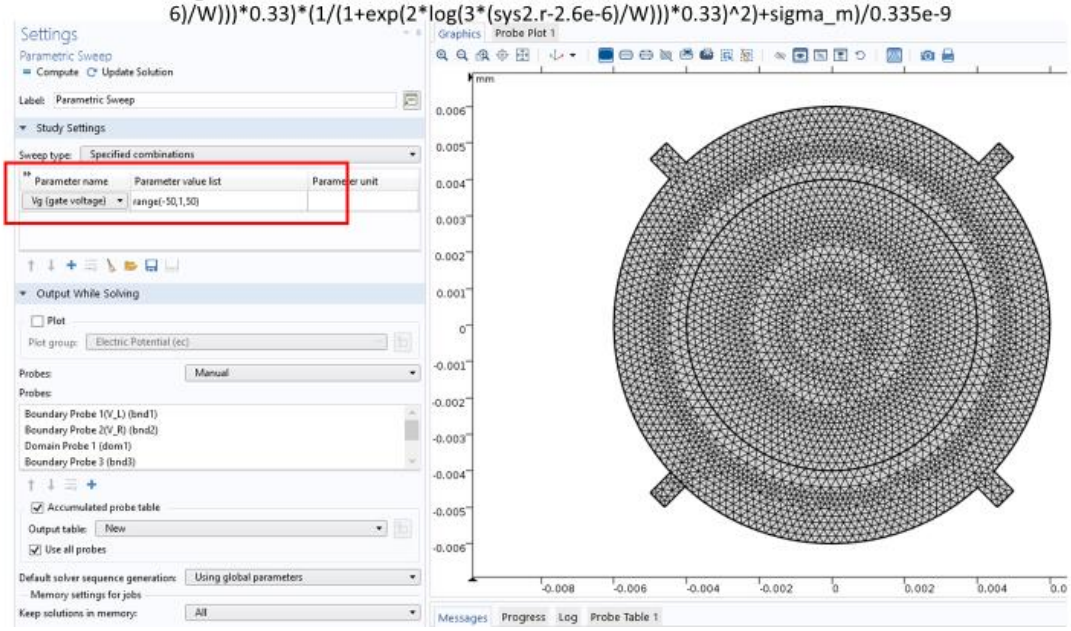

(7) Simulations of the current (arrows), electric potential (color) and equal potential lines (black contours) at zero magnetic field and zero gate voltage are shown below. Red: high electric potential, blue: low electric potential. The size of the arrows indicates the current density: the larger the arrows, the larger the current density in that area of device. The current prefers the path of the least resistance and runs through the metal disk at zero magnetic field.

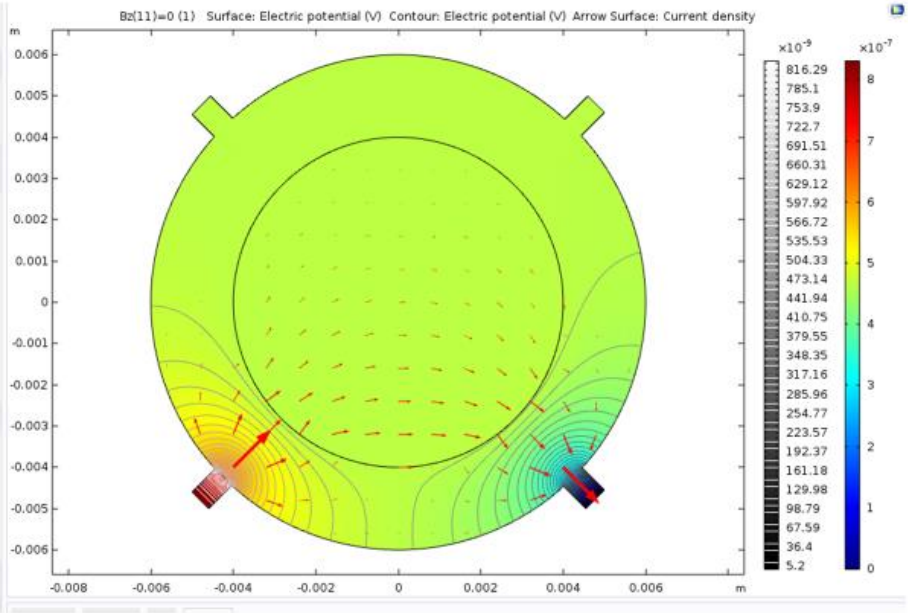

(8) The magnetic field can be set in the parametric sweep setting too. So the current in the device at zero field and high field are respectively shown below. The current gets deflected from the metal and run through the two sides of graphene at high field.

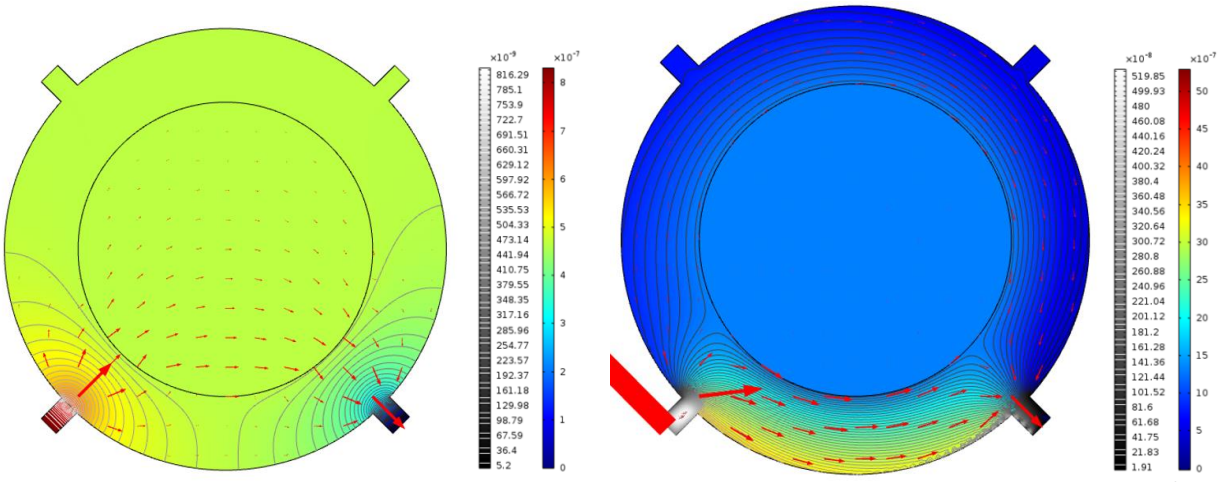

The simulation or calculation done by COMSOL provides the electric potentials at the two voltage probes along with the corresponding gate voltages. The data can be exported to Excel to calculate

the voltages and resistances (since the current is set to a fixed value), which are used to plot the voltage or resistance as a function of the gate voltage in Mathematica or Igor. The calculated resistance is eventually compared with the experimental measured resistance, shown in Chapter 4.